
Life cycle of contrails from a time series of geostationary satellite images

PhD Dissertation
Fakultät für Physik
Ludwig-Maximilians-Universität
Munich

Dipl.-Phys. Margarita R. Vázquez Navarro
from Madrid, Spain

Munich, September 2009

Gutachter der Dissertation:

1. Gutachter: Prof. Dr. U. Schumann
2. Gutachter: Prof. Dr. B. Mayer

Tag der mündlichen Prüfung: 09.11.2009

Summary

Contrails are ice clouds that have radiative effects similar to thin cirrus clouds. In satellite images, contrails are easy to identify thanks to their linear shape. If the atmosphere presents the necessary conditions for persistent contrail formation, contrails can evolve into contrail-cirrus, spreading and losing their characteristic linear shape. Thus, their identification from a satellite platform becomes more difficult. Identification of a contrail cirrus requires to follow the development of a contrail from its linear stage. This work describes the development of a contrail-tracking algorithm (ACTA). The algorithm follows the evolution of contrails from their linear stage until they are undistinguishable from natural cirrus clouds. Therefore, the study of the effect of aircraft-induced clouds in the atmosphere is not restricted to linear contrails and can include contrail-cirrus. The ACTA algorithm takes advantage of the high spatial resolution of polar orbiting satellites and the high temporal resolution of geostationary satellites. It allows for the first time to retrieve a very accurate dataset of contrails as they evolve into contrail-cirrus. The dataset generated is then combined with algorithms developed to study the irradiance using the narrowband radiometer on board a geostationary satellite. These algorithms have been validated in this work and show good agreement with the tools specifically developed to measure the Earth's radiation budget. These tools, however, do not offer the required spatial or temporal resolution for the study of aircraft induced cloudiness. The irradiance algorithms have then been used to develop a method of retrieving the radiative forcing of the contrails and contrail-cirrus tracked. In addition to the radiative forcing, measurements of optical thickness, geographical distribution and mean lifetime have also been retrieved. Results are in good agreement with previous works on linear contrails and with case studies on contrail-cirrus. They also highlight the need for considering the effect of surrounding cloudiness when assessing the impact of contrail-cirrus in the climate system.

Zusammenfassung

Kondensstreifen sind Eiswolken, die einen ähnlichen Effekt auf den Strahlungshaushalt der Erde haben wie dünne Zirren. Dank ihrer linearen Form sind Kondensstreifen auf Satellitenbildern einfach identifizierbar. Wenn in der Atmosphäre die nötigen Bedingungen für persistente Kondensstreifen vorherrschen, können sich die Kondensstreifen verbreitern und bei der Entwicklung in flugverkehrsinduzierte Zirren ihre ursprünglich lineare Form verlieren, was ihre Identifizierung in Satellitenbildern erschwert. Daher ist es nötig, ihren ganzen Lebenszyklus zu verfolgen, um auch bei alten, nicht linienförmigen Kondensstreifen den künstlichen Ursprung zu erkennen. In dieser Arbeit wurde ein Verfolgungsalgorithmus namens ACTA entwickelt, der Kondensstreifen von ihrem Sichtbarwerden in Satellitenbildern in Form von linienförmigen Kondensstreifen bis zur Zirrusphase verfolgt. Damit ist eine Analyse der Klimaeffekte von Kondensstreifen nicht mehr auf linienförmige Kondensstreifen begrenzt. ACTA nutzt sowohl die hohe räumliche Auflösung polarumlaufender Satelliten als auch die hohe zeitliche Auflösung geostationärer Satelliten. Er ermöglicht zum ersten Mal die Erstellung eines sehr genauen Datensatzes von Kondensstreifen während ihrer Entwicklung zu flugverkehrsinduzierten Zirren. Um den Strahlungsantrieb der verfolgten Kondensstreifen zu bestimmen, wurden zuerst Algorithmen, welche für die Ableitung von Strahlungsflussdichten aus Daten von Schmalbandradiometern an Bord eines geostationären Satelliten entwickelt wurden, auf den von ACTA erzeugten Datensatz angewandt. Diese Algorithmen wurden validiert und zeigen eine gute Übereinstimmung mit Methoden, welche üblicherweise für die Bestimmung des Strahlungshaushalts der Erde verwendet werden, im Rahmen dieser Arbeit jedoch nicht anwendbar waren, da sie nicht über die nötige räumliche oder zeitliche Auflösung verfügen. Basierend auf den Algorithmen wurde eine Methode entwickelt, um den Strahlungsantrieb der verfolgten Kondensstreifen abzuleiten. Außerdem wurden die optische Dicke, die geographische Verteilung und die Lebensdauer der Kondensstreifen bestimmt. Die Ergebnisse sind in guter Übereinstimmung sowohl mit früheren Arbeiten über lineare Kondensstreifen als auch mit Fallstudien von flugverkehrsinduzierten Zirren und zeigen deutlich die Notwendigkeit, benachbarte Bewölkung zu berücksichtigen, wenn man den Einfluss flugverkehrsinduzierter Bewölkung auf das Klima quantifizieren will.

Contents

1	Preface	1
2	Introduction	7
2.1	Fundamentals of Atmospheric Radiation	7
2.2	Remote Sensing	14
2.2.1	MSG - Meteosat Second Generation	14
2.2.2	Terra	21
3	Methods	27
3.1	Automatic Contrail Tracking Algorithm: ACTA	27
3.1.1	ACTA: input. Contrail Detection Algorithm	28
3.1.2	ACTA: description	29
3.1.3	Discussion	48
3.2	Outgoing longwave radiation	51
3.3	Reflected shortwave radiation	54
3.4	Validation	56
3.4.1	Mapping - Modified Nearest Neighbour Method	56
3.4.2	Validation of the MSG/SEVIRI irradiance algorithms	62
3.4.3	Discussion	70
3.5	Radiative forcing	71
3.6	Optical thickness	72

4	Life cycle of contrails: results	75
4.1	Case Studies	75
4.1.1	Case 1	76
4.1.2	Case 2	78
4.1.3	Case 3	79
4.1.4	Conclusions	81
4.2	Systematic Studies	83
4.2.1	Geographical distribution	83
4.2.2	Lifespan	86
4.2.3	Optical thickness	87
4.2.4	Radiative Forcing	88
5	Conclusions and outlook	93
A	Contrail tracking. Example	99
B	Validacion of irradiances: CERES/Terra vs. SEVIRI/MSG	109
C	Analysis of discrepancies	115
D	Validation of irradiances: GERB/MSG vs. SEVIRI/MSG	123
	Acronyms and abbreviations	129
	Bibliography	131

Chapter 1

Preface

Aviation industry is a mere 100 years old but constitutes an essential part of modern society. It has undergone a very rapid expansion that is likely to continue: passenger traffic has grown at rates in excess of the average gross domestic product since 1960 (Penner et al., 1999). The emission by an aircraft engine of a certain amount of gases and particles in the upper troposphere can initiate the formation of condensation trails (contrails) and cirrus clouds. A contrail-cirrus cloud is a naturally looking cirrus cloud that would not exist without prior formation of a contrail. This type of cirrus formation occurs mainly in regions with high levels of air traffic (Gierens, 2006).

Contrails are ice clouds and their radiative effects are similar to that of thin cirrus clouds (Fu and Liou, 1993). The presence of aircraft induced cloudiness, contrail-cirrus, can modify the radiative properties of the atmosphere and therefore influence the climate system. The aim of this work is to separate between natural and anthropogenic clouds by studying the life cycle of contrails. The influence of contrail-cirrus on the global radiative forcing has been pointed out in a large number of papers (e.g. Sassen (1997), Minnis et al. (2004)) but the radiative properties of contrail-cirrus are still uncertain (Schumann, 2005) despite the numerical simulation studies on the origin and growth of the initial stages of contrails (Gierens, 1996) and the case studies on the evolution of their microphysical properties until their transition to cirrus is completed (Schroeder et al., 2000). The extent of the effect of the aircraft induced cirrus on the climate system remains still unclear. The IPCC report (2007) established the Level Of Scientific Understanding of the role of linear contrails in the climate system as *fair*, but this was recently reduced to *low* by Lee et al. (2009). The uncertainty on contrail-cirrus is even larger, the Level Of Scientific Understanding on induced cirrus cloudiness is *very low* according to Lee et al. (2009). An evaluation of the effects of contrail cirrus over the globe is complex because of the great geographic and diurnal variability of air traffic, the variability of optical thickness and persistence of the clouds, the influence of high surface albedo and neighbouring clouds, and the natural changes in ambient humidity.

According to the Schmidt-Appleman criterion, contrails form as a result of mixing of heat and water vapour between the warm and moist exhaust of the jet and the cool ambient air. This criterion is not sufficient for contrail formation and the efficiency of the engine must also be taken into account (Schumann, 1996). The validity of this theory has been demonstrated and confirmed on various research flights (IPCC, Penner et al. (1999)). The formation

of persistent contrails is only possible if the ambient air is supersaturated with respect to ice. These persistent anthropogenic cirrus clouds can increase in coverage by more than four times due to spreading (Minnis et al., 1998) and become undistinguishable from their natural counterparts. The difficulty in identifying the naturally looking but nevertheless aircraft-induced part of total high cloudiness from satellite images has been stated (Mannstein and Schumann, 2005) and overcoming this difficulty is the aim of this work.

The radiative forcing of a contrail-cirrus depends not only on the additional coverage, but also on its geographic location, altitude, time of day, season, and the background state of the atmosphere (e.g. whether there are lower clouds or not). High-altitude thin contrail-cirrus tend to warm the Earth-Atmosphere system during day and night time if located above a bright and warm surface, whereas low-altitude thick contrail-cirrus tend to cool the Earth-Atmosphere system during day time especially if located above dark and cold surfaces (Meerkoetter et al., 1999). It should be noted that the net radiative forcing is the difference between two large values: the large (mostly negative) radiative forcing in the shortwave range and the large (positive) radiative forcing in the longwave range.

Sausen et al. (2005) provided an estimate of global radiative forcing of aviation for the year 2000 of 47.8 mW/m^2 considering aircraft exhaust emissions and contrails, but not contrail-cirrus. This result is similar to that given by Penner et al. (1999) for the year 1992 (48.5 mW/m^2). Estimates of the global radiative forcing of line-shaped contrails vary from 17.5 mW/m^2 (Minnis et al., 1999) down to 2 mW/m^2 (Stuber and Forster, 2007). The radiative forcing of contrail-cirrus is still to be accurately assessed. Sausen et al. (2005) proposed a 30 mW/m^2 radiative forcing of contrail-cirrus with an uncertainty range of 10 to 80 mW/m^2 , assuming similar optical properties to very thin cirrus. This value was adopted by the IPCC's Fourth Assessment Report (Solomon et al., 2007) with the caveat that it does not constitute a best estimate. These values are in good agreement with the upper limit value of aviation-cirrus forcing of 26 mW/m^2 estimated by Minnis et al. (2004). It is important to perform more accurate computations because although the global mean of these forcings is low, the regional impact could be higher, up to 0.5 W/m^2 over Europe and North America (Minnis et al., 1999). The strong growth rate of aviation demands to reduce the uncertainties of linear persistent contrails and aircraft induced cloudiness (Lee et al., 2009).

Schumann (2005) stated that significant uncertainties still remain over contrail optical thickness. Radiative forcing and optical thickness are non-linearly related, and it is possible that contrails within cirrus enhance the optical thickness of the existing cirrus to values for which the radiative forcing becomes negative (Schumann, 2005); hence, a reliable estimate of the radiative forcing by contrails or by contrail-cirrus cannot be given without knowing their optical thickness. Contrail optical thickness presents a wide range of values over various seasons, geographical regions and altitudes (Palikonda et al., 2005). Lidar measurements have found optical thicknesses ranging from 0.05 to 0.5 (e.g. Minnis et al. (1998)). Meyer et al. (2002) retrieved an effective optical thickness of 0.1 over Europe from satellite data. Larger values (0.2 to 0.26) were found over the USA (Minnis et al., 2004) presumably due to the higher temperatures of the North American atmosphere (Schumann, 2005). Ponater et al. (2002) established that the typical optical thickness of contrails is lower than 0.3. These values cannot be applied to contrail-cirrus because the optical thickness varies with the aging of the contrail. There have been only a few case studies on the evolution of the optical thickness

in the transition from contrail to contrail-cirrus: Duda et al. (1998) estimated cloud particle size and infrared optical thickness of contrail-cirrus during the SUCCESS experiment: the particles in a newly formed contrail were generally smaller than those in an older contrail and the microphysics of the older contrail resembled the surrounding cirrus clouds. The retrieved mean optical thickness during the experiment was 0.35 (reaching values over 1.5) and they also assessed that the older contrail was optically thicker. In a case study combining satellite information and ground-based lidar measurements, Atlas et al. (2006) retrieved a lifetime of more than 2 hours and a mean optical thickness of 0.35. Duda et al. (2004) studied the development of contrail clusters over the Great Lakes and derived optical thicknesses from 0.1 to 0.6 that lasted several hours. Kaercher et al. (2009) mentions the difficulty of tracking contrails once they have lost their linear shape by satellite detection algorithms, which is a reason for the lack of robust data on their microphysical properties and the apparent absence of measurements of older contrail-cirrus. Kaercher et al. (2009) also introduced an analytical model to estimate contrail-cirrus evolution and compare the results with in situ and remote sensing measurements. They estimated that mean contrail cirrus visible optical thicknesses range between 0.05 and 0.5 and also pointed out that a substantial fraction of contrail-cirrus is subvisible and has a non-negligible effect on the radiative forcing.

Mannstein et al. (1999) developed a contrail detection algorithm, a fully automated method for line-shaped contrail detection that will be used in this work. This method has been applied to several regions of the Earth: Central Europe (Meyer et al., 2002), North America (Palikonda et al., 2005), Eastern North Pacific (Minnis et al., 2005) and Southern and Eastern Asia (Meyer et al., 2007).

The knowledge of the percentage of the sky covered by contrails and contrail-cirrus is required to calculate a mean global radiative forcing. The contrail cover is very variable and dependent on the air traffic diurnal cycle (Stuber and Forster, 2007). Bakan et al. (1994) derived a 0.88% annual contrail coverage in the region 40-55 °N and 10°W - 20°E at daytime and 0.44% at night time. Meyer et al. (2002) established 0.74% at day and 0.25% at night over central Europe and found a seasonal dependency. Sausen et al. (1998) performed the first analysis for the global contrail cover. They combined temperature and humidity data from numerical weather analysis and aircraft fuel inventories to estimate the amount of air traffic in a global model grid box, and derived a global line-shaped contrail cover of 0.09%. This result was calibrated with the Bakan et al. (1994) estimates. Gierens et al. (1999) computed a future contrail cover of 0.25% for 2015 and between 0.26% and 0.75% for year 2050 considering a static climate. However, the consideration of a warmer future climate due to the increase in greenhouse gas concentrations leads to a lower future contrail cover: 0.14% in 2015 and 0.22% in 2050 (Marquart et al., 2003). Stuber and Forster (2007) established a 0.04% global mean contrail cover using AERO2k¹ flight data calibrating the result with the estimates of Bakan et al. (1994).

¹AERO2k is a global inventory of aircraft fuel consumption and emissions for 2002 and an emissions forecast for 2025 for climate impacts evaluation

None of these calculations include the contrail-to-cirrus transition. Contrails trigger contrail-cirrus with far larger coverage than observed line-shaped contrails (Zerefos et al., 2003; Minnis et al., 2004) but the difficulty in distinguishing the naturally looking but nevertheless aircraft-induced part from the total high cloudiness in satellite images (Schumann, 2005; Mannstein et al., 1999) has prevented the calculation of a reliable aircraft induced cloudiness cover and thus of a radiative forcing best estimate for aircraft induced cloudiness as a whole (Sausen et al., 2005).

This work focuses on contrails and aviation induced cloudiness from a space-borne point of view. The advantage of this approach is that it covers very large regions of the Earth and thus provides a wider range of events than single measurements. Two data sources will be used in this study: data from geostationary satellites and data from polar orbiting satellites. Geostationary satellites provide information on the time evolution of contrails. From a geostationary satellite, the whole extent of a contrail can be seen at once and its ageing can be followed, even very short lived cases. However, the distance to the Earth limits the spatial resolution of the instruments and, therefore, prevents the detection of fresh and thin contrails. These may be detected by a polar orbiting satellite, which orbits closer to the surface. Therefore, the best approach to study the evolution of these anthropogenic clouds is a combination of both platforms: young contrails can be detected and their evolution can be witnessed, even in the late stages, when they lose linearity and become undistinguishable from natural cirrus clouds. The fundamentals of atmospheric radiation and the instruments and sensors used in this work are described in Chapter 2.

The work described in this thesis is the development of a contrail-tracking algorithm (Chapter 3, Section 3.1) and its application to the retrieval of physical properties of contrails (Chapter 4). The algorithm combines data from two radiometers (MODIS, on a polar orbiting satellite, and SEVIRI, on a geostationary satellite), exploiting the advantages of each. First, MODIS data are used as input. The very high spatial resolution of the MODIS sensor grants an accurate contrail detection. Second, MODIS data are combined with SEVIRI data to take advantage of SEVIRI's high temporal resolution. In particular, the Rapid Scan mode of SEVIRI has a 5 minute temporal resolution, which enables a very accurate tracking and study of the evolution of the cloud in nearly all stages of its development: from the moment it is first seen from the geostationary satellite until it can no longer be distinguished from the background.

The radiative forcing of the tracked contrails is calculated by measuring the outgoing top of atmosphere irradiance and comparing it to the irradiance in the contrail-free case. This requires an assumption on the state of the atmosphere in the contrail-free case. The usual instruments to retrieve radiative forcing are designed for climate studies, they focus on synoptic scale structures and work on a low spatial resolution basis. Since these instruments do not require to resolve very small structures, their spatial resolution is inadequate for the study of contrails. The computation of the radiative forcing of contrails will be performed thanks to two algorithms also based on MSG/SEVIRI data and described in Chapter 3, Sections 3.2 and 3.3. The new algorithms take advantage of the full MSG/SEVIRI resolution (3 km at nadir) and have been validated in this work with instruments widely used and accepted by the scientific community such as CERES (on polar orbiting platforms such as Terra, Aqua and TRMM) and GERB (on board of MSG).

Following the theory (Chapter 2) and the description of the methods (Chapter 3), Chapter 4 concentrates on the combination of the tracking algorithm and the irradiance retrieval tools in order to assess the radiative forcing of the contrails. Case studies have been performed to provide a better insight into the results prior to running the algorithm on a dataset that is representative for the whole year. Other properties of the contrail-cirrus such as the optical thickness, coverage, spatial distribution and lifetime have also been assessed with specifically developed algorithms.

Chapter 5 summarises the results and discusses the possible future steps to be taken.

Chapter 2

Introduction

The first part of this chapter (Section 2.1) presents an overview of the fundamentals of atmospheric radiation and radiative transfer in both the shortwave and the longwave regions. Section 2.2 describes the performance and characteristics of the main satellites and sensors used in this work. These satellites are Meteosat Second Generation (MSG) and Terra, a NASA's Earth Observing System. The instruments on board that have been used in the different stages of this research, MSG's SEVIRI and GERB, and Terra's CERES and MODIS, are also described in this section.

2.1 Fundamentals of Atmospheric Radiation

Any exchange of energy between the Earth and the rest of the universe is carried out throughout the radiative transfer. The Sun is the only external source of energy for the Earth, as the rest of heavenly bodies provide a negligible amount of energy. The Earth and its atmosphere absorb and scatter solar radiation and emit their own thermal radiation back into the space. Averaging over a long enough period of time, absorption and emission are balanced, i.e., the Earth-atmosphere-Sun system is in radiative balance. Radiative transfer is a way of exchanging energy between the atmosphere and the Earth surface as well as among the different atmospheric layers. Transmission, reflexion and scattering of radiation by the atmosphere determine the visibility, the colour of the sky, etc.

Any isolated molecule has a given amount of energy, besides the one associated to its motion through space. Most of this is in the form of kinetic and potential energy of the electrons moving in the different orbits around the nuclei of atoms. Additional energy amounts are related to the vibration of individual atoms about their mean positions in the molecule and to the rotation of the molecule around its centre of mass. Quantum mechanics predicts that only certain electron configurations are allowed for each atom and only certain frequencies and amplitudes of vibration and rotation are allowed for each molecule. Only discrete changes among energy levels are permitted, characterising the transition, the molecule involved, and building its absorption (or emission) spectrum. This results in a finite number of narrow absorption (or emission) lines. In the gaps between lines the absorption or emission of radiation is not possible.

The energy transmitted by electromagnetic radiation is carried out through discrete units, the photons. The energy W associated to each photon is $W = h\nu$, where ν is the frequency of the radiation and h is the Planck constant. The radiation travels at the speed of light, c , so frequency and wavelength are related through $\nu = c/\lambda$.

The rate of exchange of energy, *radiant flux*, Φ , has units of energy/time (J/s, W). The *flux density* or *irradiance* (hereafter: irradiance) accounts for the radiant flux through a surface A (Eq. 2.1):

$$F = \frac{d\Phi}{dA} \quad (2.1)$$

Equation 2.1 can describe the irradiance reaching a surface:

$$F^\downarrow = \frac{d\Phi}{dA} \quad (2.2)$$

and that leaving a surface:

$$F^\uparrow = \frac{d\Phi}{dA} \quad (2.3)$$

Being the net irradiance

$$F_{net} = F^\downarrow - F^\uparrow \quad (2.4)$$

The emission of radiation is angle-dependent, so a new magnitude can be defined: *radiance* or *intensity*, L . L accounts for the flux density crossing an element of area dA in directions confined to a differential solid angle $d\Omega$, which is oriented at an angle θ to the normal of dA . Units: W/(m² sr)

$$L = \frac{d^2\Phi}{\cos\theta dA d\Omega} \quad (2.5)$$

Combining Equations 2.1 and 2.5, the incoming irradiance is related to the radiance via:

$$F = \int_0^{2\pi} L \cos\theta d\Omega = \int_0^{2\pi} \int_0^{\pi/2} L \cos\theta \sin\theta d\theta d\phi \quad (2.6)$$

For isotropic radiation reaching a surface, i.e. if the radiance is independent of direction, integrating Eq. 2.6 over the upper hemisphere gives:

$$F^\downarrow = \pi L \quad (2.7)$$

A blackbody is an hypothetical body that absorbs all incoming radiation and emits it back into space in all wavelengths and in all directions. The amount of energy and its spectral distribution in the spectrum are described by Planck's (Eq. 2.8), Stefan-Boltzmann (Eq. 2.13) and Wien's (Eq. 2.14) laws.

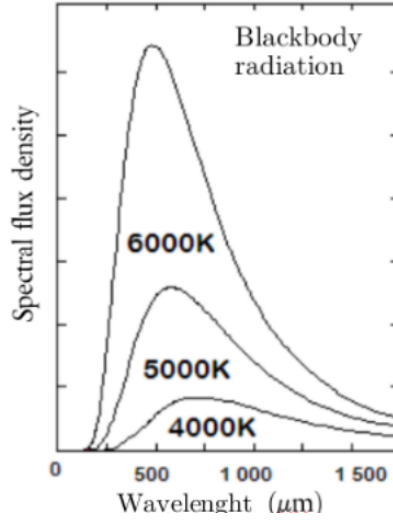


Figure 2.1: Blackbody radiation per wavelength for a number of emitting temperatures.

Planck's Law

The amount of radiation emitted by a blackbody is completely defined by its temperature, and has a given spectral distribution according to *Planck's law* (Planck, 1901). Planck derived the spectral radiance theoretically and defined the so-called Planck function:

$$B_{\lambda}(T) = \frac{2hc^2}{\lambda^5 [e^{\frac{hc}{\lambda T}} - 1]} \quad (2.8)$$

where c is the speed of light, h is the Planck constant and k is the Boltzmann constant.

Equation 2.8 relates the spectral radiance to the temperature T of the emitting body. In Fig. 2.1 the radiance is plotted versus wavelength for a number of temperatures. It is evident that the blackbody radiance increases with temperature and the wavelength of the maximum radiance decreases with increasing temperature.

Inverting the Planck function to find the temperature T_b at which a blackbody would have to be in order to produce the measured radiance, L_m , at a wavelength λ gives the *brightness temperature*.

$$T_b = \frac{c_2}{\lambda \ln(c_1/L_m \lambda^5 + 1)} \quad (2.9)$$

where $c_1 = 2hc$ and $c_2 = hc/k$.

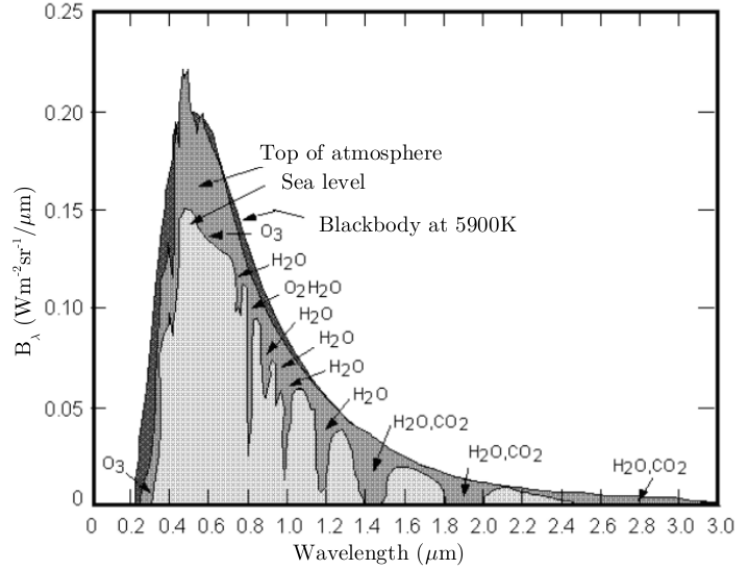


Figure 2.2: Solar spectrum at TOA and at sea level and comparison to blackbody spectrum at 5900K. Source: Wallace and Hobbs (1977).

Stefan-Boltzmann Law

The blackbody irradiance can be derived by integrating the Planck function (Eq. 2.8) over all wavelengths. Hence,

$$B(T) = \int_0^{\infty} B_{\lambda}(T) d\lambda = \int_0^{\infty} \frac{2hc^2 \lambda^{-5} d\lambda}{[e^{\frac{hc}{k\lambda T}} - 1]} \quad (2.10)$$

Introducing a new variable $x = hc/k\lambda T$, Eq. 2.10 becomes:

$$B(T) = \frac{2k^4 T^4}{h^3 c^2} \int_0^{\infty} \frac{x^3 dx}{(e^x - 1)} \quad (2.11)$$

The integral term in Eq. 2.11 is equal to $\pi/15$. Thus, defining $b = 2\pi^4 k^4 / (15c^2 h^3)$, we have:

$$B(T) = bT^4 \quad (2.12)$$

Since blackbody radiation is isotropic, the irradiance emitted by a blackbody is (see Eq. 2.7) $F = \pi B(T)$. Therefore

$$F = \sigma T^4 \quad (2.13)$$

where σ is Stefan-Boltzmann's constant ($5.6710^{-8} \text{ W m}^{-2} \text{ K}^{-4}$) and T is temperature. For bodies that are not blackbodies and thus do not emit following this law, it must be modified adding an spectral emissivity coefficient: $F = \epsilon \sigma T^4$.

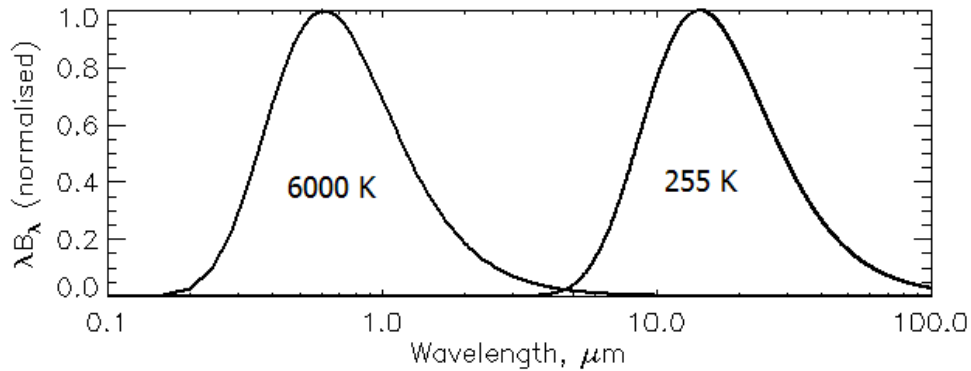


Figure 2.3: Solar and terrestrial normalised spectra.

The spectral emission of the Sun is very similar to that of a blackbody at a temperature of 5900 K. At the Earth's surface, the spectrum is modified by the influence of the atmospheric constituents (see Fig. 2.2).

Stefan-Boltzmann's law (Stefan, 1879; Boltzmann, 1884) is fundamental in the field of infrared radiative transfer. It allows to translate the radiances measured by the radiometers on board of satellites into brightness temperatures.

Wien's Displacement Law

By differentiating the Planck function (Eq. 2.8) with respect to wavelength and by setting the result equal to zero we obtain the wavelength of peak emission for a blackbody at temperature T :

$$\lambda_m T = \text{const} = 2897 \text{ } [\mu\text{m K}] \quad (2.14)$$

Through Eq. 2.14, which is known as *Wien displacement law* (Wien, 1896), it is possible to determine the temperature of a radiation source from its emission spectrum.

An important follow-up of Planck and Wien's law is the practical absence of overlap between the curves depicting solar and terrestrial normalised spectra (Fig. 2.3). While solar emission is produced mainly in the visible and near-infrared parts of the spectrum, terrestrial emission of radiation is practically confined to the infrared wavelengths. This allows for most applications the separate study of solar and terrestrial components of radiation.

The equation of transfer

Radiation traversing a medium will be weakened by its interaction with matter. The change in the radiance undergone by radiation passing through a layer of infinitesimal thickness dz

is proportional to the number of molecules per unit area that are absorbing radiation along the path. This relationship can be described by:

$$dL = -\sigma_{ext}n_0Ldz \quad (2.15)$$

where σ_{ext} denotes the extinction cross section and n_0 is the particle density. Integration of Equation 2.15 leads to the *Beer-Bouger-Lambert law*:

$$L = L_0e^{-\int \beta_{ext}dz} \quad (2.16)$$

where $\beta_{ext} = \sigma_{ext}n_0$ is the extinction coefficient, the sum of scattering and absorption coefficients, $\beta_{ext} = \beta_{scat} + \beta_{abs}$. Absorbed radiation is converted to internal energy of the absorbing molecules. Scattered radiation contributes to the radiance in other directions.

The weakening of the radiation following a path from S_1 to S_2 can be described by the *optical thickness*, τ :

$$\tau = \int_{S_1}^{S_2} \beta_{ext} dz \quad (2.17)$$

In addition to the weakening of radiation according to Equation 2.15, the radiance may be strengthened by emission of the material plus multiple scattering from all other directions into the pencil of radiation under consideration. The monochromatic radiation intensity at frequency ν emitted along a vertical path at the top of the atmosphere and incident at a satellite-borne instrument is given by:

$$L_\nu = (L_0)_\nu T_\nu(z_0) + \int_{z_0}^{\infty} B_\nu[T(z)] \frac{dT_\nu(z)}{dz} dz \quad (2.18)$$

where: L_0 is the emission from the Earth's surface at height z_0 ,
 $T_\nu(z)$ is the vertical transmittance from height z to space,
 $T(z)$ is the vertical temperature profile and
 $B_\nu[T(z)]$ is the corresponding Planck function profile.

Equation 2.18 can also be written as

$$L_\nu = (L_0)_\nu T_\nu(z_0) + \int_{z_0}^{\infty} B_\nu[T(z)] W_\nu(z) dz \quad (2.19)$$

where $W_\nu(z) = dT_\nu(z)/dz$ is the weighting function.

A *weighting function* is the change of the total transmittance with respect to pressure. It specifies the layer of the atmosphere from which the radiation measured by the satellite channel was emitted and, hence it determines the region of the atmosphere which can be sensed from space at this frequency. Since it is the derivative of the transmittance, the weighting function peaks higher in the atmosphere for the frequency at which the absorption is stronger.

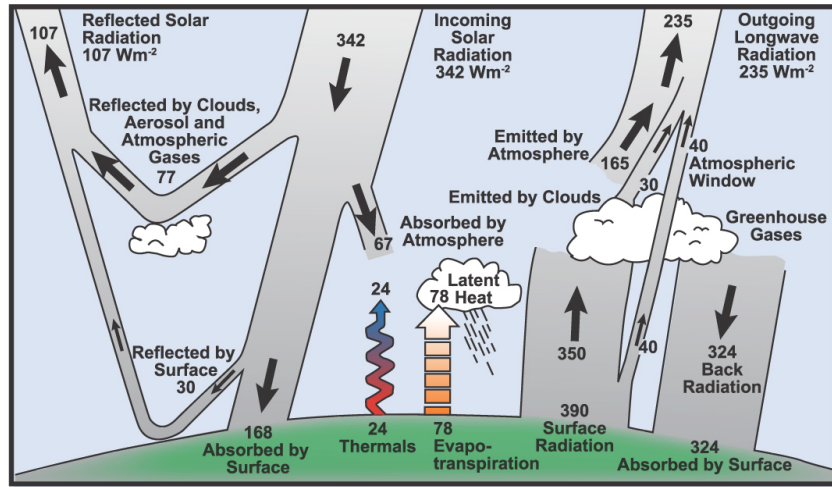


Figure 2.4: Estimate of the Earth's annual and global mean energy balance. Source: Kiehl and Trenberth (1997).

Earth Radiation Budget

The Earth receives energy from the Sun and re-emits it back to space as reflected solar radiation and outgoing thermal radiation. The Earth Radiation Budget is the balance between incoming energy from the Sun and the outgoing longwave (thermal) and reflected shortwave energy from the Earth. This energy balance can be influenced by modifying the amount of greenhouse gases, aerosols and clouds. Greenhouse gases in the atmosphere absorb energy emitted by the Earth and prevent its emission into space leading to a warming of its surface. Aerosols produced by both natural processes or human activities can reflect part of the sunlight back into space. Clouds exert both a cooling effect on the surface by reflecting sunlight back into space, and a warming effect by trapping heat emitted from the surface and emitting it at lower temperatures (see Fig. 2.4). One of the most difficult problems in the study of clouds is their high variability: horizontally, vertically and in time.

The IPCC defines the *radiative forcing* of the surface-troposphere system as the change in net irradiance at the tropopause (solar plus longwave, see Equation 2.20) due to the introduction of or the perturbation in an agent.

$$\Delta F_{net} = \Delta F_{SW} + \Delta F_{LW} \quad (2.20)$$

When a cloud is present, the forcing is defined as the difference between clear-sky and cloudy-sky irradiances at top of atmosphere (TOA) in both the shortwave and the longwave ranges (see Eq. 2.21). Cloud radiative forcing is one of the largest sources of uncertainties in the Earth's radiation budget (Penner et al., 1999).

$$\Delta F_{net} = F_{clear-sky} - F_{cloudy} \quad (2.21)$$

Contrails have a lower temperature than the atmosphere below the contrails and hence induce a positive radiative forcing in the LW range, causing a warming. In most cases, contrails increase the Earth's albedo and cause a negative radiative forcing in the SW range, causing a cooling. At nighttime, when the SW forcing is zero, the only contribution to the net radiative forcing is that of the LW, which is positive. At daytime, both SW and LW play a role. The radiative forcing grows with the optical thickness and with the amount of contrail cover. The influence of surrounding clouds and the reflectance of the background may alter this behaviour essentially by diminishing the SW forcing and probably by slightly increasing the LW forcing of low optical thickness contrail cirrus. The SW effect is also dependent on the solar zenith angle (Meerkoetter et al., 1999).

The current issue of whether the presence of air traffic leads to an increase of cirrus clouds has very likely an affirmative answer (Penner et al., 1999; Solomon et al., 2007). Air traffic takes place around the tropopause, where the temperature is very low and the greenhouse effect strong, contributing with exhaust emissions to the development of contrails. Given the constant raise of air traffic, it is of great concern that the increase of contrails can affect the Earth's radiative balance.

2.2 Remote Sensing

Infrared radiation emitted by the Earth-atmosphere system and reflected visible radiances measured by the satellites are the basis of remote sensing. In order to provide an exhaustive study of the development of aviation induced cloudiness, to quantify their radiative forcing and to assess their influence in the climate system, the use of meteorological satellites is required.

2.2.1 MSG - Meteosat Second Generation

To study the impact of air traffic on climate, remote sensing observations along the major air traffic routes were required. Air traffic presents a strong diurnal cycle so a high temporal resolution sensor with several observations per day is necessary. Moreover, air traffic has a different effect on the cloud cover and on the radiative balance depending on the season and the atmospheric conditions; so data of different months are required. Besides, day and nighttime data are required due to the fact that a large amount of long distance flights



Figure 2.5: MSG. Source: EUMETSAT.

take place overnight, so the use of infrared sensors is necessary. A system that fulfils all these requirements is the second generation of Meteosat, the European geostationary satellite program. MSG's sensors provide information with a very high spatial and temporal sampling about heavily flown areas such as Europe and the North Atlantic.

The second generation of Meteosat consists of a series of four spin stabilised spacecrafts that will operate consecutively. To guarantee continuity of service, one MSG will remain in geostationary orbit above Europe and Africa, with a second MSG on standby in a parking orbit nearby. Each MSG has a design life of seven years, so that the four spacecrafts should support operational meteorologists until 2018 or later. MSG-1 and MSG-2 are already in orbit (launched in 2002 and 2005) and the remaining MSG-3 and MSG-4 are yet to be launched (tentatively planned for 2010 and 2013). The MSG satellites are 3.2 m in diameter and 2.4 m high and spin anti-clockwise at 100 rpm at an altitude of 36,000 km above the Equator.

The main instrument on board of MSG is its radiometer SEVIRI (Spinning Enhanced Visible and Infrared Imager) measuring radiances in 12 different spectral channels. Its frequent sampling enables monitoring of rapidly evolving events such as contrails. The MSG satellites also carry a second instrument intended for climate studies: the Geostationary Earth Radiation Budget (GERB). Thanks to its broadband sensor, GERB delivers reflected solar radiation and thermal radiation emitted by the Earth and by the atmosphere.

Also included in MSG is a comprehensive communications payload serving the needs of satellite operations, data communication and user data dissemination. MSG is also equipped with a supplementary Search and Rescue transponder operated by the Cospas-Sarsat Programme which achieves global coverage by having several such transponders on geostationary and other satellites and relays distress signals from ships, aircraft and others in peril.

SEVIRI - Spinning Enhanced Visible and Infra-Red Imager

SEVIRI is the core instrument on board of MSG. It delivers daylight images of the weather patterns plus atmospheric pseudo-sounding and thermal information.

The satellite spins with its sensor at 100 rpm while measuring the Earth's radiation in 12 different channels or wavelengths. SEVIRI scans as shown in Figure 2.6: combining the East-West scan generated by the satellite spin motion and the South to North micro-step scan of a mirror. In each spin it records 3 lines of low resolution channels and 9 lines of the High Resolution Visible (HRV) channel, until the full disk of the Earth is completed. This procedure lasts 12 minutes. Three additional minutes are required for processing and delivering the information to ground stations. A full disk scan can thus be performed every 15 minutes.

MSG-1 (Meteosat-8) is located at 0° longitude and MSG-2 (Meteosat-9) is located 9.5°E so careful handling of the data used in this work is needed in order to avoid mapping problems when combining data from both satellites. Data retrieved are Level 1.5 raw data, in the HRIT format (High Rate Information Transmission) (EUMETSAT, 2005a,b). Data are compressed and coded. For this work their transformation into binary data has been performed through the `xrit2bin` routine developed by Krebs (2006). The conversion from *counts* to radiances is

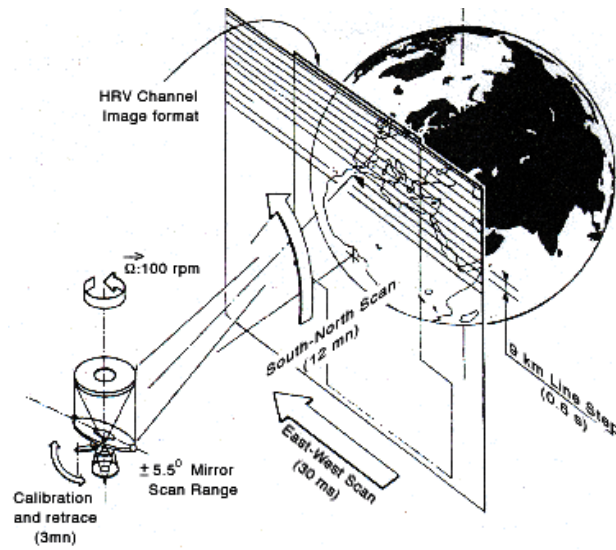


Figure 2.6: SEVIRI's repeat cycle. Source: ESA.

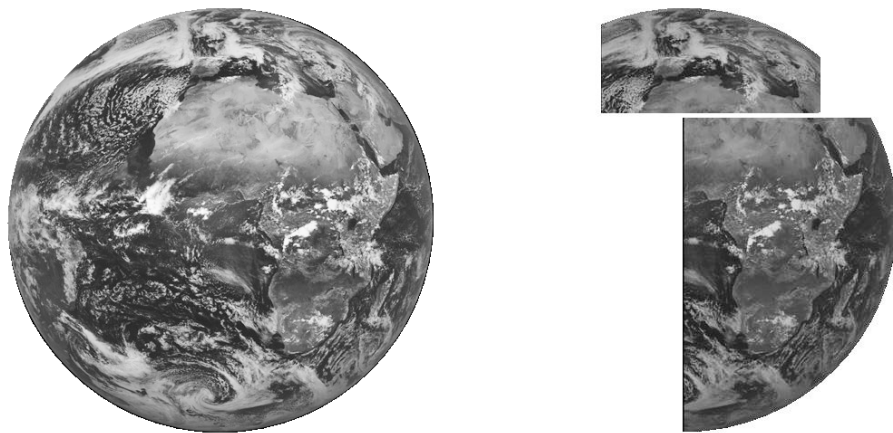


Figure 2.7: Left: Meteosat-8 VIS008 channel. Right: Meteosat-8 HRV channel.

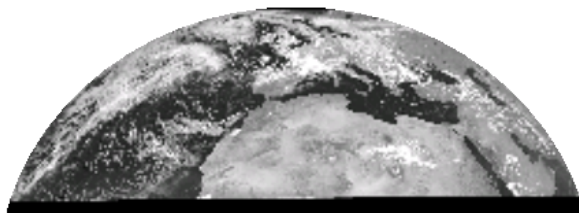


Figure 2.8: Meteosat-8 RSS 5-min scan of reduced area.

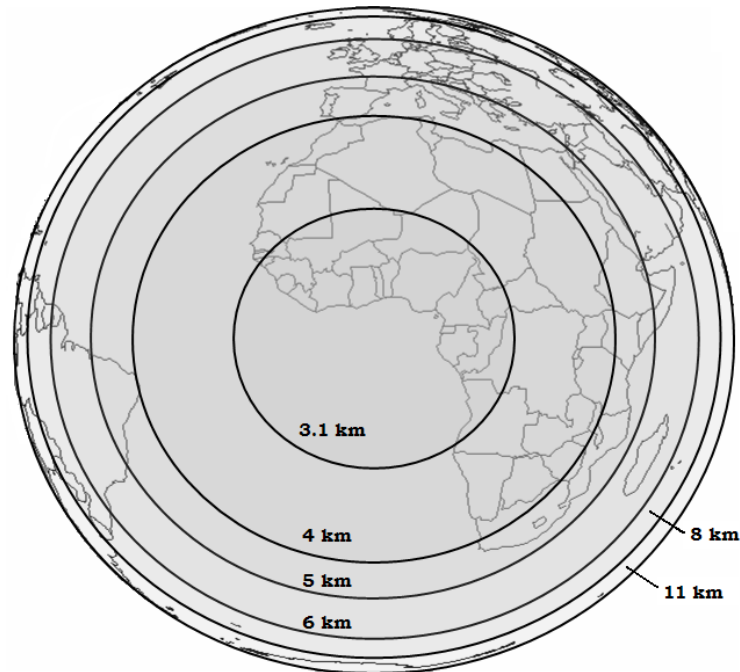


Figure 2.9: Meteosat-8 normalised pixel area. Source: Adapted from EUMETSAT.

performed using calibration coefficients provided by EUMETSAT. The HRV channel has a resolution of 1x1 km at the sub-satellite point and its images are 5568x11136 pixels large (see Fig. 2.7, right), whereas the rest of channels have a resolution of 3x3 km at the subsatellite point and the images are 3712x3712 pixels (see Fig. 2.7, left). Due to the observation geometry, pixel size increases with distance from the sub-satellite point. Pixel size further away from the nadir for low resolution data is shown in Fig. 2.9.

The new Rapid Scan Service (RSS) from MSG-2 (Meteosat-9) which provides data every 5 instead of 15 minutes started mid- 2008 from a position at 9.5°E. The region covered by the rapid scan service ranges from approximately 15°N to 70°N (as shown in Fig. 2.8). These rapid scans are extremely useful for the study of the evolution of contrails because contrails are rapid changing features and rapid scans provide near real-time information facilitating the tracking.

In addition to the high spatial and temporal resolution, SEVIRI also improves the spectral information of the previous Meteosat series. It has four solar/near-infrared channels (HRV, VIS006, VIS008 and IR_016); a channel, IR_039, that provides combined thermal and solar information and seven thermal infrared channels. Infrared channels WV_062 and WV_073 are located in the absorption wavelengths of water vapour; IR_087, IR_108 and IR_120 are located at atmospheric windows and the channel IR_134 is located in an absorption band of CO₂ (see Fig. 2.10). Table 2.1 shows the central wavelength, spectral band and spatial resolution of all twelve SEVIRI channels.

Each of the channels provides unique information about the atmosphere. The contribution of each atmospheric layer to the radiance measured by the satellite sensor can be seen in Figure 2.11, where the weighting functions of the thermal SEVIRI channels are shown for a

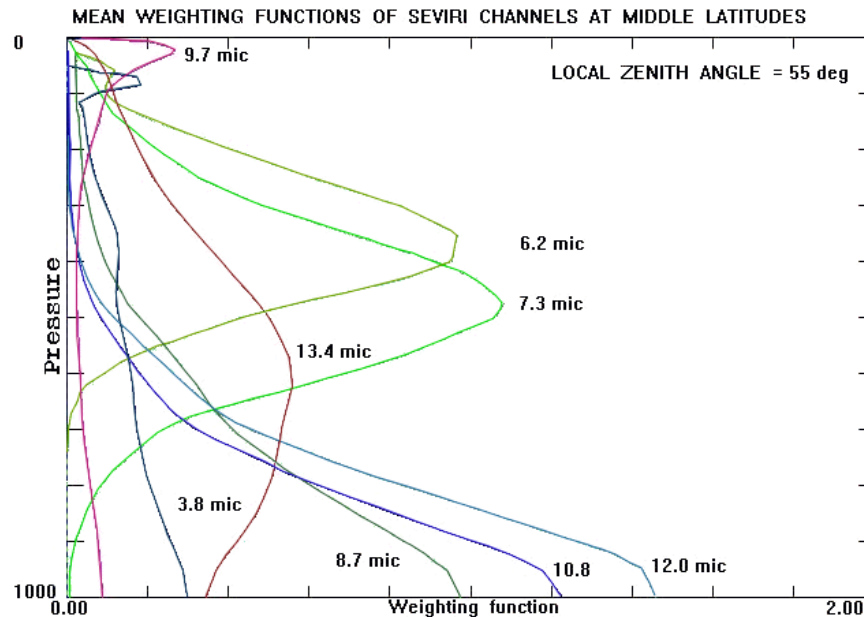


Figure 2.11: Weighting functions of SEVIRI's IR channels. Source: EUMETSAT.

satellite zenith angle of 55° . It can be seen that the weighting functions of the three window channels reach the ground, because the atmosphere is highly transparent for these wavelengths. Infrared channels WV_062 and WV_073 are located in absorption bands of water vapour. This absorption occurs strongly at mid-troposphere levels, and radiances cannot penetrate through the higher absorbing water vapour and these channels do not provide information about the atmosphere's lower layers. Therefore, they are independent of the surface temperature and of the presence of lower clouds, and can be used for discrimination in the retrieval of high clouds, for instance. Channel IR_097 is also called "ozone" channel because it includes an absorption band of ozone, which occurs essentially in the stratosphere. Channel IR_134 is located in an absorption band of CO_2 , which takes place in the lower troposphere providing thus information about the temperature of its lower layers. Channel IR_039 enables the detection of low clouds and fog. Combinations of channels provide further information, for instance, combining channels IR_016 and IR_087 it is possible to derive cloud phase.

When an optically thick cloud is present, it alters the weighting functions. Due to the strong absorption of the cloud, the radiance only contains information from the cloud top and above, but not from the surface. The radiance measured by the satellite can be transformed into brightness temperature of the cloud (see Eq. 2.9). Cirrus are usually optically thin, and the window channels still receive information from the ground. This difficults the measurement of their temperature. In this case, only a combination of channels can provide quantitative information about the cloud temperature or height.

GERB - Geostationary Earth Radiation Budget Experiment

GERB (Harries et al., 2005) is designed to provide accurate measurements of the Earth Radiation Budget (ERB) from a geostationary orbit. GERB data are received at the EUMETSAT ground segment and delivered to the GERB ground stations for processing. Radiances and irradiances are available via internet only four hours after acquisition via the Royal Meteorological Institute of Belgium (RMIB) On-Line Short-term Services (ROLSS)¹.

All Radiation Budget measurements to date have been made from polar orbiting satellites. However, these data cannot provide proper temporal sampling, since they lack the multiple views necessary each day to resolve processes on short time scales. Strong diurnal variations in the radiation budget, particularly over land, in response to the diurnal variation of solar heating are not carefully monitored with such platforms. A number of ERB satellites have been simultaneously available (such as TRMM, Aqua and Terra) allowing 6 observations per day of each region. GERB provides a better temporal sampling, being the only instrument in geostationary orbit that measures broadband radiances for radiation budget studies within time frames of less than an hour. High time resolution measurements of the Earth's radiation budget are very important in the study of rapidly changing processes like clouds. They also provide an important complement to other instruments (polar orbiters) such as CERES.

GERB provides measurements of outgoing longwave radiances and reflected solar radiances and computes the irradiance taking into account the properties of the cloud cover and the type of surface detected by SEVIRI. 24 look-up tables provide information about the cloud phase and optical thickness for six different surface backgrounds and also a cloud mask from SEVIRI data is applied. The irradiance is then calculated from the radiance through Angular Dependency Models (ADMs). In the shortwave range some of CERES' ADMs are used. For longwave irradiance a method based on thermal SEVIRI channels is used.

GERB has two broadband channels (see Table 2.2) achieved through use of a quartz filter. One of them covers the solar spectrum (0.32 - 4.0 μm) and the second covers the solar and thermal parts of the electromagnetic spectrum (0.32 - 30 μm). GERB measures the total radiation and then places a quartz filter in the field of view of the instrument that only allows the solar component of the radiation through. The thermal, or longwave, radiation of the Earth is found subtracting the solar, or shortwave, from the total amount.

Channel	Method	Wavelength (μm)	Sub-satellite point resolution
TOTAL (i.e. thermal + solar)	Filter Out	0.32 - 500	44.6 km x 39.3 km
Shortwave (i.e. solar)	Filter In	0.32 - 4.0	44.6 km x 39.3 km
Longwave (i.e. thermal)	by subtraction	4.0 - 500	44.6 km x 39.3 km

Table 2.2: GERB channels (Harries et al., 2005).

The spatial resolution of GERB is low, approximately half a degree in the sub-satellite point (44.6 km x 39.3 km), but the temporal resolution is only 15 minutes. The instrument uses

¹<http://gerb.oma.be/gerb/ROLSS/rolss.html>

256 distinct detectors arranged approximately North-South with respect to the Earth. One column of an Earth view (256 pixels) is acquired on each rotation of MSG building up a full disk scan from 282 columns in just over 2.5 minutes. Additional time is required for calibration. The scan is repeated every 5 minutes and the data delivered every 15 minutes are an average of three 5-minute scans in order to achieve the required signal-to-noise ratio (Bates et al., 2004).

GERB data used in this work are taken from the Level 2 ARG (Averaged Rectified Geolocated)² package. These images contain unfiltered radiances (broadband reflected solar and emitted thermal) and their associated top of atmosphere (TOA) irradiances. Averaged data are geolocated on the 256x256 pixel Rectified Grid. This data package is in .hdf (Hierarchy Data File) format, so tools for the reading of the data have also been developed in this work.

The validation of the GERB products has been carried out using the most reliable broadband radiometers available on board of satellites: CERES' radiometers. The description of the CERES instrument is to be found in the following section.

2.2.2 Terra - A NASA's Earth Observing System

Terra is a multi-national, multi-disciplinary mission involving partnerships with the aerospace agencies United States, Canada and Japan. It is the flagship of NASA's Earth Observing System (EOS), a series of coordinated polar orbiting satellites designed for long-term global observations. It provides global data on the state of the atmosphere, land, and oceans, as well as their interactions.

Terra's orbit is near-polar and sun-synchronous, descending across the Equator at 10:30 a.m., with a repeat cycle of 16 days. It orbits at an altitude of 705 km and, thus, the spatial resolution of its instruments is better than that of geostationary satellites at 36,000 km height. Nevertheless, even though some overpasses overlap slightly, the type of orbit prevents a thorough study of life cycle of clouds. Terra, that became operational in February 2000, carries a payload of five instruments designed to monitor the Earth's environment and its climate system:

- ASTER (Advanced Spaceborne Thermal Emission and Reflection Radiometer), for close-up land studies, is designed to make detailed maps of land surface temperature, emissivity, reflectance and elevation.
- CERES (Clouds and Earth's Radiant Energy System) measures major elements of the Earth's radiation budget (will be described below).
- MISR (Multi-angle Imaging Spectroradiometer) for bidirectional-reflectance studies of clouds, aerosols and vegetation cover.

²*Geolocation* is the process of assigning a longitude and latitude to each pixel in the GERB image. *Rectification* is the interpolation of the data from the actual known pixel position to an alternative specified grid the spacing of which corresponds to the GERB sampling distance. *Averaged* refers to the final step, where three images in each channel are also *time-averaged* to produce one 15 minute image in each channel

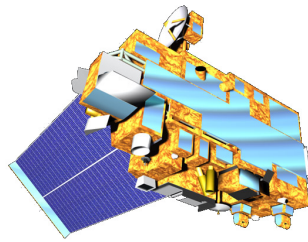


Figure 2.12: Terra satellite. Source: NASA.

- MODIS (MODerate-resolution Imaging Spectroradiometer) one of the most important instruments on board of Terra, with 36 spectral bands designed for the analysis of land, ocean and atmosphere properties and their interactions (further description below).
- MOPITT (Measurements of Pollution in the Troposphere) measures concentration of CO and CH₄ in the atmosphere.

Terra CERES and MODIS data are available at the Langley Research Center (LaRC) web page³.

MODIS - Moderate Resolution Imaging Spectroradiometer

MODIS is a 36-band spectroradiometer providing a wide array of multispectral observations of land, ocean, and atmosphere features on a global basis every 1 or 2 days at spatial resolutions between 250 m and 1000 m. Its spatial resolution improves that of SEVIRI and facilitates the detection of narrower cirrus clouds, but the temporal resolution is insufficient for the study of contrail evolution. It was launched into Earth orbit by NASA in 1999 on board the Terra (EOS AM) Satellite, and in 2002 on board the Aqua (EOS PM) satellite.

The MODIS instrument consists of a cross-track scan mirror and collecting optics, and a set of linear arrays with spectral interference filters located in four focal planes. The optical arrangement provides imagery in 36 discrete bands (see Table 2.3) between 0.4 and 14.5 μm and at varying spatial nadir resolutions (2 bands at 250 m, 5 bands at 500 m and 29 bands at 1 km). The system also includes four on-board calibrators.

Besides radiances, MODIS also provides an enormous variety of Level 2 products such as aerosol optical thickness, cloud microphysics, total precipitable water, total column ozone, cloud mask, stability indices, etc. The MODIS cloud mask and the MODIS optical thickness will be used in different stages of this work. To derive a cloud mask, MODIS requires radiances from 14 spectral bands: visible bands 1 and 2, near-infrared bands 5 and 6 and infrared bands 17-21, 26-29, 31, 32, 33 and 35. Additionally, several ancillary data are needed: sun zenith angle, azimuthal angle, viewing angle, land/water mask, topography, ecosystems, snow/ice mask and sea ice coverage (Ackerman et al., 2006). To retrieve the

³<http://ladsweb.nascom.nasa.gov/>

Primary use	Band	Bandwidth
Land/cloud/aerosols boundaries	1	620 - 670
	2	841-876 nm
Land/Cloud/Aerosols Properties	3	459 - 479 nm
	4	545-565 nm
	5	1230-1250 nm
	6	1628-1652 nm
	7	2105 - 2155 nm
Ocean Colour Phytoplankton Biogeochemistry	8	405 - 420 nm
	9	438 - 448 nm
	10	483 - 493 nm
	11	526 - 536 nm
	12	546 - 556 nm
	13	662 - 672 nm
	14	673 - 683 nm
	15	743 - 753 nm
Atmospheric Water Vapour	16	862 - 877 nm
	17	890 - 920 nm
	18	931 - 941 nm
Surface/Cloud Temperature	19	915 - 965 nm
	20	3.660 - 3.840 μm
	21	3.929 - 3.989 μm
	22	3.929 - 3.989 μm
Atmospheric Temperature	23	4.020 - 4.080 μm
	24	4.433 - 4.498 μm
Cirrus Clouds and Water Vapour	25	4.482 - 4.549 μm
	26	1.360 - 1.390 μm
	27	6.535 - 6.895 μm
Cloud Properties	28	7.175 - 7.475 μm
	29	8.400 - 8.700 μm
Ozone	30	9.580 - 9.980 μm
	31	10.780 - 11.280 μm
Surface and Cloud Temperature	32	11.770 - 12.270 μm
	33	13.185 - 13.485 μm
Cloud Top Attitude	34	13.485 - 13.785 μm
	35	13.785 - 14.085 μm
	36	14.085 - 14.385 μm

Table 2.3: MODIS channels.



Figure 2.13: CERES scan modes: Blue: RAP, White: cross-track, Red: along-track. Source: NASA.

cloud optical thickness, MODIS uses a radiative transfer model to build a lookup table and searches the combination of optical thickness and effective radius that gives the best fit for each pixel (King et al., 2007).

CERES - Clouds and the Earth's Radiant Energy System

Clouds and the Earth's Radiant Energy System, CERES, is a broadband scanning thermistor bolometer package aimed at providing information about the Earth's radiative budget (Wielicki et al., 1996). CERES measures the radiative flows at the top of atmosphere (TOA). Combining these data with data from higher spatial resolution narrowband imagers such as MODIS, it is possible to calculate cloud properties and irradiances through the atmosphere as well as the radiative energy budget at the Earth's surface. CERES is controlled at the NASA's Langley Research Center and is on board several satellites such as Terra, Aqua and TRMM.

The first 24 months of CERES data collected on both TRMM and Terra demonstrate that the CERES instruments present an extremely high radiometric measurement precision and accuracy. It has been validated by a large number of products (Charlock and Alberta, 1996). The Terra spacecraft carries two identical CERES instruments, which enable different scan modes simultaneously. There are three possible scanning modes (see Fig. 2.13) that can operate in pairs. The main scanning modes are: fixed azimuth crosstrack scan (optimising spatial sampling over the globe) and rotating azimuth plane (RAP) (providing angular sampling of the entire hemisphere of radiation. The RAP mode is used to improve ADMs and thus the accuracy of the final fluxes of solar and thermal energy used to derive the Earth's radiation budget). The ADMs used are thoroughly described in (Loeb et al., 2005) and their validation is described in (Loeb et al., 2003). The third mode is an along-track scan used to maximise the number of viewing angles of a particular region. It is primarily used for validation purposes and is typically activated every 15 days on the RAP scanner.

Each CERES instrument has three channels (see Table 2.4) measuring the Earth's radiation budget and providing estimates of cloud properties to establish their effect on the radiative fluxes from the surface to the TOA. The shortwave channel ($0.3 - 5.0 \mu\text{m}$) measures reflected sunlight, the longwave channel measures Earth-emitted thermal radiation in the 8-12 μm "window" region to improve the flux estimates in clear sky conditions, and the total channel (0.3 to $> 200 \mu\text{m}$) measures all wavelengths of radiation. Longwave outgoing radiation is

Channel	Wavelength (μm)	Nadir resolution
Total	0.3 - >200	20 km
Shortwave	0.3 - 5.0	20 km
Window (LW)	8 - 12	20 km
Longwave	5.0 - 200	20 km

by subtraction

Table 2.4: CERES channels (Minnis et al., 1997).

retrieved as in GERB subtracting the shortwave contribution from the total channel (Minnis et al., 1997).

The spatial resolution of CERES is 20 km at nadir, notably better than that of the GERB instrument (44.6 x 39.3 km), but with the temporal resolution characteristic of a polar orbiting sensor.

Table 2.5 summarises the characteristics of all data used in this work. It can be seen that a combination of both geostationary and polar orbiting narrowband instruments is strongly advised, because the former have better temporal resolution and the latter, better spatial resolution. The spatial resolution of the broadband instruments GERB and CERES is not sufficient to determine the radiative forcing of contrails, which arises the need for a narrowband-to-broadband conversion based on the SEVIRI instrument.

Instrument	Narrowband instruments		Broadband instruments	
	SEVIRI	MODIS	GERB	CERES
Altitude	36000 km	705 km	36000 km	705 km
Spatial resolution at nadir	3x3 km	1 km	50 km	20 km
Temporal resolution	5 min	1/day*	15 min	1/day*

Table 2.5: Approximate characteristics of data used. * Temporal resolution of Terra is latitude-dependent, ranging from 16 times/day at the poles to only once a day over the Equator.

Chapter 3

Methods

This chapter describes a tracking algorithm designed to study the life cycle of contrail-cirrus (see Section 3.1). The algorithm uses satellite data with a high temporal resolution that cover a region of the Earth where air traffic is frequent: SEVIRI Rapid Scan data. It is designed to monitor the development of contrails from their formation to their final dissolution. The objective of this work is to combine the output of the algorithm with methods developed to retrieve the physical properties of contrails (radiative forcing and optical thickness). This will offer for the first time measurements of the effect on the climate system of not only linear contrails but also of other aviation induced clouds. These would not have been considered anthropogenic otherwise because they lack the characteristic linear shape.

To derive the radiative forcing, measurements of the irradiances at top of atmosphere are needed. The algorithms used for retrieving irradiances from SEVIRI data were developed by B. Mayer and H. Mannstein. These algorithms perform the narrowband-to-broadband conversion and the angular integration necessary to obtain broadband irradiances from SEVIRI narrowband measurements. The algorithms are described in Sections 3.2 and 3.3 and have been validated in this work (see Section 3.4.2) for their subsequent use. The method to retrieve the radiative forcing is described in Section 3.5. The optical thickness retrieval algorithm is described and discussed in Section 3.6.

3.1 Automatic Contrail Tracking Algorithm: ACTA

This section describes the method designed to identify the pixels that belong to a contrail-cirrus using satellite data with high temporal and spatial resolution, from the first occurrence of the linear contrail to the final dissolution of the aviation-induced cirrus cloud. First, linear contrails are detected in a high resolution MODIS image, using the well-established algorithm developed by Mannstein et al. (1999). Second, the detected contrails are tracked forwards and backwards in time with the newly developed ACTA algorithm, exploiting the high temporal resolution of the SEVIRI sensor.

3.1.1 ACTA: input. Contrail Detection Algorithm

To detect the position of linear contrails in MODIS data, the contrail detection algorithm (CDA) developed by Mannstein et al. (1999) is used. It is a fully automated method based on a combination of infrared channels designed to identify linear contrails on satellite images. Contrails are usually hard to distinguish from the background due to their low optical thickness and coverage. Therefore, a contrail detection algorithm must be a sensitive tool that consequently has a high probability of misdetections (Meyer et al., 2002). In principle, false alarms (the amount of pixels falsely classified as contrails) may occur through real image features that look similar to contrails, or through data errors that accidentally can produce contrail-like structures. The CDA is designed to have a low false alarm rate (ideally 0) at the expense of the detection efficiency (the ratio of the amount of correctly classified contrail pixels to the full amount of true contrail pixels, ideally 1).

The CDA used is based both on the brightness temperature difference between $10.8 \mu\text{m}$ and $12 \mu\text{m}$, and on the $12 \mu\text{m}$ brightness temperature. Data are normalised to apply constant thresholds for all scenes using an adaptive highpass filter. The sum of both normalised images is screened for contrails by line shaped filters with a kernel size of 19×19 pixels in 16 different directions to include all possible orientations of the contrails. For each orientation, those structures that fulfil a given set of geometrical and physical thresholds are labeled as contrails. The physical thresholds are related to the sum of the normalised images, to the brightness temperature difference and to the gradient of the temperature in channel $12 \mu\text{m}$, and are sensor-dependent (Mannstein et al., 1999). The geometrical thresholds are related to the length, the coverage and the linearity of the contrail.

The CDA described in Mannstein et al. (1999) was initially developed for the NOAA-AVHRR instrument. For this work it has been adapted to the MODIS instrument including a water vapour channel. This channel provides information above the pressure level of approximately 500 hPa (see the weighting functions in Fig 2.11), so it can be used to eliminate linear features on the surface such as coastlines, rivers and low level cloud streets. Moreover, the lower limit of the length of the contrail has been raised from the initial 15 AVHRR pixels to 47 MODIS pixels (both pixel sizes are similar), to reduce the number of misdetections. The minimum number of pixels required to identify a contrail is set at 19 MODIS pixels, and the geometric threshold forces the alignment of the contrail pixels to present a correlation coefficient larger than 0.975. As the length threshold is larger than the number of pixels threshold, the contrail may be a non-connected structure. The CDA has been tuned to have a lower false alarm rate and, therefore, an inevitably low detection efficiency to ensure that all structures handled during this work are real contrails. Despite this drawback, the amount of contrails detected is large enough to perform an statistical analysis. To accurately study the effect of aviation induced clouds on the climate system, it is preferred to use a smaller number of real contrails rather than to include a larger number of misdetections (that may include natural cirrus). As discussed later (Section 3.1.3), this reduces the amount of contrails studied to the ones identified by the CDA.

3.1.2 ACTA: description

The Automatic Contrail Tracking Algorithm, ACTA, focuses not only on linear contrails but also on aged contrail-cirrus: man-made clouds that were linear once but have lost their linear shape with time. Linear contrails can be identified on satellite images with line-searching algorithms such as the CDA (see Section 3.1.1), but older contrail-cirrus provide less easily identifiable signals on a satellite image (see Fig. 3.1). ACTA exploits the fact that contrails retain part of their linear structure as they age, and although wind shear and spreading can modify their shape, at least a part of the contrail-cirrus can be fitted by a straight line. It resembles the process a human observer would use: identify a contrail thanks to a group of partially aligned pixels providing a strong BTD signal to the sensor and lying close to the position of that contrail in the previous image. The tracking of a contrail is a complex task because contrails change in position and shape between two consecutive satellite images. SEVIRI rapid-scan data have been used in this work because, within a 5-minute time lapse, neither the shape nor the position of the contrail present major changes.

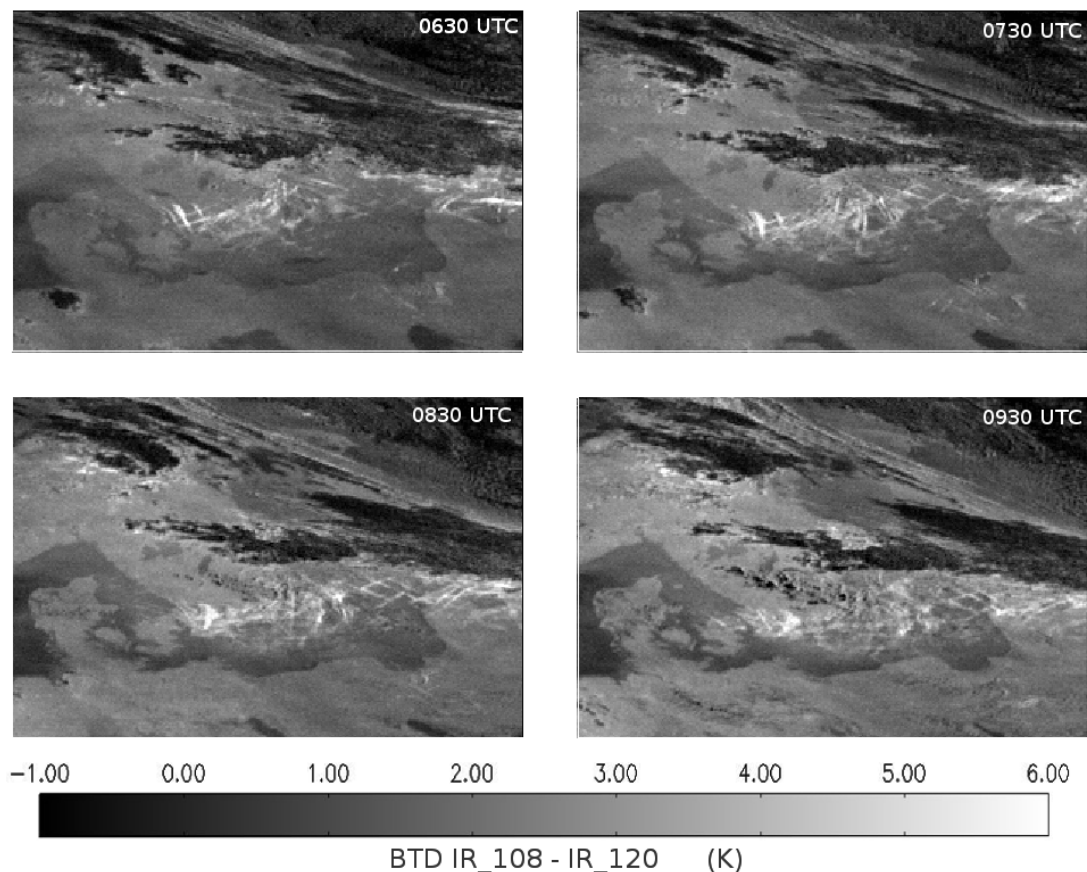


Figure 3.1: Four examples of BTD images showing the evolution of contrails over southern Sweden over three hours. 0630 UTC: contrails appear as linear structures with a high BTD signal (light grey - white). It can be seen that the older contrails are, the more difficult is to identify them as such without temporal information. Date: 3/Jul/09.

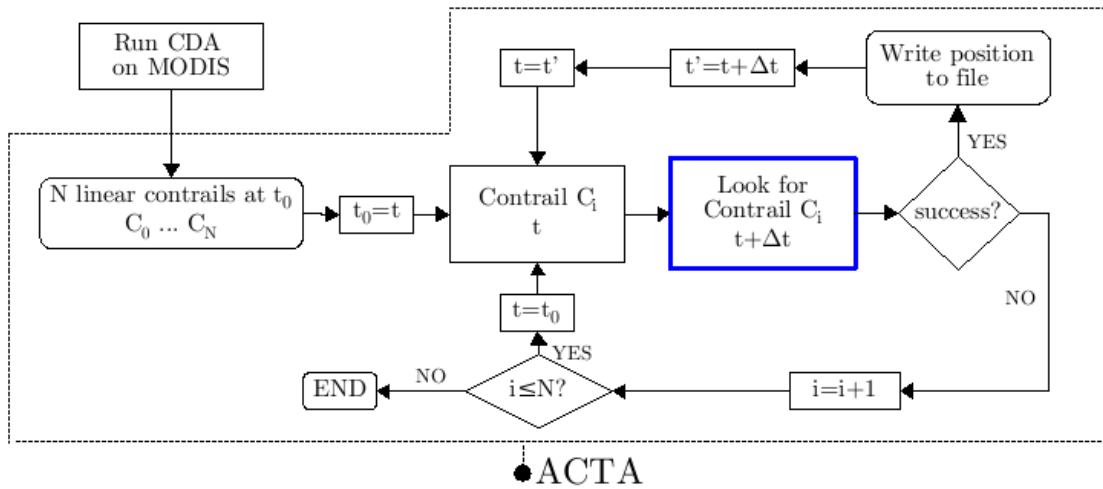


Figure 3.2: Schematic representation of ACTA. Input: list of linear contrails detected by the CDA on MODIS.

Fig. 3.2 shows a schematic outline of ACTA. Running CDA on a MODIS image provides a list of N linear contrails at time t_0 as input to ACTA (see an example of this input in Fig. 3.3). This input contains the geographical position of the two end points of each linear contrail detected by the CDA. The latitude and longitude of both ends are used to map the contrail on the SEVIRI grid, making a parallax correction assuming a theoretical height of 10 km for the contrail. Based on the position of the contrail C_i at time t , $C_i(t)$, ACTA looks for C_i in the following SEVIRI image, at time $t + \Delta t$, $C_i(t + \Delta t)$. If it is found, then ACTA uses the information about the new position to iterate the process, with $t + \Delta t$ as initial time. Once the contrail cannot be tracked any longer, ACTA proceeds to the next contrail on the input list.

A very important feature of ACTA is that it is applied forwards and backwards in time. The algorithm takes the first input from CDA at time t , the time of the MODIS overpass, and then tracks each contrail with positive or negative time increments (Δt), i.e. it tracks equally back to the past and forth to the future. Thus, the contrail lifetime can be determined, from its first detection in satellite at time $t - n\Delta t$ until it can no longer be discriminated from its surroundings by the satellite at $t + n'\Delta t$, regardless of the MODIS overpass time.

To perform the tracking, ACTA uses the brightness temperature difference (BTD) between channels IR_108 ($10.8 \mu\text{m}$) and IR_120 ($12.0 \mu\text{m}$) of SEVIRI. As it can be seen in Fig. 3.1, contrails are easier to identify in those images because they have a larger BTD than the surroundings. This channel combination has long been used to identify thin clouds, especially thin cirrus. Ice crystals behave differently in those two wavelengths while other atmospheric and surface properties are similar for both channels (Lee, 1989). The exclusive use of infrared channels in the design enables the algorithm to run indistinctly on day and nighttime scenes.

0	60.5833	-56.2446	60.2379	-54.9474	69.5701
1	58.7723	-51.2684	58.3933	-50.1702	76.2430
2	58.4218	-50.6467	58.0765	-49.8008	62.0322
3	57.3055	-51.1648	57.4103	-50.1245	61.2944
4	56.7138	-49.4408	56.5904	-50.6570	71.1969
5	56.5365	-48.9268	56.4056	-50.1770	72.2011
6	56.3608	-51.7426	56.1360	-53.3517	100.344
7	54.7573	-54.0794	54.9307	-52.7444	85.8836
8	54.7718	-52.3320	54.6192	-53.7741	92.1358
9	53.5748	-54.9242	53.7873	-53.7090	81.6333
10	56.9389	-48.0549	56.6901	-49.6270	91.2140
11	56.5007	-49.2015	56.7149	-47.6743	86.4002
12	56.1503	-48.3321	56.3899	-46.1906	113.406
13	55.9850	-47.8665	56.1578	-46.3629	79.0253
14	56.2930	-52.0901	56.6550	-50.2551	115.603
15	54.7224	-43.9298	54.6238	-45.2470	58.6941
16	54.7686	-52.0808	55.0279	-51.0284	70.1783
17	54.5084	-54.9504	54.2256	-55.8822	65.8559
18	54.2828	-55.2017	54.0384	-56.1482	64.8151
19	53.6036	-54.0381	53.2945	-55.1776	81.0555
20	51.8710	-48.1554	51.5454	-50.2094	117.593

Figure 3.3: Example of CDA output that will be used as input for ACTA. Column 1 is the contrail ID. Columns 2-3 are latitude and longitude ($^{\circ}$) of the contrail starting point. Columns 4-5 are latitude and longitude ($^{\circ}$) of the contrail end point. Column 6 is the length of the contrail (km)

Briefly, the process of finding the contrail $C_i(t + \Delta t)$ (in blue in Fig. 3.2) consists in two steps (see detailed flowchart in Fig. 3.4 and a more detailed explanation in the following pages):

- In Step I, ACTA aims to link the contrail at start time t with its corresponding position at time $t + \Delta t$ by finding a line that identifies the core of the contrail. For that purpose, an enhanced BTD image is produced and the pixels providing a signal stronger than a given threshold are selected. These pixels are called *guide points*. Then, a line is fitted through the guide points. Step I succeeds when the fit fulfils an acceptance criterion that ensures that the line found at $t + \Delta t$ corresponds to the same contrail as the line at t .
- In Step II, ACTA's task is to establish the contrail shape at $t + \Delta t$. ACTA uses the information of the position of the line at time $t + \Delta t$ (Step I) as input to define a region in which to search for the rest of the pixels that also belong to the contrail. Through a combination of image processing techniques and BTD information, the pixels belonging to the contrail are retrieved. The output of Step II, and therefore of ACTA, is at least one group of at least three connected pixels. Depending on the latitude and longitude, a connected region of 3 pixels in the area under study corresponds to an area of 50-200 km².

After both steps are successfully performed, ACTA writes the output (the contrail pixels) to a file and proceeds to the following iteration (i.e. the new start time is $t + \Delta t$) using as start and end points the position of the westernmost and the easternmost pixels detected in Step II. If the line parameters cannot be found, the tracking stops.

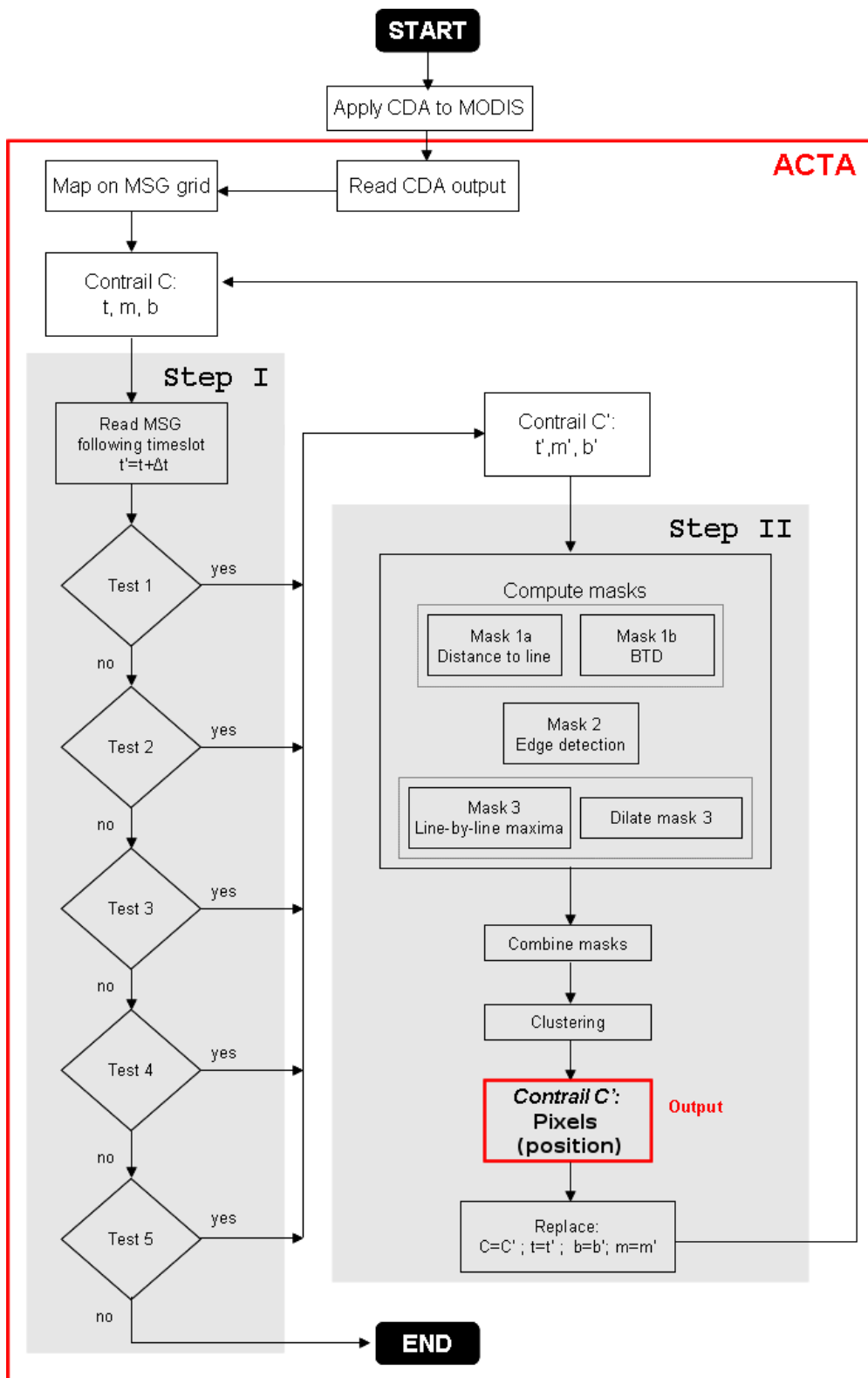


Figure 3.4: Schematic overview of ACTA. Input for Step I is the MODIS detected contrail at t . After Step I, m and b , the coordinates of a $y = mx + b$ line are used as input for Step II. Output of Step II are the pixels that belong to the contrail at $t + \Delta t$.

Step I

From a satellite point of view, a contrail is essentially a group of pixels with a stronger BTD signal than the surroundings, similar to a cirrus cloud but with a distinct evolution pattern. When the contrail is young, those pixels are strongly aligned. The group may change shape as it ages, but it will always retain part of its former linear shape. Therefore, a contrail can be tracked by locating that linear part throughout its lifetime. Let $C(t)$ be the contrail at t and $C(t + \Delta t)$ the same contrail at $t + \Delta t$. As $C(t)$ and $C(t + \Delta t)$ are the same contrail, the slope and intercept of the line that corresponds to $C(t + \Delta t)$ through the fit of the guide points will be related to the slope and intercept of the line that corresponds to contrail $C(t)$. To establish the parameters of the line that corresponds to contrail $C(t + \Delta t)$ from the parameters of the line that corresponds to contrail $C(t)$, Step I performs a set of five consecutive tests. Each test has the same structure but different internal variables, and is designed to take into account various atmospheric and surface conditions. Fig. 3.5 shows a short flowchart of a test in Step I and Fig. 3.6 shows a real example.

In each test, one input is the position of the line corresponding to the desired contrail on the BTD image at t . This information is used to define a search region where the contrail drifted by the wind within a time interval Δt can be found. A second input is the BTD image at $t + \Delta t$. This image is enhanced through filtering and *guide points* are determined within the wind field-defined region using a certain threshold on the enhanced BTD image. Next, a line is fitted through the guide points. The parameters used to characterise the line are its slope, m , and intercept, b . The test succeeds when the line derived by the guide points fulfils the corresponding acceptance criterion. This criterion has very restrictive conditions regarding either the orientation of the line, or the alignment of the pixels, or both. Each test works following the above described process but with different widths for the wind field-defined region, different filters for enhancing the BTD image, different criteria to look for guide points and different acceptance criteria for the regression.

Next, a thorough definition of the internal test variables (shaded boxes in Fig. 3.5) is given. Then, their thresholds and combination in each of the tests is explained. Finally, an example is shown where all five tests have been used.

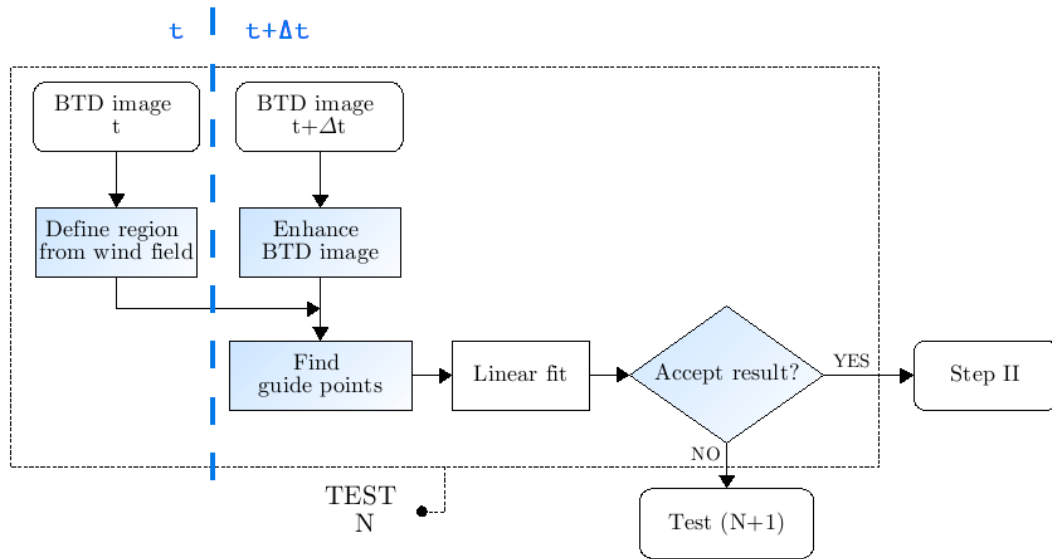


Figure 3.5: Schematic representation of a Test in Step I. Inputs: Contrail position in the BTD image at t and BTD image at $t + \Delta t$. Each shaded box has different internal thresholds/definitions in each test. The output (input for Step II) is the position of the line at $t + \Delta t$.

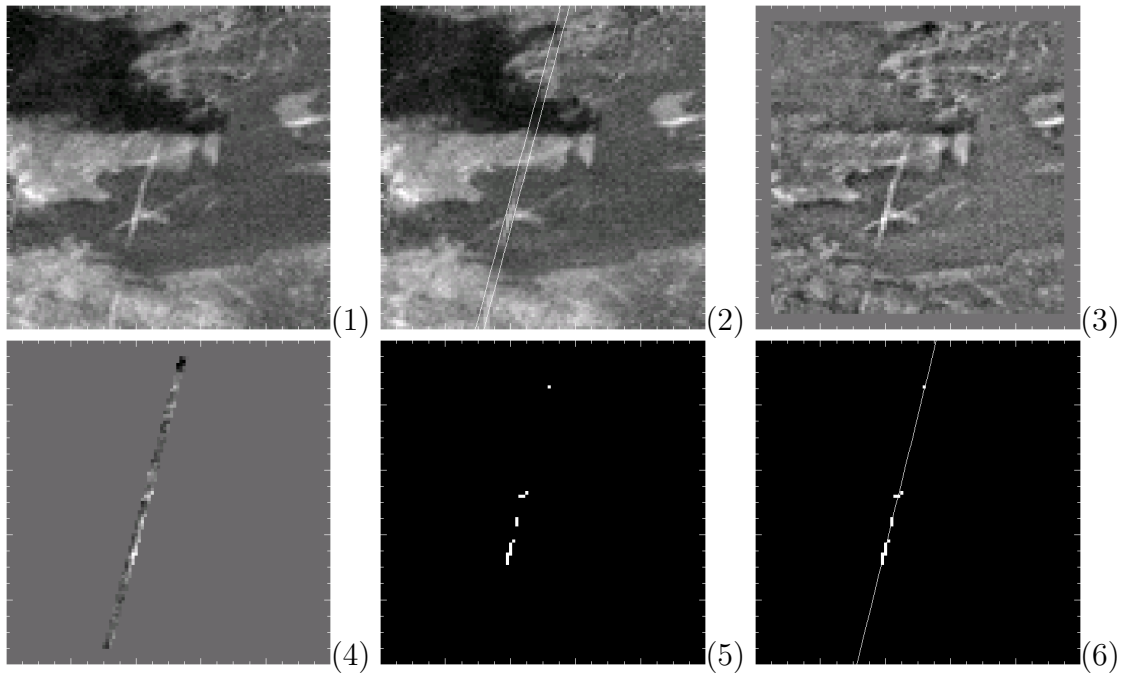


Figure 3.6: Test 3. 1: Scene at time t with contrail $C(t)$ in the centre of the image. 2: Same scene at time $t' = t + \Delta t$, contrail $C(t')$ in the centre of the image between the white lines that delimit the area where C can lie after being drifted by the wind. 3: Enhanced BTD image. 4: Selected wind field related region over the enhanced image. 5: Guide points. 6: Linear fit.

*Wind field-defined region*¹

First, to find $C(t + \Delta t)$ from the information provided by $C(t)$, ACTA selects a region, B_{ij} , where $C(t + \Delta t)$ could exist. This region must be consistent with the wind field at the contrail height (see Fig. 3.7). At a typical altitude of 10 km, and with a Δt of 5 minutes, the wind drifts the contrail approximately 10 km from its original position (depending on the speed of the wind and on the latitude and longitude, this corresponds to 2 or 3 pixels). Moreover, the wind field at flight-level height is mainly West - East, so the contrail will be most likely drifted eastwards in the region under study.

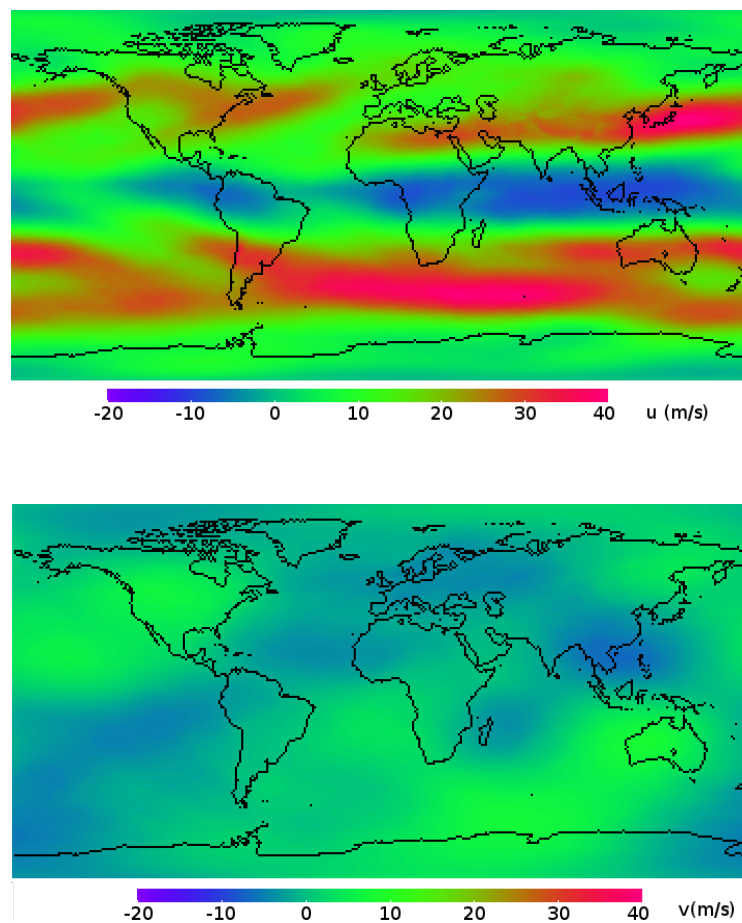


Figure 3.7: Annual mean (2007) zonal (top) and meridional (bottom) components of the wind field at approximately 10 km height. Source: ECMWF (European Centre for Medium-Range Weather Forecasts)

¹Throughout the section, A_{ij} or $A(i, j)$ denote matrices of $N_i \times N_j$ elements. Multiplication (\cdot) does not imply matrix multiplication but Hadamard (or Schur) product: elementwise multiplication of their elements, therefore $A_{ij} \cdot B_{ij} = B_{ij} \cdot A_{ij}$.

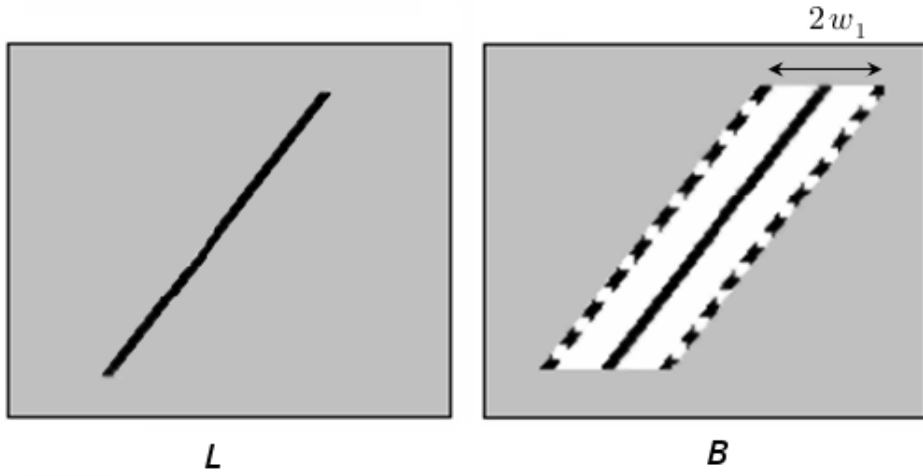


Figure 3.8: Left: 2-dimensional array L with the line corresponding to contrail C . Right: 2-dimensional array B with the area (white) in which contrail $C(t + \Delta t)$ is expected to be found.

To establish the allowed region at time $t + \Delta t$, the starting point is the line that corresponds to the contrail at time t ($y = mx + b$). The length of the line is limited by $x = i_0$ and $x = i_1$. In the first iteration, i_0 and i_1 are given by the westernmost and easternmost points of the contrail ± 10 pixels. These loose boundary conditions allow the contrail to grow and adjust its length, in case the CDA has not provided the full length of the contrail. In further iterations, i_0 and i_1 are issued from the output of Step II. The line is placed on a 2-dimensional array L_{ij} of the same size as the BTD image (see Fig. 3.8, left):

$$L_{ij} = \begin{cases} 1 & , \forall(i, j) \mid j = f(mi + b) \quad , i_0 < i < i_1 \\ 0 & , \text{otherwise} \end{cases} \quad (3.1)$$

where $f(x) = \text{round}(x) = \lfloor x + 0.5 \rfloor = \max\{n \in \mathbb{Z} \mid n \leq x\}$ rounds x to the nearest integer.

Then, the region of width $2w_1$ (test-dependent, see Table 3.1) where the contrail can move from its position at time t to its new position at time $t + \Delta t$, can be defined by shifting L w_1 pixels eastwards and w_1 pixels westwards (see Fig. 3.8, right).

$$B_{ij} = \sum_{k=0}^{2w_1} L(i - w_1 + k, j) \quad , \forall(i, j) \quad (3.2)$$

Enhanced BTD image

To enhance the contrail structures and eliminate most of the background information, ACTA applies a high-pass filter to the BTD image. First, the BTD image at $t + \Delta t$ is smoothed using a boxcar filter. Let BTD_{ij} be the BTD image, and let w_2 be the width of the filter (test-dependent, see Table 3.1). The filtered image, F_{ij} , then equals:

$$F_{ij} = \begin{cases} \frac{1}{2w_2} \sum_{p=0}^{w_2-1} \sum_{q=0}^{w_2-1} BTD(i - \frac{w_2}{2} + p, j - \frac{w_2}{2} + q) & , i = \frac{(w_2-1)}{2}, \dots, N_i - \frac{(w_2+1)}{2} \\ & j = \frac{(w_2-1)}{2}, \dots, N_j - \frac{(w_2+1)}{2} \\ BTD_{ij} & , \text{otherwise} \end{cases} \quad (3.3)$$

Finally, ACTA uses this information to produce an enhanced image, $BTD_{ij} - F_{ij}$, and focuses on the allowed region by multiplying by B_{ij} (see Eq. 3.2).

$$S_{ij} = B_{ij} \cdot (BTD_{ij} - F_{ij}) \quad (3.4)$$

The matrix S_{ij} now contains the enhanced BTD values in the region shown in Fig. 3.8, right, and otherwise, 0.

Guide points

ACTA looks in S_{ij} for the pixels that provide a stronger signal. Those points are called *guide points*, $(i, j)_0 \dots (i, j)_n$, and fulfil an empirically derived threshold, $CRIT$:

$$\text{guide points} = \{(i, j) \mid S_{ij} > CRIT\}, \quad (3.5)$$

where $CRIT$ is a test-dependent scalar, see Table 3.1.

Acceptance criterion

If there are less than three guide points, ACTA stops the current test and proceeds to the following test. If three or more guide points are present, a linear regression is performed and a final criterion, *acceptance criterion*, must be fulfilled. The acceptance criterion is test-dependent (see Table 3.1) and specifies empirically defined requirements regarding either the correlation coefficient issued from the fit, R^2 , (*alignment criterion*), or the orientation of the line with respect to the former orientation at time t (*orientation criterion*), or both. If the linear regression fulfils the requirements, the position of the line issued from this regression is written to a file and will be used as input for the next iteration. Otherwise, ACTA proceeds to the following test.

The *orientation* criterion means that the orientation of the line that guide points define must not differ by more than 2.8° from the orientation of the line in the previous timestep. The *alignment* criterion means that the correlation coefficient of the fit through the guide points must be larger than 98%.

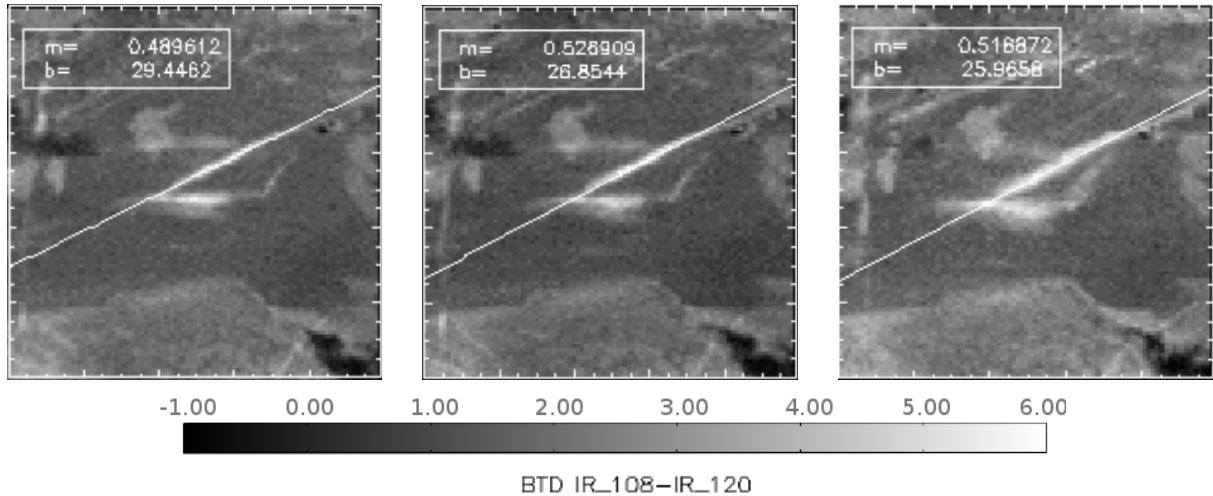


Figure 3.9: Output of Step I: Contrail with its corresponding line at different stages of its development. On each plot, the line $y = mx + b$ equation parameters. Left: at time t . Centre: at time $t+25$ min. Right: at time $t+55$ min. Background: BTD image $10.8 \mu\text{m} - 12.0 \mu\text{m}$, in K

Test	Region ($W1$)	Filter width ($W2$)	Guide points threshold ($CRIT$)	Linear regression <i>acceptance criterion</i>
1	5 pixels	2 pixels	1K	orientation
2	5 pixels	10 pixels	1.3K	alignment
3	2 pixels	2 pixels	1K	orientation
4	2 pixels	6 pixels	1K	alignment and orientation
5	2 pixels	10 pixels	scene-dependent (*)	alignment

Table 3.1: Description of ACTA's Step I tests. (*) See explanation in text below (description of Test 5).

When this first step is over, contrail $C(t+\Delta t)$ is assigned the parameters of its corresponding line. Fig. 3.9 shows three different stages of the evolution of a contrail with their corresponding lines. This information is stored and used for the next iteration at time $t + 2\Delta t$. After each assignment, ACTA proceeds to Step II to derive the shape of the contrail.

The different internal variables in each test (w_1 , w_2 , $CRIT$ and those for the *acceptance criterion*) have been established empirically. They are summarised in Table 3.1 and explained in detail in the following pages. If all tests provide a negative answer, the tracking stops.

The sequence of the tests is designed to identify contrails in images of increasing difficulty. Isolated contrails are easier to track than contrails surrounded by other cirrus clouds or contrails nearby. Moreover, the younger the contrail is, the more linear its shape appears in the BTD image and the easier the tracking is. Typically, Step I ends successfully already after the first or second test, depending on the image. These test are designed to identify easily recognisable contrails, narrow structures with a strong BTD signal. Besides, the region defined in tests 1 and 2 is wide enough to allow the tracking of the contrail even if the wind

field is particularly strong and drifts the contrail far away. When the scene is too complex because of neighbouring contrails or other surrounding clouds crossing the tracked one, tests 1 and 2 do not provide conclusive results because they focus on a large region that may include structures other than the desired contrail. Therefore, ACTA looks for the contrail in narrower regions, such as in the tests 3 and 4. These tests are designed for complicated cases and prevent other clouds' pixels from being selected as contrail pixels. In particular, they impose strong requirements on the width of the wind field-defined region and on the acceptance criterion for the line parameters. The presence of alien pixels would modify too much the orientation of the contrail. Finally, ACTA's Test 5 is usually applied to scenes with poor contrast, typically when a vanishing contrail must be distinguished from the (similar) background.

Test 1

The first of the five tests uses a narrow smoothing filter providing an only slightly smoothed BTM image at $t' = t + \Delta t$. The wind field-related region defined by the contrail at t is wide enough so that the whole contrail $C(t')$ lies in it. The acceptance criterion for the line is based on the comparison of the orientation of the new line (at t') with the orientation of the line at t . Due to the nature of the wind field, the orientation criterion ensures that the line identified corresponds to the desired contrail and not to a different contrail crossing the scene or to other natural structures present at t' .

$w_1 = 5$ pixels, $w_2 = 2$ pixels, $CRIT > 1K$,
Acceptance criterion: $m - 0.05 < m' < m + 0.05$ (orientation within 2.8°)

Test 2

If Test 1 does not succeed, a second test is performed. Within the same pixel neighbourhood as in the prior test, a stronger filter is applied. Therefore, only the more relevant pixels are retained. In this case, the acceptance criterion of the linear fit is the alignment of the guide points (correlation coefficient).

$w_1 = 5$ pixels, $w_2 = 10$ pixels, $CRIT > 1.3 K$,
Acceptance criterion: $R^2 > 98\%$

Test 3

The third test is similar to the first one but constrains the existence of the contrail $C(t' = t + \Delta t)$ to a narrower neighbourhood to reduce the possibility that the contrail guide points have been misidentified or outnumbered by strong BTM signals from surrounding cloudiness in the prior tests. According to the typical wind speed at 10 km height, the contrail $C(t')$ must lie within this narrow region. In this case, the image at t' is filtered with the same filter as in Test 1. The combination of a weak filter with a narrow neighbourhood has the advantage of allowing more image features to be recognised than in Test 2 while preventing that other cirrus clouds present and too close to the desired contrail mislead the identification of guide points. The acceptance criterion for the regression is, as in Test 1, the orientation.

$w_1 = 2$ pixels, $w_2 = 2$ pixels, $CRIT > 1 K$,
Acceptance criterion: $m - 0.05 < m' < m + 0.05$ (orientation within 2.8°)

Test 4

The fourth test is a combination of Tests 2 and 3. Not only the alignment of the guide points is assessed (through the correlation coefficient) but also the inclination of the line corresponding to $C(t' = t + \Delta t)$ with respect to the line corresponding to $C(t)$. The smoothing in this case is performed with a filter of intermediate width to eliminate most of the background noise and identify structures that are too weak for Test 2 but in a scene that is too complex (regarding neighbouring contrails or cirrus clouds) for Test 3.

$$w_1 = 2 \text{ pixels}, w_2 = 6 \text{ pixels}, CRIT > 1 \text{ K},$$

$$\text{Acceptance criterion: } R^2 < 98\%$$

$$\text{AND}$$

$$m - 0.05 < m' < m + 0.05 \text{ (orientation within } 2.8^\circ)$$

Test 5

The fifth and last test looks for guide points in a narrow vicinity of the line that corresponds to $C(t)$ and strongly smoothes the background image. The guide point threshold, $CRIT$ (Eq. 3.5), in this test is not fixed, but related to the maximum value of the signal in S , the enhanced BT image (Eq. 3.4). Let m_S be the maximum value in S ; the threshold chosen is the maximum between $0.77 \cdot m_S$ and 1K. The reason for establishing a variable threshold is to account for very weak contrails in scenes where the contrast with the background is small, so a scene-dependent threshold will point out the guide points in the image. Nevertheless, if the signal is too weak, no guide points will be found and the tracking will stop. Test 5 strongly smoothes the image while enabling the contrail to exist only in a narrow region, which can be too restrictive. That is why this test is used as end test and not from the beginning. It may also strongly limit the length of the contrail to its most relevant features. Experience has shown that in the last stages of the life cycle usually only Test 5 provides a positive answer.

$$w_1 = 2 \text{ pixels}, w_2 = 10 \text{ pixels}, CRIT > \max\{m_S \cdot 0.77, 1\} \text{ (K)},$$

$$\text{Acceptance criterion: } R^2 < 98\%$$

Figure 3.6, at the beginning of this section, shows an example of how ACTA works in the Test 3. In this case, tests 1 and 2 have failed because of surrounding cloudiness and a second contrail crossing the scene. First, the contrail $C(t)$ (Fig.3.6(1)) is used as input to define a region within which contrail $C(t' = t + \Delta t)$ could exist (Fig. 3.6,(2)), then, the image is filtered (Fig. 3.6(3)) to enhance contrail features and the tests are run to look for the guide points in the allowed region (Fig. 3.6(4)). Once the guide points are found (Fig. 3.6(5)), a linear fit is performed (Fig. 3.6(6)). Note that an alien pixel not belonging to the contrail is present as guide point. If the resulting line fulfils the orientation criterion, this line then is used as input line for the following timeslot and ACTA can proceed to Step II. Otherwise, ACTA performs Test 4.

Figure 3.10 shows an example of a contrail which was only detected in Test 5. It is due to the fact that the contrail is very wide and the contrast with the surroundings is not very strong. In consequence, tests 1, 3 and 4 do not detect enough guide points. In Test 2,

enough guide points are found but the linear fit does not fulfil the corresponding acceptance criterion (orientation). Only the last test provides a satisfactory output. Table 3.2 shows the output of each test in this scene.

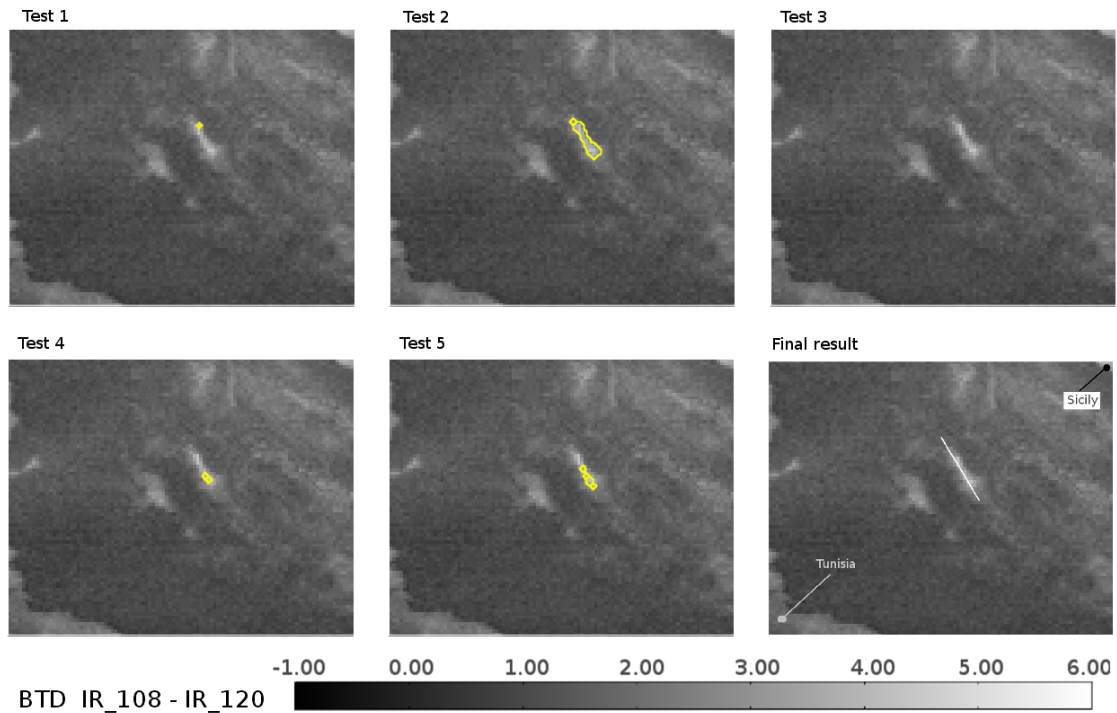


Figure 3.10: Test 1 - Test 5: Background, BTDR image (in K). Enclosed in yellow, guide points found in each Test. Bottom, right: Output of Step I, line (white) that corresponds to the contrail tracked by ACTA. Table 3.2 shows the process in detail. Location: Over the Mediterranean between Sicily and Tunisia. Date: 19/Jun/09 0945 UTC

Test	Number of guide points	Correlation coefficient	Slope m' $m(t) = -1.36$	Acceptance criterion	OK?
1	1	-	-	orientation	No
2	17	95.40%	-1.58	alignment	No
3	0	-	-	orientation	No
4	2	100%	-1	alignment and orientation	No
5	5	98.93%	-1.65	alignment	Yes

Table 3.2: Example of ACTA's Step I. Due to the characteristics of the contrail, only Test 5 provides a satisfactory output to continue the tracking

Step II

Once the position of the line is established, ACTA's next step is to retrieve the contrail shape by selecting the pixels that also belong to $C(t + \Delta t)$ from the surroundings of the line. This is achieved by combining three different masks² containing different information about the image and the position of the contrail. This Step combines the information of the line derived in Step I with the BTD image. Step II focuses on the neighbourhood of the line (Mask 1), identifies the edges of the contrail (Mask 2) through filtering, and outlines a possible shape by selecting the pixels with a higher BTD (Mask 3). A final clustering test retrieves the shape by selecting the pixels in groups. Figure 3.11 outlines the process followed by Step II. It is important to point out that Step II identifies also the parts of $C(t + \Delta t)$ that are not linear.

A complete definition of each mask in Step II and a step-by-step example (see Fig. 3.12) follow.

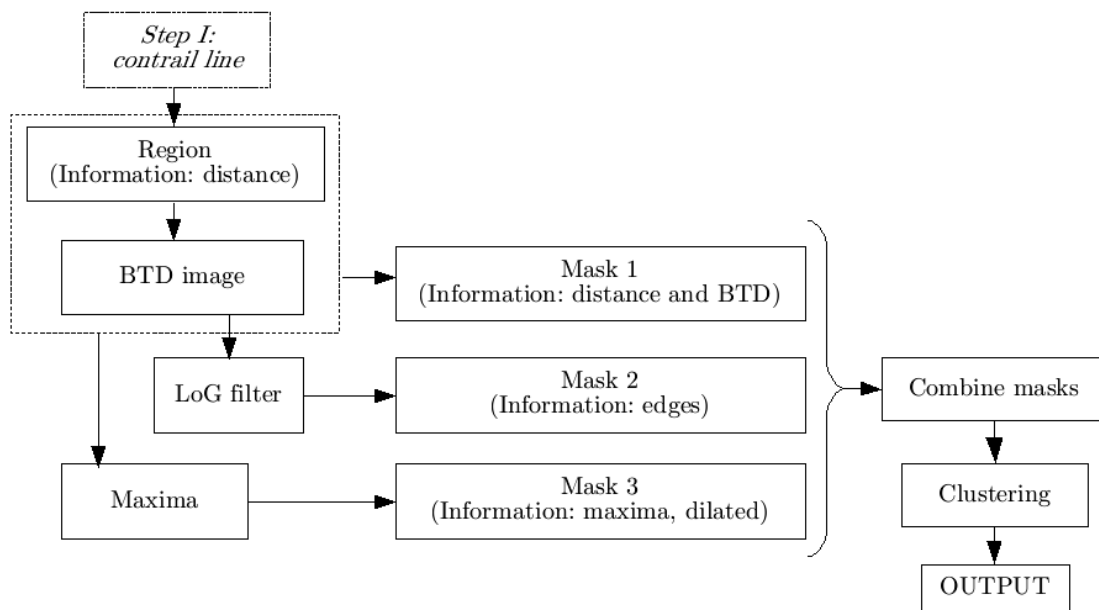


Figure 3.11: Schematic representation of Step II.

²Mask: template image used to accept or reject patterns in another image under study. Each pixel in a binary mask accepts (1) or rejects (0) a pixel in the studied image

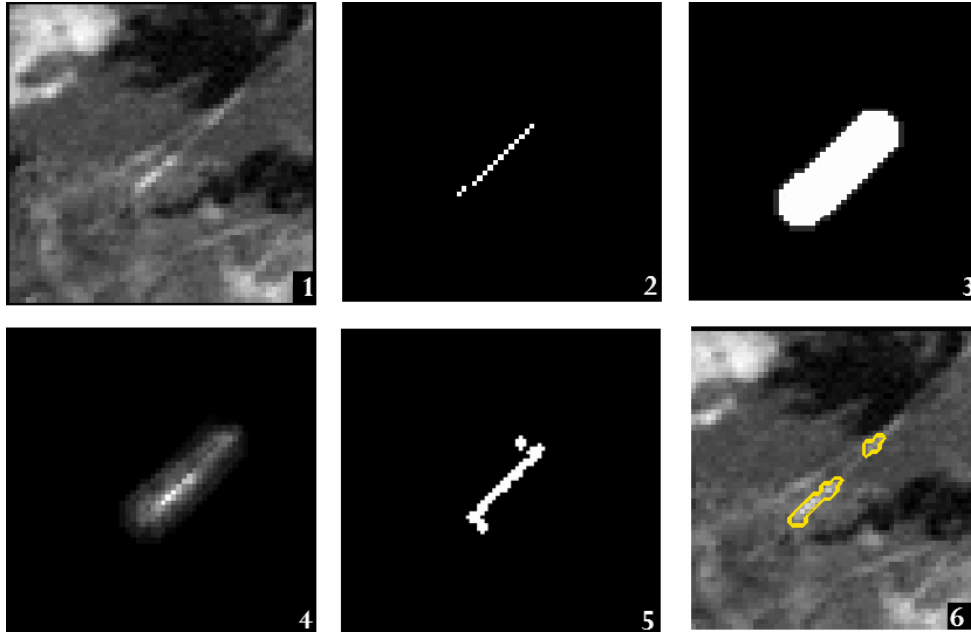


Figure 3.12: Process of selecting the contrail pixels. (1) Original BTM image. (2) Line from Step I. (3) Mask labeling the pixels around the line that lie within a given distance, D_{ij} . (4) Mask combining the distance information and the BTM signal, $BTD_{ij} \cdot D_{ij}$. (5) Mask containing information about the maxima of each line of the image, DIL_{ij} . (6) Pixels resulting after combining masks M_1 , M_2 and M_3 and performing the clustering test.

First mask: Distance and BTM³

A first mask is built considering a neighbourhood of 4 pixels around the line (see Fig. 3.12(3)). All pixels on the neighbourhood are likely to belong to the contrail, constituting a distance mask. The mask is thus 9 pixels wide, allowing the contrail to exist not only along the line, but within a radius of 16 - 20 km (latitude and longitude dependent) around the line. This enables the contrail to expand, to split and to lose linearity. The neighbourhood is implemented as a matrix, D_{ij} , as follows:

$$D_{ij} = \sum_{d=0}^4 L(i \pm d, j \pm d) \quad (3.6)$$

where $L(i, j)$ is as defined in Step I, Equation 3.1.

This distance mask is multiplied by the brightness temperature difference image. The result can be seen in Fig. 3.12(4). The resulting mask, M_1 contains information from both the distance to the original line and the BTM. This allows the contrail to have nearly any shape within the boundaries of the neighbourhood. Only pixels having a positive signal in M_1 can belong to the contrail.

$$M_1 = \begin{cases} 1 & , \text{ if } BTD_{ij} \cdot D_{ij} > 0 \\ 0 & , \text{ otherwise} \end{cases} \quad (3.7)$$

³Masks M_1 , M_2 , M_3 and M_{final} are matrices of $N_i \times N_j$ elements. Multiplication (\cdot) involving these masks implies Hadamard (or Schur) product (elementwise multiplication of their elements)

Second mask: Edge detection

An edge detection algorithm is applied to the brightness temperature image to identify the boundaries of the contrail. By definition, the pixels identified as boundary by the edge detection algorithm have a zero likelihood of being contrail pixels. This second mask is also binary and assigns 0 to the edge pixels and 1 to the pixels not belonging to edges.

The edge detection algorithm is based on the *Laplacian of Gaussian* (LoG) filter described in Canty (2007). The computation of the gradient of a grey-scale image provides a maximum at an edge. The second derivative is zero at that maximum and has opposite signs immediately on either side. Thus, it is possible to determine edge positions to the accuracy of one pixel by using second derivative filters.

Laplacian filters have the property of returning 0 in regions of constant intensity and in regions of constantly varying intensity but nonzero at their onset or end. They are also very sensitive to image noise, so first a Gaussian filter must be applied to smooth the image. Since the convolution operation (*) is associative, the application of both filters consecutively on the image is equivalent to calculating the Laplacian of the Gauss function and then using the resulting function as filter.

The Gauss function, G , in two dimensions is given by:

$$G = \frac{1}{2\pi\sigma^2} \exp\left(-\frac{1}{2\sigma^2}(x_1^2 + x_2^2)\right), \quad (3.8)$$

where the parameter σ determines its width. Applying the Laplacian operator, the final filter is thus:

$$\nabla^2 G = \frac{1}{2\pi\sigma^6}(x_1^2 + x_2^2 - 2\sigma^2) \exp\left(-\frac{1}{2\sigma^2}(x_1^2 + x_2^2)\right). \quad (3.9)$$

Let BTD_{ij}^f be the result of the convolution of the Laplacian of Gaussian filter, $LoG_{ij} = \nabla^2 G(x_1, x_2)$, with the BTD image:

$$BTD_{ij}^f = BTD_{ij} * LoG_{ij} \quad (3.10)$$

As the signs are opposite on either side of the edge, the zero crossings in the horizontal and vertical directions are determined from the products of the image with a copy of itself shifted by one pixel to the right and upward, respectively. Let $BTD_{ij}^{f,up}$ and $BTD_{ij}^{f,right}$ be the filtered BTD images shifted upwards and rightwards, respectively. Sign changes correspond to negative values in the products and these define the edges, E_{ij} .

$$\begin{aligned} F1_{ij} &= BTD_{ij}^f \cdot BTD_{ij}^{f,up} \\ F2_{ij} &= BTD_{ij}^f \cdot BTD_{ij}^{f,right} \end{aligned}$$

$$E_{ij} = \begin{cases} 1 & , \text{ where } F1_{ij} < 0 \quad \vee \quad F2_{ij} < 0 \\ 0 & , \text{ otherwise} \end{cases} \quad (3.11)$$

Finally,

$$M_2 = \begin{cases} 0 & , \forall(i, j) \mid E_{ij} = 1 \\ 1 & , \text{otherwise} \end{cases} \quad (3.12)$$

Figure 3.13 shows the filter applied in this work (size: 16×16 pixels and $\sigma = 2$) and an example of the identified edges.

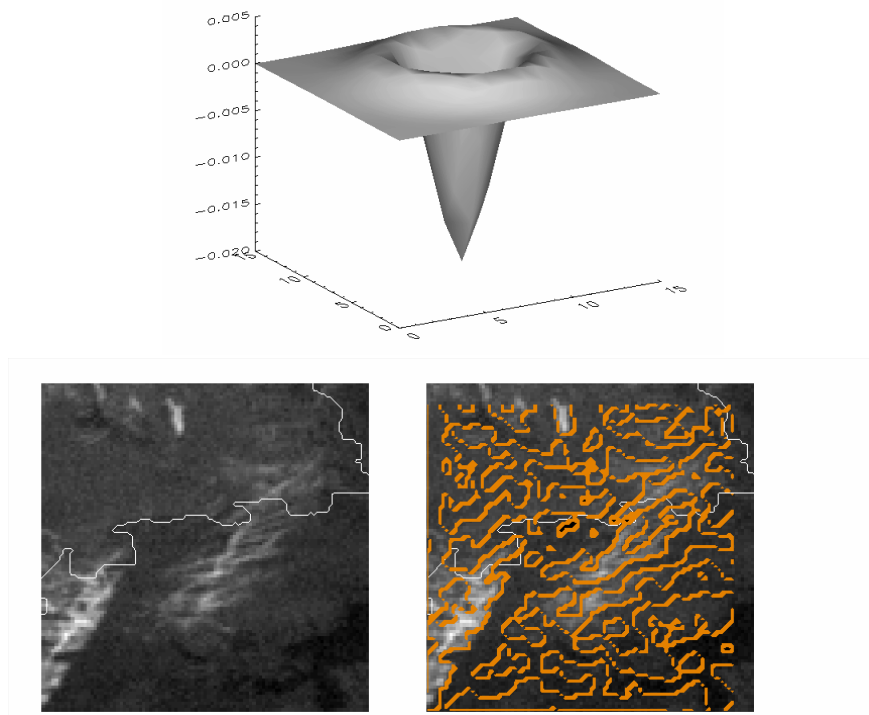


Figure 3.13: Top: Laplacian of Gaussian filter applied, on a 16×16 grid, with $\sigma = 2$. Bottom: Left: BTM image corresponding to 17/6/09 0700 UTC covering part of the North Sea, northern Germany and western Denmark. Right: in orange, edges identified when applying LoG filter to the BTM image.

Third mask: Maxima

The contrail corresponds to the pixels in the BTM image with a larger brightness temperature difference. This mask intends to identify the pixels that have a stronger BTM signal and their surroundings, that is, this mask retrieves a possible shape of the contrail. To locate the pixels that present a larger BTM, first the pixel with the strongest BTM signal in each horizontal line within the neighbourhood area (see Eq. 3.7) is selected:

$$MAX_{ij} = \begin{cases} 1 & \text{if } BTM_{ij} = \max_{i_0 \leq k \leq i_N} (M_1(k, j)) \\ 0 & , \text{otherwise} \end{cases} \quad (3.13)$$

A broader region around the maxima is created expanding the pixels found up, down, left and right, as in the example below (Fig. 3.14, left).

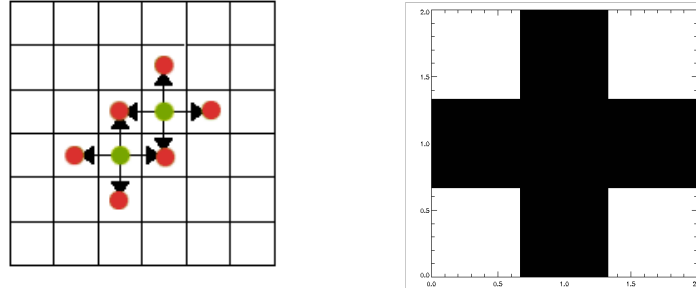


Figure 3.14: Left: Example of creation of a broader region. Green: original pixels. Green and red: expanded (dilated) region. Right: 3x3 structuring element used in the dilation. Black = 1, White = 0.

Technically, this is carried out applying the morphological operator dilate⁴ (Stark et al., 1998) to these pixels using the cross-shaped 3x3 pixel structuring element, $STRUCT_{ij}$, shown in Fig. 3.14, right

$$DIL_{ij} = MAX_{ij} \oplus STRUCT_{ij} \quad (3.14)$$

An example of the resulting image, DIL_{ij} , can be seen in Fig. 3.12(5). Next, the temperature difference of the pixels in DIL_{ij} is calculated and compared with the average of the brightness temperature difference in the original area, D_{ij} (Fig. 3.12(3), Eq. 3.6). Due to the fact that allowed region in D_{ij} is very wide, most of the pixels in it (water clouds or surface) have a low BTD signal whereas only a few (either only the contrail or the contrail and cirrus clouds nearby) will have a strong BTD signal. Let the average BTD in D_{ij} be \overline{BTD} . The pixels having a lower temperature difference than \overline{BTD} , i.e. a weaker BTD signal, are assigned a zero likelihood of being contrail pixels. This way, the mask can discard the pixels with a lower-than-average BTD, a scene-dependent criterion that points out the contrail pixels on the image. The result constitutes the third mask (see Eq. 3.15).

$$M_3 = \begin{cases} 1 & , \forall(i, j) \in DIL_{ij} \quad | \quad DIL_{ij} \cdot BTD_{ij} > \overline{BTD} \\ 0 & , \text{otherwise} \end{cases} \quad (3.15)$$

⁴Dilation (\oplus), is the transformation of an image by a structuring element, that results in the expansion of the shapes contained in the input image. In this work, the `dilate` operator in IDL has been used as follows: `resulting_image=dilate(input_image,structuring_element)`

Combination of masks

By combining the three masks with a logical AND: the mask containing information both from the proximity to the line and from the temperature difference, the mask derived from the edge detection algorithm, and the mask resulting from applying the dilate operator to a selection of the stronger signal pixels and refining the result, a final binary mask can be obtained. Pixels where $M_{final} = 1$ are labeled as possible contrail pixels:

$$M_{final} = M_1 \cdot M_2 \cdot M_3 \quad (3.16)$$

Clustering

The labeled pixels undergo a final clustering test to identify the grouped regions and discard isolated ice cloud pixels that have been misidentified in M_{final} . A contrail is typically a connected region sometimes split into smaller areas. Only the pixels belonging to connected regions of more than 3 contiguous pixels are considered contrail pixels.

In this work, the IDL command `label_region` has been used. Let $CL_{ij} = cluster(M_{final})$ the result of applying `label_region` to the two-dimensional array M_{final} . CL_{ij} , is an array of the same dimensions as M_{final} where each cluster carries a consecutive numeric label. Therefore, pixels in *Cluster 1* have $CL = 1$, pixels in *Cluster 2*, $CL = 2$, etc. Let $m_{CL} = max(CL_{ij})$ be the number of clusters or connected regions in M_{final} . The number of pixels, n_p , in each cluster, p , is:

$$n_p = i, j \in M_{final} \quad | \quad CL_{ij} = p \quad (3.17)$$

Thus, the contrail pixels *con_px* can be defined by:

$$con_px = i, j \in CL_{ij} \quad | \quad n_p > 3 \quad , \quad 0 < i < m_{CL} \quad (3.18)$$

The pixels selected as contrail pixels by ACTA are shown on Fig. 3.12 (bottom, right): all pixels enclosed by the yellow line are contrail pixels. This example also shows that the presence of a secondary contrail very close to the tracked contrail does not affect the final result. The westernmost and easternmost pixels ± 10 pixels are used as limits i_0 and i_1 for the length of the contrail in Step I.

When the Step II of ACTA is over and the whole set of pixels that corresponds to contrail $C(t + \Delta t)$ is identified, ACTA writes the position of the contrail pixels to a file and proceeds to Step I using the line parameters of $C(t + \Delta t)$ as input for the following time slot.

3.1.3 Discussion

ACTA is a tracking algorithm that identifies contrails and contrail-cirrus throughout their lifetime taking advantage of the high temporal resolution of the SEVIRI sensor (5 minutes). The most important feature of ACTA is that the only information necessary to start the tracking of the contrail / contrail-cirrus is a single positive identification by the contrail detection algorithm (CDA) on MODIS at any stage of its development. Data input from a human observer or any other instrument with a high spatial resolution such as AVHRR or AATSR could also be used to provide an input for ACTA.

ACTA's results have been manually verified in a large number of cases. It has been confirmed that the performance of the algorithm is excellent with rapid-scan data, where the temporal delay between successive images is five minutes. Larger time steps such as the regular 15 minute scan can be used for isolated contrails, but in a scene with many parallel linear contrails, ACTA might misidentify the contrail. In these cases it may select a neighbouring contrail to continue the tracking.

According to the design of ACTA it is not necessary to use actual wind field data. Use of ECMWF wind field data has not improved the accuracy of the tracking but resulted in much longer processing times. Considering an average fixed wind speed of 110 km/h (~ 60 knots) at 10 km height and using it to define the region within which the contrail can move each 5 minutes is sufficient for the tracking and has reduced significantly the computing time. ACTA is very fast, each iteration requiring less than one minute on a usual desktop machine depending on the number of tests that must be performed in Step I.

ACTA uses only two SEVIRI channels, IR_108 and IR_120. Additional channels or channel combinations have been considered, such as the IR_039 ($3.9 \mu\text{m}$) for discriminating between water and ice clouds or water vapour channels WV_062 ($6.2 \mu\text{m}$) and WV_073 ($7.3 \mu\text{m}$), and also BTDs involving IR_087 ($8.7 \mu\text{m}$), but these considerations have not added significant improvements to the result while notably increasing the computation time. In some images such as that depicted in Fig. 3.12 (bottom, right) ACTA misses parts of the contrail that have a lower BTD response. Furthermore, there are parts in the life cycle of the contrail that cannot be detected by a passive satellite instrument (such as in its early stages or when its optical thickness and the contrast to the surroundings are very low). These are ACTA's known limitations. ACTA provides considerably more information than the CDA algorithm but may still miss part of the evolution of contrails and contrail-cirrus.

If the input does not provide the full length of a contrail, some contrail pixels are initially ignored. To prevent this, ACTA has loose boundary conditions that allow the tracked cloud to be longer or shorter than suggested by the input data, correcting the length of the contrail / contrail-cirrus in subsequent intervals. Nevertheless, an input contrail that is too short can result in a too short tracked contrail. This problem can be solved using a *human* input, i.e. if the researcher feeds ACTA with input line parameters detected manually. Thus, throughout the lifetime of the contrail its full length can be accurately tracked. The objective of this work was to perform a statistical analysis over a very large number of contrails, so human input was not considered to be a feasible option. For each time step an average value of all pixels is used for further analysis, so ignoring a few contrail pixels in certain scenes due to the automatic input does not imply a substantial change in the average when

computing lifetime, optical thickness or radiative forcing. The combination of ACTA and CDA provides such a large number of occurrences that the occasional omission of pixels can be considered negligible. Besides, this work aims to establish a minimum value for the effect of anthropogenic aviation clouds on the climate system. Of extreme importance is that all pixels labeled as contrail pixels actually belong to contrails. This point has been fulfilled satisfactorily by ACTA.

The CDA has a low but non-zero false alarm rate. The detected contrails are mapped by ACTA on the MSG grid and tracked. The different performance and spatial resolution of the instruments and algorithms involved can lead to two different types of errors. In the first place, features misdetected by the CDA have to be eliminated. Second, since CDA and ACTA data work on different spatial resolutions, it is possible that the CDA detect a very narrow contrail on the MODIS scene (resolution 1km) that cannot be detected by the SEVIRI sensor (pixel size at least 3x3km, see Fig. 2.9). To avoid this, data have gone through an exhaustive visual control and misdetections have been discarded. This analysis has also helped to increase the quality of the results by eliminating not only false CDA detections but also by sorting out the cases where the tracking *jumps* from the contrail being tracked to a different contrail nearby. The latter only occurs when contrails are drifted by a very strong lateral wind and constitute less than 1% of the cases.

A step-by-step example of the tracking can be found in appendix A. The yellow line encloses the pixels identified as contrail. Note that the vicinity of other contrails parallel to the tracked one does not affect the tracking and that crossing over a pre-existing contrail does not lead to a misidentification of the original contrail. It can be seen that ACTA still tracks the contrail when it has lost the linear structure in the late stages of its life cycle. The moment where the contrail is detected by the CDA, coincident with MODIS overpasses, occurs at 1135 UTC. ACTA uses this input to track the contrail back until 1100 UTC and forth until 1725 UTC. Figure 3.15 shows the first, the input and the last stages of the example shown in Appendix A.

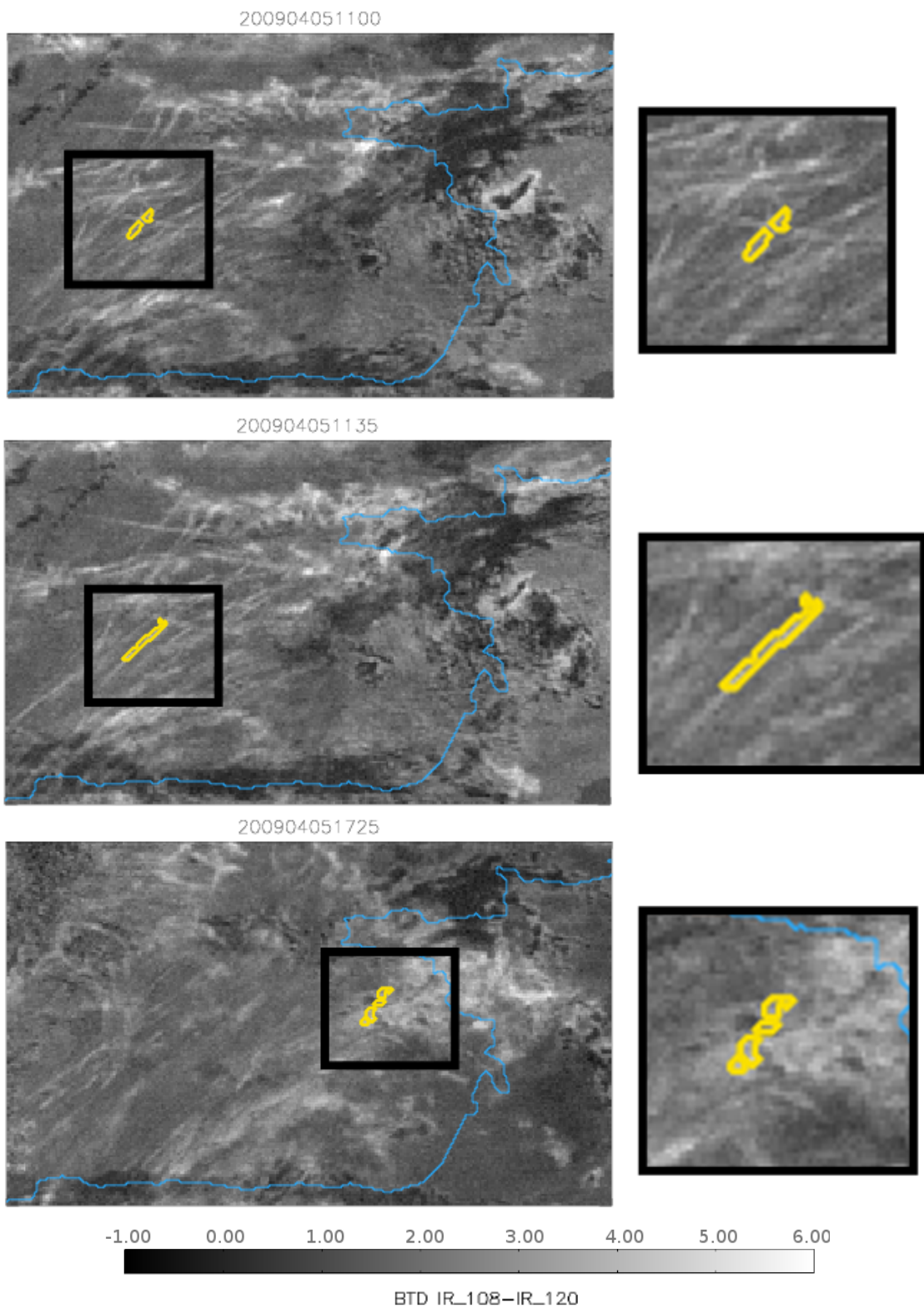


Figure 3.15: Example of ACTA tracking a contrail over the bay of Biscay. Top: younger stage, 1100 UTC. Centre: 1135 UTC, coincident with the CDA input. Bottom: older stage, 1725 UTC. Right column: zoom-in of the studied area. Background: BTDR in K.

3.2 Outgoing longwave radiation

In order to develop an algorithm that computes the irradiance from radiances measured by the SEVIRI sensor, a narrowband to broadband conversion is necessary. The conversion depends on the wavelength, the geometry of the observed system, the satellite zenith angle and the azimuth. The angular dependency (strongly dependent on the cloud phase) and the ground properties must also be taken into account. The algorithm used in this work to perform the narrowband to broadband conversion has been developed by B. Mayer. With the `libRadtran` package, 10,000 different combinations of atmospheric profiles (temperature, pressure, water vapour, etc.), cloud phase and surface types for 800 different sun-satellite geometries have been simulated (Krebs et al., 2007). `libRadtran` is a radiative transfer package developed by Mayer and Kylling (2005) devoted to the calculation of solar and thermal radiation in the Earth's atmosphere. This package slices the atmosphere in a number of layers and computes absorption, scattering and emission in each and every one of them. The different applications of the package range from instrument simulation to irradiance and ERB computations. These simulations have been then used to develop the longwave (LW) and the shortwave (SW) irradiance retrieval algorithms described hereafter.

According to the Stefan-Boltzmann law (Eq. 2.13), each body emits a certain amount of radiation given its temperature. The top of atmosphere (TOA) irradiance in the longwave range is computed using a multilinear fit to the simulated SEVIRI brightness temperatures based on the Stefan-Boltzmann law:

$$F_{LW}^{\uparrow}(\theta_{sat}) = \sigma \{ a(\theta_{sat})T_{6.2} + b(\theta_{sat})T_{7.3} + c(\theta_{sat})T_{8.7} + d(\theta_{sat})T_{9.7} + e(\theta_{sat})T_{10.8} + f(\theta_{sat})T_{12.0} + g(\theta_{sat})T_{13.4} + h(\theta_{sat}) \}^4 \quad (3.19)$$

Where:

$\sigma = 5.6703 \cdot 10^{-8} W m^{-2} K^{-4}$ is the Stefan-Boltzmann constant,

θ_{sat} is the satellite zenith angle and

$a(\theta_{sat}) \dots h(\theta_{sat})$ are the fit coefficients, which are dependent on the satellite viewing angle.

The fit coefficients have been assessed through this multilinear parameterisation and have been summarised in a table for different satellite zenith angles. Different coefficients are used for cirrus-free and cirrus-covered scenes. The dependency on the satellite zenith angle of each coefficient can be seen in Figure 3.16 for the cirrus-free case and in Figure 3.17 for the cirrus-covered case. The MeCiDA (Meteosat Cirrus Detection Algorithm) mask developed by Krebs et al. (2007) is used for the discrimination. It can be seen that the coefficients behave differently depending on the satellite zenith angle. It must be noted that the coefficients are issued from the multilinear fit, which is very robust, but their physical interpretation remains unclear. Therefore, it is very important to carry out the validation of the irradiances derived thanks to this method.

In order to compute the outgoing longwave radiation it is necessary to proceed in three steps: first, transform the SEVIRI radiances to brightness temperatures; second, run the MeCiDA algorithm on the data to label the pixels as cirrus-free or cirrus-covered; and third, apply

Equation 3.19 taking into account the satellite zenith angle to use the correct fit constant for each pixel. An example of the computation of the LW irradiance following this method is shown in Figure 3.18, left.

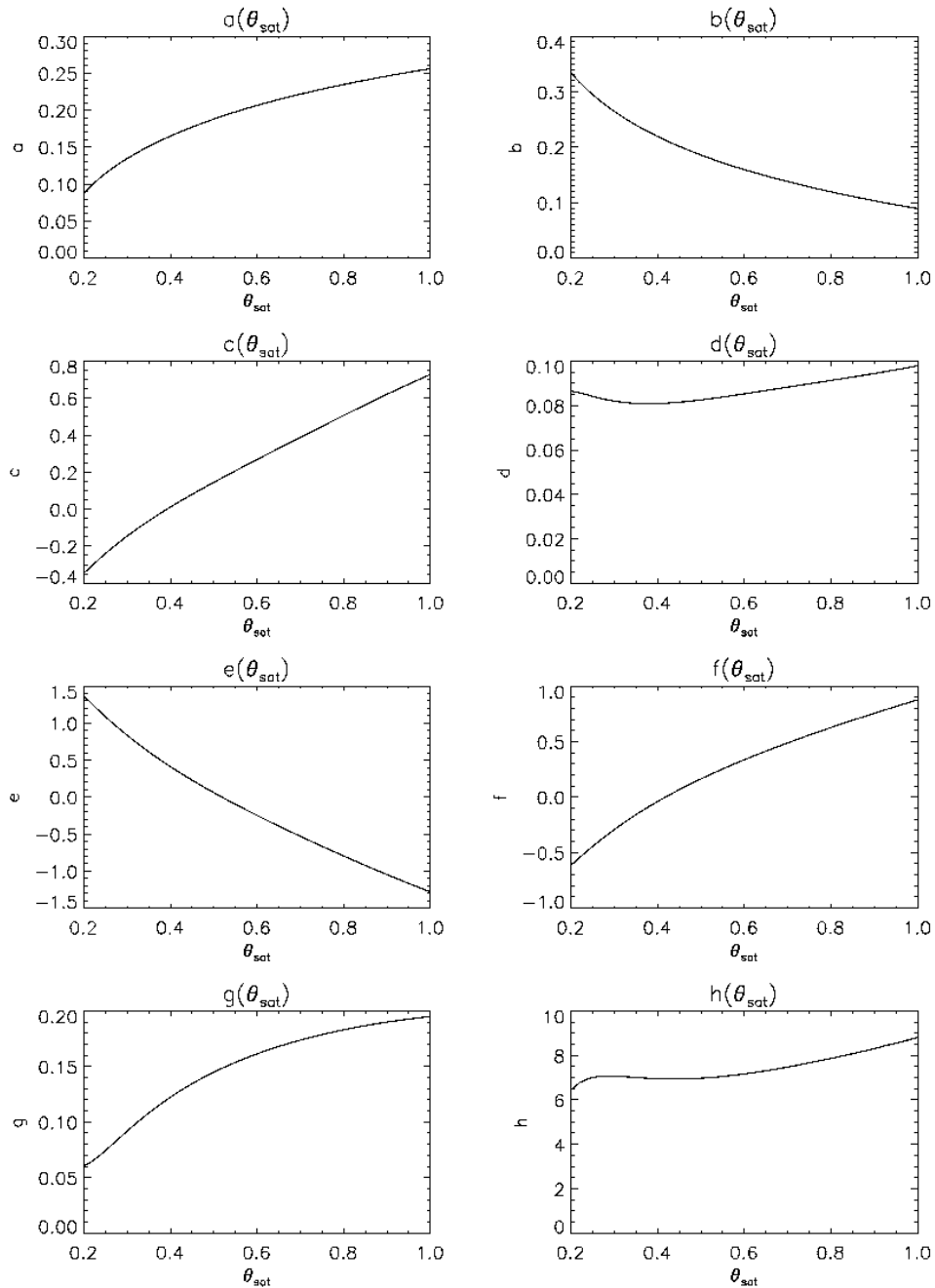


Figure 3.16: Fit coefficients of Equation 3.19 vs. satellite zenith angle for cirrus-free scenes.

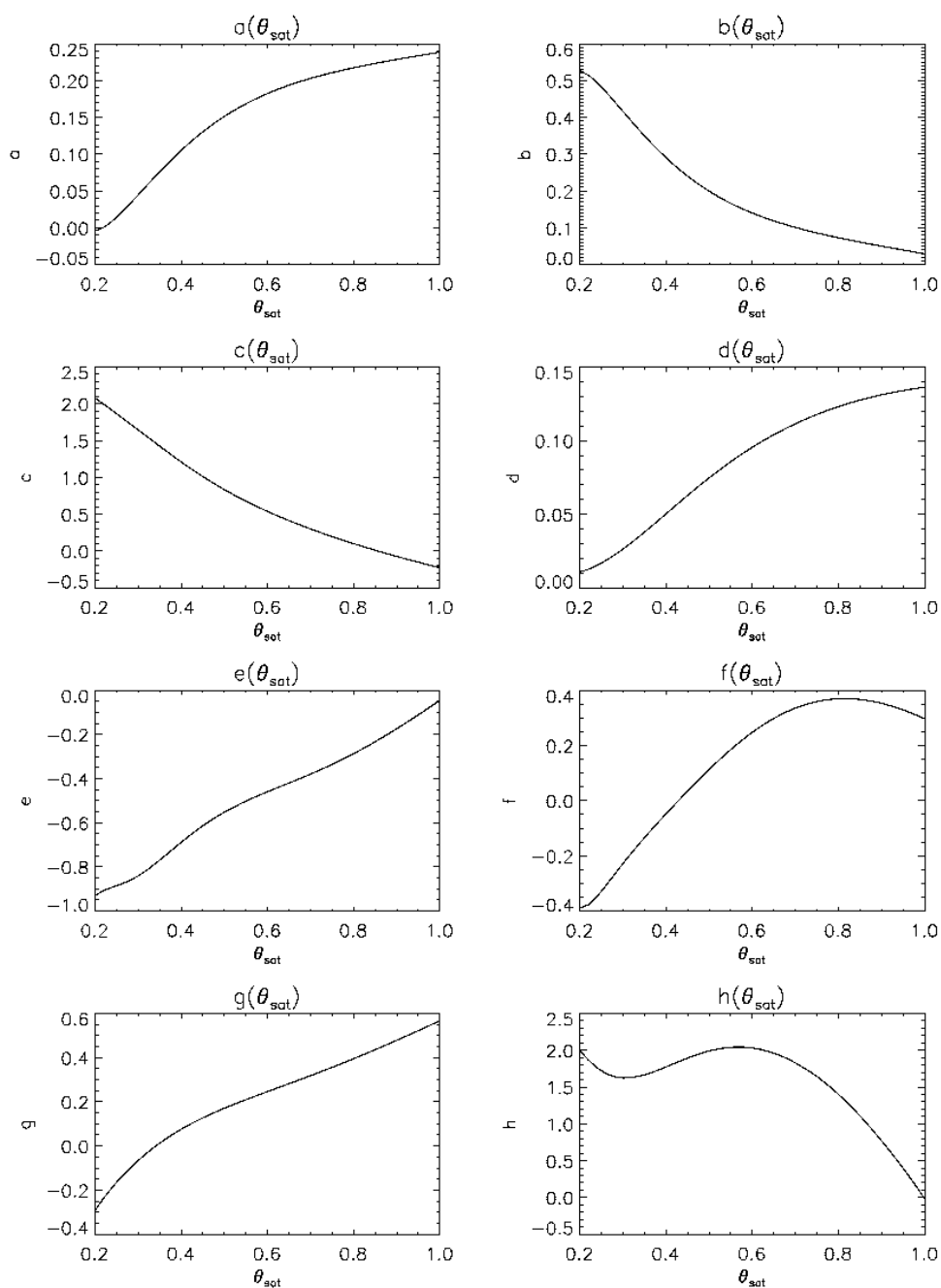


Figure 3.17: Fit coefficients of Equation 3.19 vs. satellite zenith angle for cirrus-covered scenes.

3.3 Reflected shortwave radiation

To compute the narrowband-to-broadband conversion in the SW range, an artificial neural network developed by H. Mannstein has been used. Given that the relationship between irradiance and radiance is not linear, a multilinear parameterisation as the one described in the previous section is not suitable for this case. Therefore an artificial neural network has been used to compute the irradiances.

An *artificial neural network* (ANN), sometimes called only *neural network* (NN), is an adaptive system that changes its structure based on the information that flows through the network during the learning phase. This flow allows the network to set a number of internal parameters, the *weights*, that alter the connections in the network nodes to produce the right output. The adjusting of the weights is a fully automatic process, without human intervention. Such systems are widely used in biology, informatics, physics and microelectronics. The problem that the neural network must solve is taken from real examples: the network is fed with a series of input values and their corresponding outputs, so the network *learns* from these examples and optimises the weights accordingly. After this training process, all internal parameters are fixed and the network has acquired the ability to compute results for a similar problem given any new input dataset. The performance of the neural network is highly dependent on the quality of the training dataset. If training data do not cover a significant portion of the conditions to be studied or if the noise is high, then the neural network will not provide the right solution. The training set of the network used for this work contained the `libRadtran` simulations of the state of the atmosphere mentioned in Section 3.2 and was carried out with a back-propagation algorithm (Rumelhart et al., 1986). This is one of the most usual training methods and minimises the output error.

The neural network has been trained and verified with the radiances simulated in the SEVIRI visible channels: VIS006, VIS008 and near-infrared channel IR_016 for different geometries of the sun-satellite-earth system. It has 200 neurons and one layer. The neural network needs an input vector containing the following information:

- Radiance VIS006
- Radiance VIS008
- Radiance IR_016
- Satellite zenith angle
- Solar zenith angle
- Relative azimuth
- Land/sea mask

The output contains the reflected shortwave irradiance on TOA. The narrowband to broadband conversion is applied to each pixel of a SEVIRI image. Fig. 3.18, right, shows the SW irradiance computed from SEVIRI radiances with the neural network.

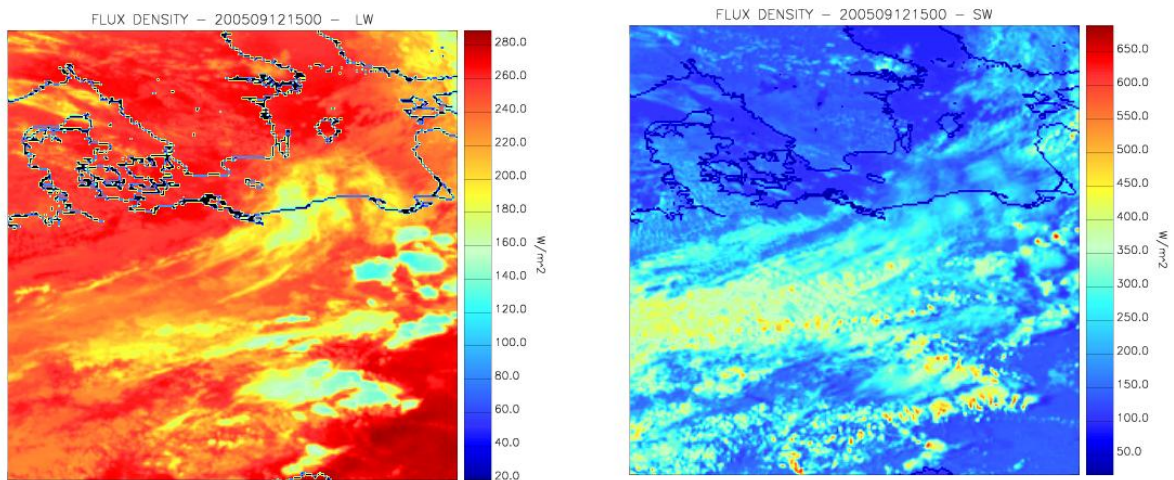


Figure 3.18: Left: Outgoing LW irradiance at TOA computed by the multilinear parameterisation. Right: Reflected SW irradiance at TOA computed by the neural network. Area: Germany, Denmark, Poland, south of Sweden, southern part of the Baltic Sea. Date: 12/Sep/05 1500 UTC.

Comparing both images in Fig. 3.18, some interesting results can be seen. Both images correspond to the same scene. The areas with high reflected SW irradiance (Fig. 3.18, right) are bright structures (clouds). The LW irradiance (Fig. 3.18, left) emitted by clouds is low if the cloud is very cold (and thus its cloud top is located very high) and grows larger the warmer (lower) the cloud lies. Over Jutland low clouds can be seen, they can be distinguished from the surrounding water in the SW image, because the albedo is different, but are hardly seen in the LW image, because their thermal emission is essentially that of the background. On the right-hand side of the image, over Poland, high clouds can be seen, likely of a convective origin. These present low LW emission (very cold) and high signal in the SW image (very bright). Across the south of Norway and the north of Denmark, a region colder than the background can be identified (see LW image). The same area in the SW image shows a low reflected irradiance. The structure is a cirrus-like cloud: cold but optically thin.

3.4 Validation

Shortwave and longwave irradiances from CERES and GERB are used for the validation of the SEVIRI-based algorithms. CERES data have a highly different satellite projection than SEVIRI and GERB, both on board of MSG. Also spatial resolutions of all three sensors strongly differ (cf. Table 2.5 at the end of Chapter 2). To avoid the errors made in a direct comparison of the images and to perform the validation with the least loss of information possible, a *modified nearest neighbour* mapping technique has been developed.

3.4.1 Mapping - Modified Nearest Neighbour Method

Fig. 3.19 A and B shows the schematic representation of two different resolution images with two different projections. Fig. 3.19 A represents satellite data with a higher spatial resolution than data in B. Fig. 3.19 C shows which pixels of the A image are closer to each pixel in the B image. Once each pixel in the low spatial resolution image B has been assigned its corresponding set of high resolution pixels in A, there are two possibilities to compare the images A and B: in a low spatial resolution grid or in a high spatial resolution grid, and both lead to the same results.

To compare data in a low spatial resolution grid, in each B pixel location an average of the corresponding A pixel values is placed. This corresponds to the comparison between schematic representations 3.19 B and 3.20. However, due to the nature of the data used in this work, the comparison has been chosen to be made in the SEVIRI grid, that is, in the highest spatial resolution and in the satellite projection. The averaged high resolution data are placed back on their original positions, and the non averaged low resolution data are placed in their corresponding high resolution positions, as shown in Fig. 3.21. Therefore, both images have the same type and amount of information, the resolutions are similar and the projection is the same. Moreover, the errors that would have arisen from comparing originally A and B in Fig. 3.19 are avoided.

The usual nearest neighbour method links each pixel in image B to just one pixel in image A: that located closest. This system can lead to errors because the information contained in one pixel is the combination of all the possible structures within, and the modified nearest neighbour method takes this into account. If the closest pixel is a cloudy pixel but the rest of the associated pixels are cloud free, the value assigned to the pixel A by the modified method corresponds to a combination of the cloudy and cloud-free pixels instead of assigning it the value of a fully cloudy pixel. The average performed by the modified nearest neighbour method is more representative than individually selected pixels, especially when the spatial resolutions to compare are highly different, which is the case in this work.

Examples of the application of the modified nearest neighbour method to the different platforms used in this work are shown next.

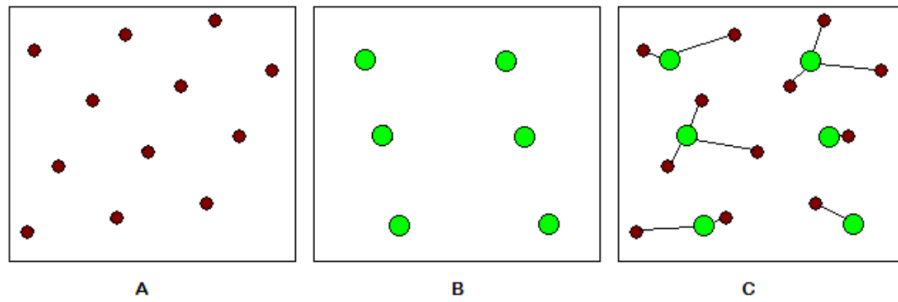


Figure 3.19: A) Higher spatial resolution image -dark red-, B) Lower spatial resolution image -green-, C) Lower resolution pixels connected to their corresponding higher resolution pixels according to the modified nearest neighbour method.

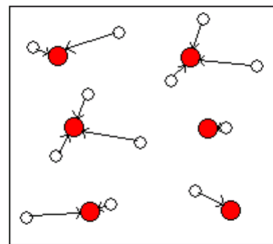


Figure 3.20: Higher resolution pixels averaged and placed in their corresponding lower resolution locations -red-.

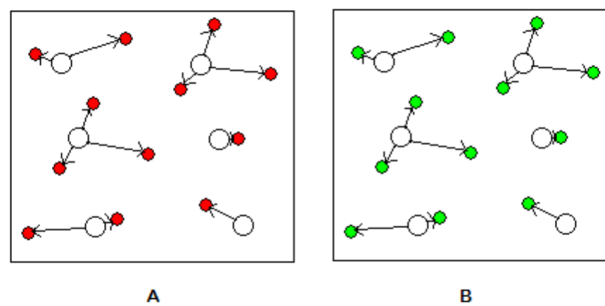


Figure 3.21: A) Averaged higher resolution pixels -red- placed back to their original locations, B) Lower resolution pixels -green- placed in their corresponding higher resolution locations.

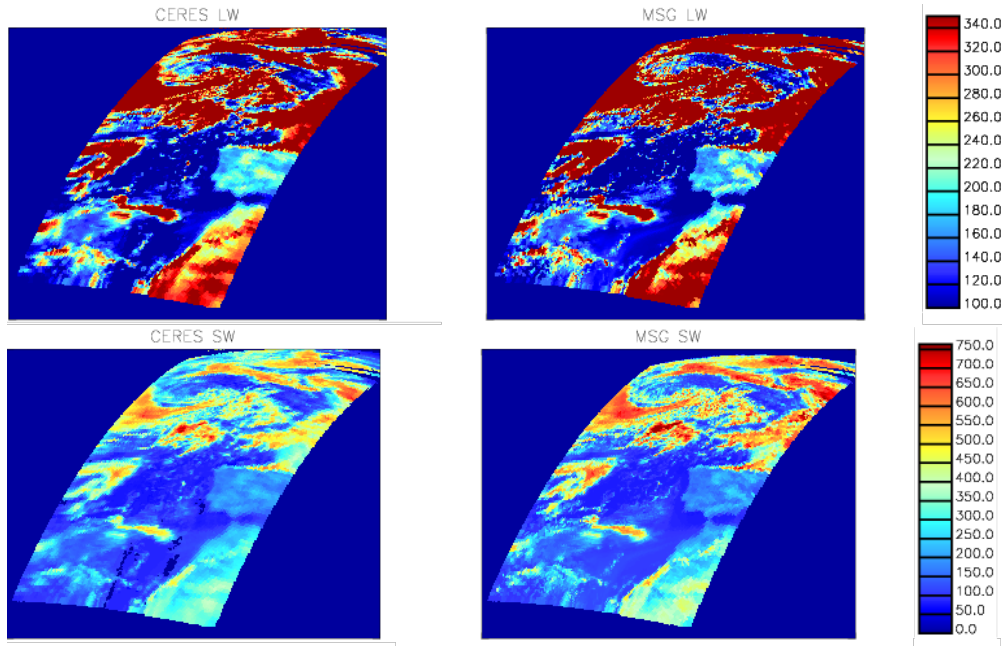


Figure 3.22: Left: Terra/CERES irradiance (W/m^2) in LW (top) and SW (bottom) on MSG/SEVIRI grid. Right: Corresponding MSG/SEVIRI irradiance in LW (top) and SW (bottom) in W/m^2 .

Mapping of Terra/CERES data in the MSG/SEVIRI grid

The irradiance measured by CERES has been projected on the SEVIRI grid in the SW and LW ranges as shown in Fig. 3.22, top. Then, SEVIRI irradiances have been computed and the corresponding CERES footprint pixels selected and averaged, according to the method explained. An example can be seen in Fig. 3.22, bottom. Even though the irradiances are not exactly identical, the same patterns and structures can be recognised.

The number of pixels of the SEVIRI grid allocated to one pixel of the projected CERES grid is shown in Fig. 3.23, left. It can be seen that irregularities arise on the side strips of the footprint. This is due to the fact that the modified nearest neighbour technique allocates all remaining SEVIRI pixels in the neighbourhood to an edge CERES pixel. Therefore, the pixels in the side stripes of the CERES swaths have not been used in the study. For the CERES sensor is in a cross-scan mode, the pixels are larger near the edges of the swath. This explains the higher number of SEVIRI pixels allocated to each CERES pixel in Fig. 3.23 at lower latitudes, where SEVIRI grid pixels are also small.

The distance between the CERES pixel and the corresponding SEVIRI-grid pixel is very small, usually around 0.02° and it never exceeds a tenth of a degree (cf. Fig. 3.23, right). This guarantees the quality of this method. The structure of this image shows the typical Moiré effect pattern due to the overlap of two grids with different resolutions.

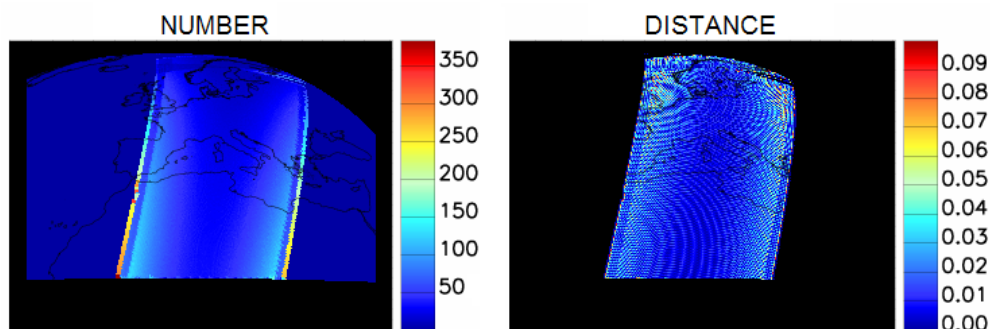


Figure 3.23: Left: Number of SEVIRI grid pixels allocated to each CERES grid pixel. Right: Distance in arc degrees between each CERES grid pixel and its corresponding SEVIRI-grid pixel.

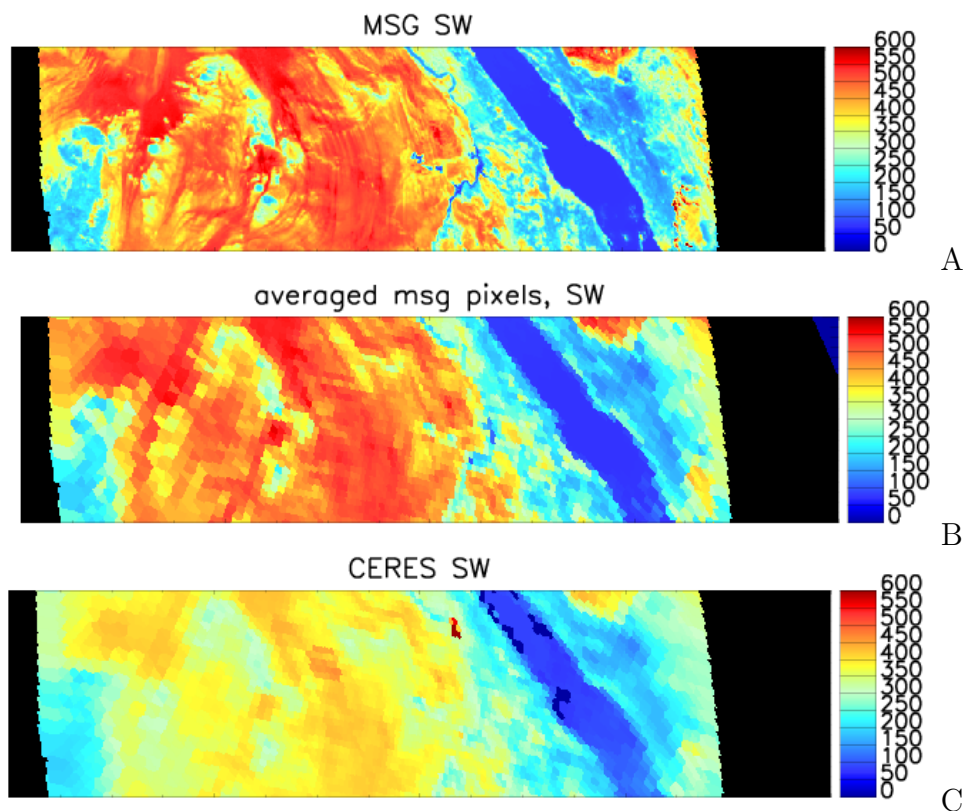


Figure 3.24: Outgoing shortwave irradiance (W/m^2) for the region around the Red Sea. A: MSG/SEVIRI original resolution, B: MSG/SEVIRI averaged pixels, C: Terra/CERES on satellite projection.

A closer example of the mapping and averaging undergone by SEVIRI pixels to be prepared for the comparison with CERES is shown in Fig. 3.24. Fig 3.24 A shows the shortwave outgoing irradiance of the pixels in the region covered by the CERES overpass in the original resolution. Fig. 3.24 B shows the average of the original pixel values so that they match the spatial resolution of Fig. 3.24 C. Data in Fig. 3.24 B and C will be used for the validation of the SEVIRI-based irradiance retrieval methods with the CERES irradiance.

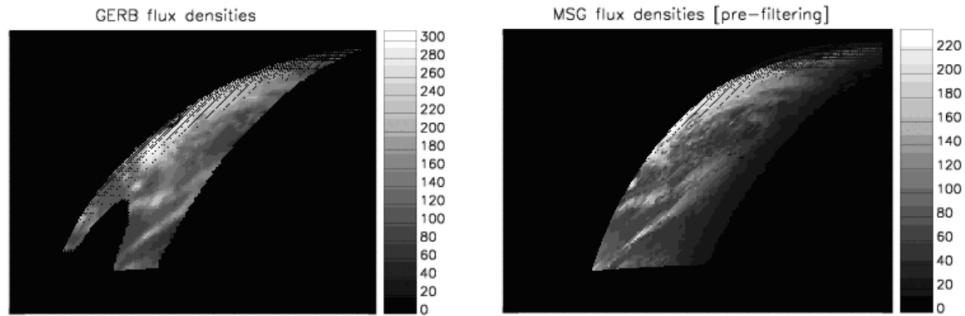


Figure 3.25: Left: Irradiance from GERB (SW). Right: Irradiance from SEVIRI (SW).

Mapping of MSG/GERB data in the MSG/SEVIRI grid

GERB and SEVIRI data share the same view of the Earth, as both sensors are on board of the geostationary satellite MSG. Thus, a reprojection of the data is not needed. Nevertheless, in order to overcome the different spatial resolutions an averaging of the SEVIRI pixels is needed. This is, again, carried out with the modified nearest neighbour method.

However, after averaging the data and mapping them in their corresponding pixel locations, still a difference is to be observed. In Fig. 3.25 it can be seen how the GERB image shows less detail than the SEVIRI image. The cut in the lower section of GERB is to avoid sunglint⁵, which can lead to errors in the derived irradiance. The GERB data used in this work correspond to the Averaged Rectified Geolocated collection, which are interpolated to a regular grid, the spacing of which corresponds to the GERB sampling distance. However, the native resolution of the GERB products (higher than this sampling distance and a function of wavelength) is retained, and no correction for the spatial variation in the instrument response is made. Thus each measurement represents a non-uniform spatial average at the native GERB resolution centered on that grid point. The spatial variation of the weighting is determined by the average of the point spread functions (PSFs) of the pixels that contribute to that point. To compare both datasets a filter simulating the PSF (see Fig. 3.26) of the GERB detector from the must be applied to the SEVIRI image. This filter has been derived from the information contained in the GERB documentation (Russell et al., 2006).

In Figure 3.27 the result of the filtering (or the applying of the PSF) can be observed. Fig. 3.27A is the GERB SW irradiance and B and C are the non-filtered and the filtered SEVIRI irradiances. It can be seen that the use of the PSF makes A and C more homogeneous than A and B. In the validation of the SEVIRI algorithms with GERB data, this filter has been applied to all SEVIRI images reducing the scattering (see Fig. 3.28).

⁵Sunglint is a phenomenon that occurs when the Sun reflects off the surface of the ocean at the same angle that a satellite sensor is viewing the surface.

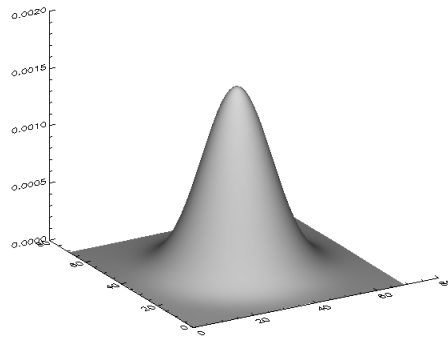


Figure 3.26: Simulated GERB point spread function.

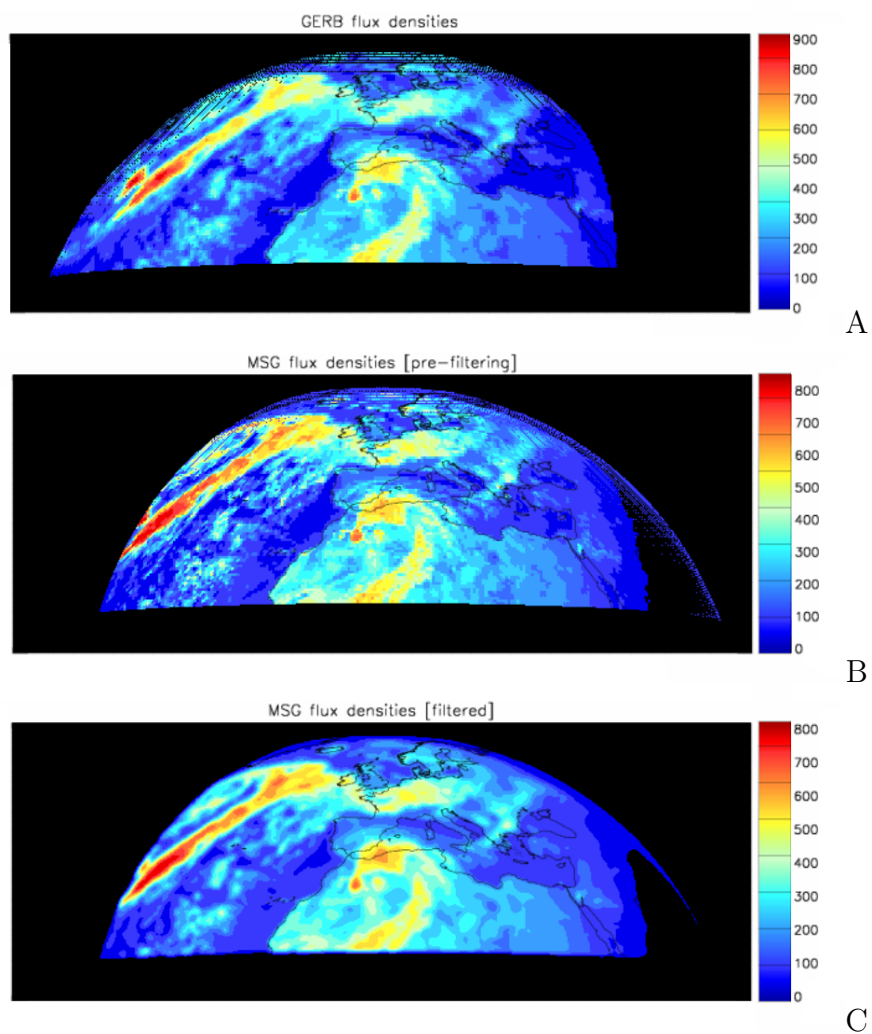


Figure 3.27: Irradiance in the SW range (W/m^2). A) measured by GERB. B) computed with SEVIRI. C) computed with SEVIRI and filtered.

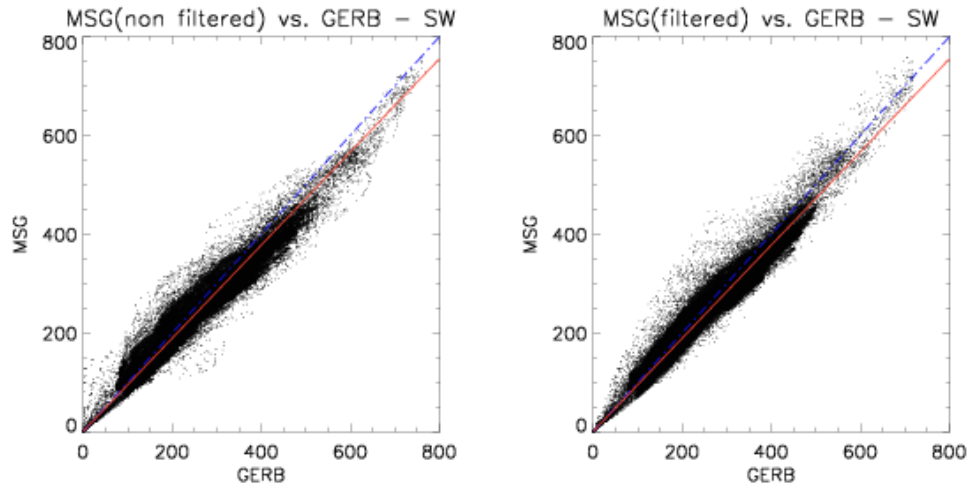


Figure 3.28: GERB irradiance vs. MSG/SEVIRI irradiance in the LW range (W/m^2). Left: without the PSF. Right: with the PSF. Date: 12/Jun/06 0730 UTC.

3.4.2 Validation of the MSG/SEVIRI irradiance algorithms

The validation of the SW and LW irradiance retrieval methods has been performed comparing the algorithm results to the measurements provided by the narrowband instruments GERB and CERES and carefully analysing all sorts of possible discrepancies. This analysis has been carried out in the SEVIRI satellite projection so the irradiances measured by GERB and CERES have been projected as described above onto the SEVIRI grid, the grid the algorithm results are in.

Validation of SEVIRI-retrieved irradiances with CERES measurements

Data used for this validation correspond to 12 scenes in the year 2004. These scenes have been selected for consistency with previous works (Krebs, 2006). Scenes have been selected to cover a wide range of day times and satellite viewing angles.

In the first place, a direct comparison of the irradiance computed with the SEVIRI based algorithms (hereafter *SEVIRI irradiance*) and that measured by CERES has been carried out. Irradiances are mapped by means of the modified nearest neighbour method described in section 3.4.1. Data are displayed in a 2D scatter plot: the SEVIRI irradiance vs. the CERES irradiance and fitted to a straight line by linear regression. A perfect fit should fulfil the equation $y = mx$ with $R^2 = 100\%$ and $m = 1$.

A typical case is shown in Figure 3.29 and its results on Table 3.3. To analyse the effect of outliers in the fit, the results when one every one hundred points is used are also shown in parentheses. The remaining cases are found in Appendix B. It can be seen that there is a high correlation (present in all images studied), especially in LW, but there are discrepancies between both irradiances. The SEVIRI irradiance is usually higher than the CERES irradiance over bright surfaces such as the desert and clouds, and it is related to their three-dimensional structure. The different angles under which CERES and SEVIRI observe the

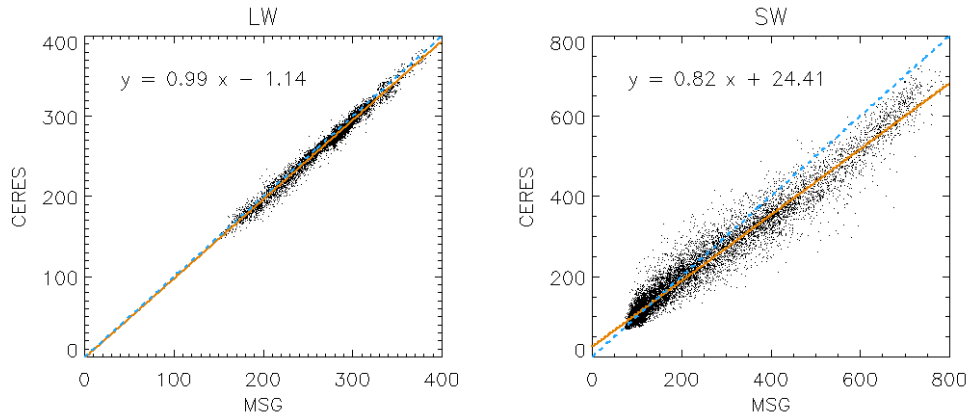


Figure 3.29: MSG/SEVIRI irradiance vs. Terra/CERES irradiance (W/m^2) in LW (left) and SW (right). Orange line: linear fit (fit equation displayed). Blue line: ideal 1:1 case. Date: 8/Jul/04 1200 UTC.

Parameter	Longwave	Shortwave
Slope	0.99 (0.99)	0.82 (0.82)
R^2	98.93 (98.92)	97.83 (97.83)
Mean irradiance (W/m^2)	282.48 (282.55)	224.87 (223.27)
RMS (W/m^2)	6.67 (6.66)	43.24 (42.78)
Bias (W/m^2)	-4.62 (-4.64)	-15.67 (-15.15)

Table 3.3: MSG/SEVIRI irradiance vs. Terra/CERES irradiance: slope, correlation coefficient, mean irradiance, root mean square and mean bias of the case depicted in Figure 3.29. In (), the results of the same analysis selecting only one every 100 points.

scene lead to different results. For lower values of the SW irradiance, that is, over non-bright surfaces such as the ocean, this overestimation is not present or is lower.

In order to analyse the cause of the discrepancies in the irradiances, a series of parameters likely to have an influence on the retrievals have been separately studied. The relative difference between both irradiances (from CERES/Terra and SEVIRI/MSG) has been computed, and the influence of each parameter in the relative difference has been studied. The parameters analysed are latitude, difference between overpass times of Terra and Meteosat-8 satellites, sun zenith angle, satellite zenith angle, cloud cover and cirrus cover.

The relative differences, RD , have been assessed according to the following equation.

$$RD = \frac{F(SEVIRI) - F(CERES)}{F(SEVIRI)} \times 100(\%) \quad (3.20)$$

Where $F(SEVIRI)$ is the irradiance retrieved from the SEVIRI algorithms (neural network in SW and multilinear parameterisation in LW) and $F(CERES)$ is the irradiance retrieved by the CERES observations.

The parameters though likely to influence the calculations are analysed below. Given that all scenes show the same behaviour with respect to each parameter, only a single scene is shown as an example. Additional examples are listed at the Appendix C for reference.

Different overpass times The first of the parameters analysed is the difference of the overpasses between Terra/CERES and MSG/SEVIRI. The scans are not simultaneous, and thus the scene is likely to show a discrepancy. Some structures such as clouds might have moved, evolved or disappeared, and the solar zenith angle has changed. If the different overpass times are responsible for the discrepancies, it is expected that the difference between both images will be low when the overpass difference time is low, and it will increase when the overpass difference time is higher.

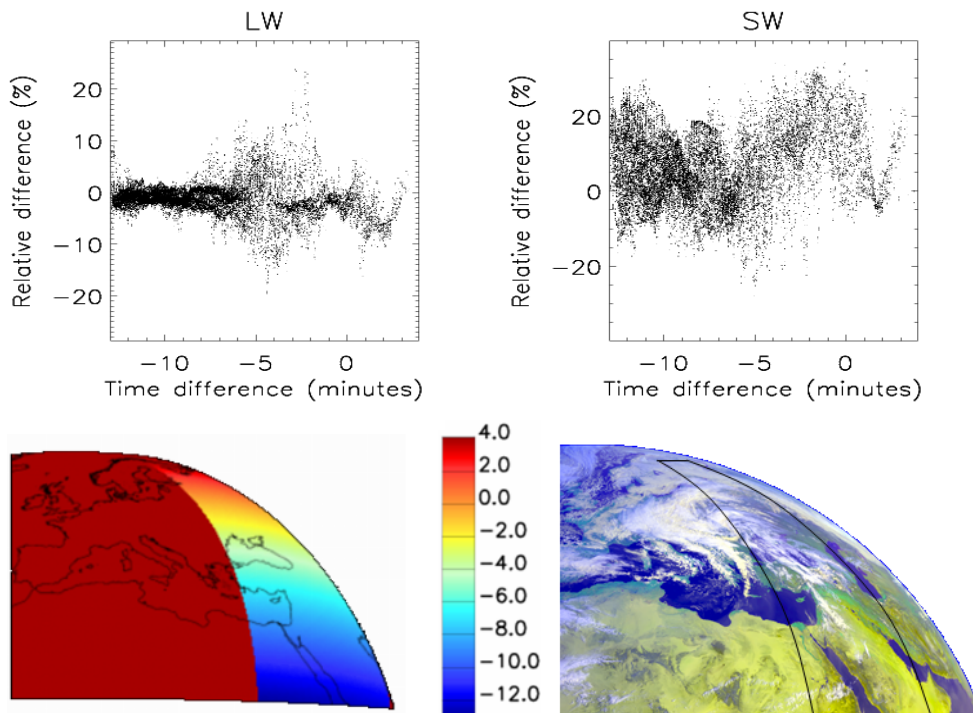


Figure 3.30: Above: LW and SW relative differences vs. time differences (Δt minutes) between CERES and SEVIRI overpasses. $\Delta t > 0$ SEVIRI scans before CERES, $\Delta t < 0$ CERES scans before SEVIRI. Below, left: Time difference in minutes $t(\text{CERES})-t(\text{SEVIRI})$. Below, right: Corresponding false colour composite. Date: 24/Mar/04 0800 UTC.

For instance, in the example 3.30 the CERES overpass took approximately 20 minutes. The MSG scan of the same region lasts less than 6 minutes. If the overpass time delay had been responsible for the discrepancies, a higher relative difference would have been present in the region with higher time differences. However, no temporal-related difference is observed, the minimum relative difference in LW is to be found when the difference between scans is between -12 and -7 minutes and the maximum in LW between -5 and 0 minutes difference. The relative differences in the shortwave case show also larger discrepancies between -5 and 0 minutes. Results in Fig. 3.30 top-left and top-right correspond to the time differences

depicted in Fig. 3.30 bottom-left and for the region of the globe in Fig. 3.30 bottom-right.

Latitude If there is a latitude dependency, it is expected to provide larger errors with increasing latitude. CERES' viewing angle varies, between 0 at the centre of the cross-track scan and 67° near the borders, whereas SEVIRI has an increasing viewing angle with latitude and longitude. This can lead to misplacement of some cloud structures several kilometers from their real position, especially high clouds.

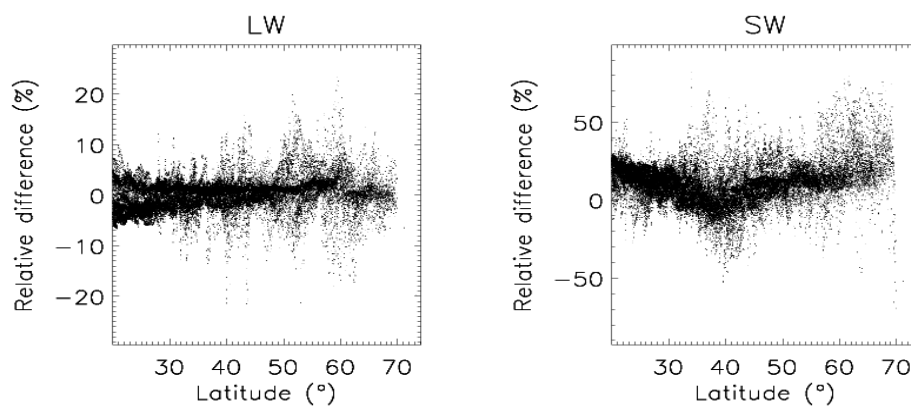


Figure 3.31: Relative difference vs. latitude. Left: Longwave. Right: Shortwave. Date: 14/Jun/04 0915 UTC.

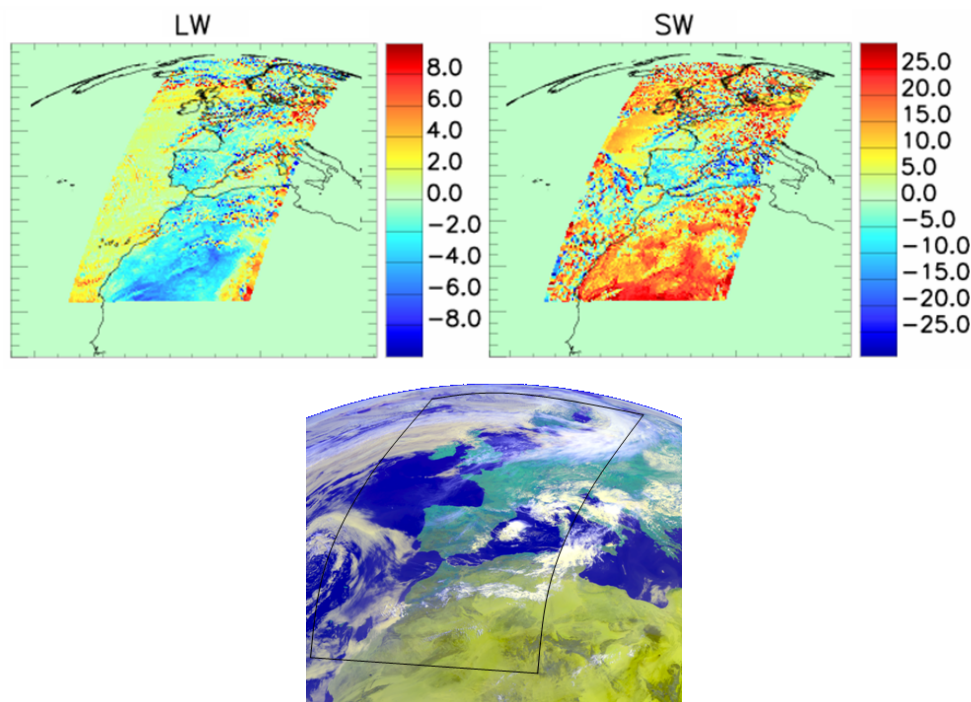


Figure 3.32: Above: LW and SW relative differences displayed over their corresponding regions. Below: False colour composite of the same scene. Date: 14/Jun/04 0915 UTC.

No clear latitudinal dependency of the discrepancies is found in any of the scenes. In the example depicted in Fig. 3.31 there is a minimum error around 40° North. The regions depicted in Fig. 3.32 correspond to the Fig. 3.31 relative difference plots. It can be seen that an overestimation of the irradiance in the SW occurs over bright and warm surfaces such as the Sahara desert. Then, over Spain (latitude 40° N) there is a decrease in the discrepancies, hence the minimum at that latitude, and an strong increase again towards the north. This increase is coincident with the increase of cloudiness but it is not due to the higher latitude *per se*. A more thorough study of the influence of cloudiness is shown below.

Solar zenith angle Fig. 3.33 shows an example of the dependency of the relative differences on the solar zenith angle. More examples are shown in Appendix C. None of the cases show an increase or decrease of the relative differences with the solar zenith angle. There is, again, an increase on the discrepancies where a cloudy region is present (solar zenith angle 40°).

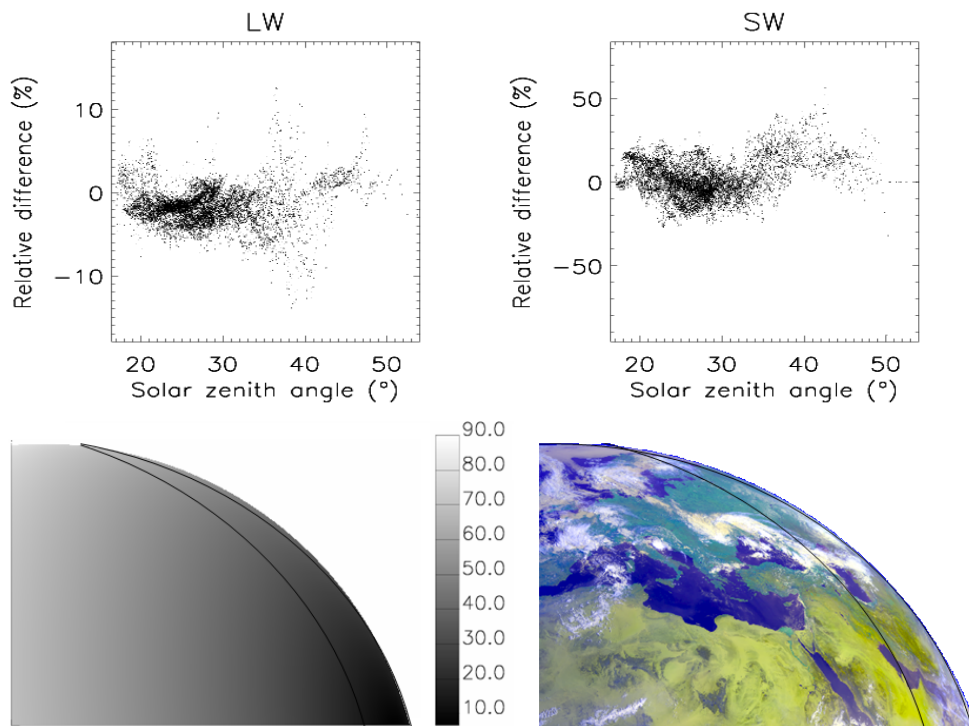


Figure 3.33: Top: relative difference vs. solar zenith angle. Left: Longwave; right: Shortwave. Bottom: left: Solar zenith angle; right: false colour composite. Date: 8/Apr/04 0730 UTC.

Satellite zenith angle Due to the fact that MSG and Terra observe the same structures under different angles, it might be possible that the satellite zenith angle (the angle between the zenith and the position of the satellite) has an influence on the computation of the irradiances. Fig. 3.34 shows an example of the dependence of the relative difference with respect to the MSG satellite zenith angle. Despite being able to see that high satellite zenith angles are related to an increase of the errors in the SW range, this behaviour is not present

in the examples in Appendix C. Figure 3.34 shows that cloudiness is present in this scene at higher satellite zenith angles.

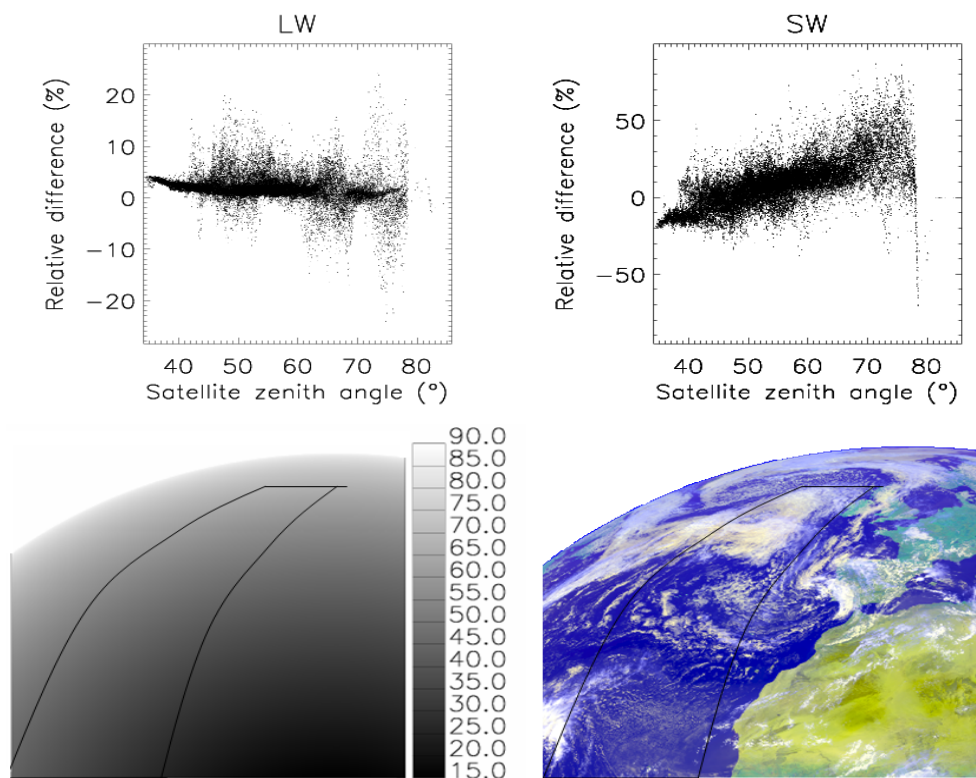


Figure 3.34: Top: Relative difference vs. satellite zenith angle. Left: Longwave. Right: Shortwave. Bottom: Left: satellite zenith angle. Right: false colour composite. Date: 02/Sep/04 1245 UTC.

Cloud cover The discrepancies found in Table 3.3 and in Table B.1 in Appendix D cannot be attributed to any geographical (latitude), geometrical (zenith angles) or temporal parameters. Instead, a careful analysis of the images points out the cloud cover as a possible source of discrepancies.

To discriminate between cloudy and cloud-free pixels, the MODIS cloud mask has been used. Each MODIS cloud mask file is a 5 minute scan. Therefore, for each CERES scan used in this analysis, three MODIS cloud mask files have been required. The cloud mask corresponds exactly to the time and region observed by CERES, given that both instruments are on board of Terra.

MODIS cloud cover has been projected on the same grid as SEVIRI and CERES. Given that MODIS pixels are smaller than SEVIRI or CERES pixels, the amount of cloudy pixels within each mapped pixel provides a fraction of the cloud coverage of that pixel. Zero cloud cover means clear-sky and cloud cover 1 means full cover. A tendency towards greater errors with increasing cloud cover can be seen despite the great scattering present in Fig. 3.35, where also the linear fit equation is shown. In the LW case, the $y = mx + b$ fit parameters are $m = 1.32 \pm 0.02$ and $b = 0.096 \pm 0.005$. In the SW case, $m = 13.52 \pm 0.02$ and

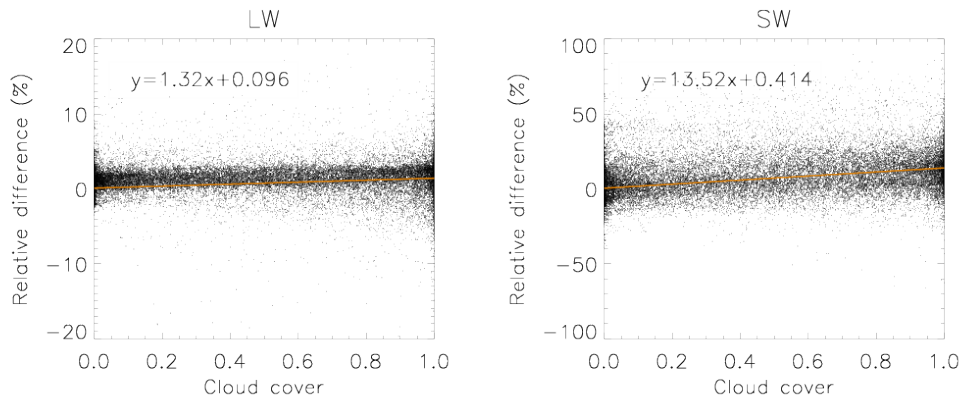


Figure 3.35: Relative difference vs. cloud cover in LW (left) and SW (right). Orange line: linear fit. Fit equation displayed on the corresponding plot.

$b = 0.414 \pm 0.007$. Note that the scales are different in the LW and SW because LW shows smaller discrepancies. It can be seen that the cloud cover has an influence on the increase of the relative differences.

Cirrus cover This work aims to assess the influence of contrails and aviation induced cloudiness in the climate system. The previous parameter has shown an increase of the discrepancies when increasing the cloud cover, so it is of particular interest to see if this behaviour is also present in the cirrus cover.

The cirrus cover used is the MeCIDA (Krebs et al., 2007) cirrus mask. Fig. 3.36 shows the results for all cases studied. The fit equation parameters are $m = 0.026 \pm 0.003$ and $b = 0.212 \pm 0.002$ for the LW case and $m = 0.34 \pm 0.07$ and $b = 3.997 \pm 0.045$ for the SW. In this case, although there is still a small increase in the coverage, it is less than in the previous case, where all clouds were considered. The 3-dimensional structure of clouds strongly influences the retrieval of the irradiances, but this influence is smaller in this case because cirrus clouds are very thin and flat structures.

In short, the CERES instrument is a widely used tool to study irradiances, it has undergone a very comprehensive validation (Loeb et al., 2005), but it is not suitable for the study of the evolution of contrails. This is due to the poor temporal resolution of the scans, missing information about the temporal evolution, and to the pixel size, which is too large and ignores smaller structures such as fractioned clouds, small cumuli and narrow cirrus. These limitations are easily overcome with the SEVIRI-based algorithms. A closer analysis has shown that these algorithms present a slight systematic overestimation of the relative difference when they are used to compute the irradiances over bright areas such as clouds or the desert. The SEVIRI algorithms also show an increase in the CERES/SEVIRI relative differences when cloudiness is present. It is thought that the 3-dimensional structure of clouds might be the reason for the increase. In order to confirm this point, measurements from instruments that share exactly the same viewing angle of each pixel in each scene must be compared. This can only be done using the GERB instrument.

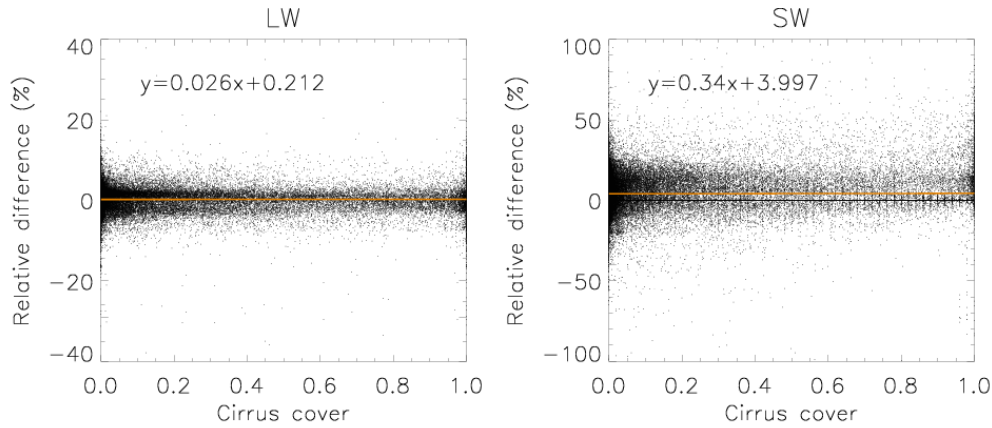


Figure 3.36: Relative difference vs. cirrus cover in (left) LW (right) SW. Orange line: linear fit. Fit equation displayed on the corresponding plot.

Validation of SEVIRI retrieved irradiances with GERB measurements

Due to some calibration problems with the GERB instrument, it was impossible to use for the validation the same scenes previously used in the SEVIRI vs. CERES case. Nevertheless, scenes have been chosen so that they are representative of the different times of the day. May and June scenes have been used to aim for greater insolation in the Northern Hemisphere.

Data are downloaded from the GERB website upon request. GERB data have been mapped onto the SEVIRI grid and SEVIRI-based data have been mapped and filtered as described in Section 3.4.1 to make the analysis possible.

A typical example is shown below (see Figure 3.37) and further examples are shown in Appendix D. It is clear that this analysis shows better results, closer to the ideal case of $R^2=100\%$ and slope = 1.00. Comparing the results in Table 3.4 with the results in Table 3.3, it can be seen that there is a clear improvement in both the LW and SW regions. More examples of this improvement can also be seen comparing the CERES vs. SEVIRI results in Appendix B with the GERB vs. SEVIRI results in Appendix D.

Parameter	Longwave	Shortwave
Slope	0.99 (0.99)	0.91 (0.91)
R^2	98.61 (98.58)	96.53 (96.49)
Mean irradiance (W/m^2)	266.35 (266.25)	251.95 (252.24)
RMS (W/m^2)	7.32 (7.30)	31.75 (31.87)
Bias (W/m^2)	-3.24 (-3.20)	-12.18 (-12.30)

Table 3.4: MSG/SEVIRI irradiance vs. MSG/GERB irradiance: slope, correlation coefficient, mean irradiance, root mean square and mean bias of the case depicted in Figure 3.37. In (), the results of the same analysis selecting only one every 100 points.

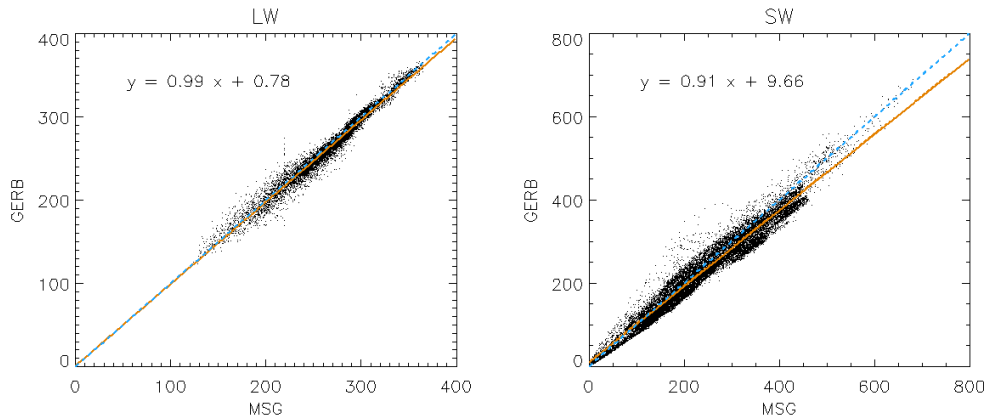


Figure 3.37: MSG/SEVIRI irradiance vs. Terra/GERB irradiance (W/m^2) in LW (left) and SW (right). Yellow line is the linear fit. Fit equation displayed. Date: 12-Jun-06, 0730 UTC.

According to the GERB quality summary (Russell et al., 2006), users should be aware that values determined for data acquired for satellite viewing angles $> 70^\circ$ will be subject to increased errors. For these higher viewing angles the three dimensional nature of clouds and the increased atmospheric path for Rayleigh scattering cause a growth in apparent cloudiness and increasing scene identification errors (Diekmann and Smith, 1988; Smith and Manalo-Smith, 1995). Thus, the wrong angular dependency model (ADM) is selected for computing irradiance from radiance. Also, the footprint of the pixel on the Earth grows rapidly beyond 70° , so that scenes and ADMs are highly mixed. These limitations will be taken into account when performing the statistical analysis of the life cycle of contrails. The GERB team has reported an additional problem in the radiance to irradiance conversion for thin high level clouds in the GERB products (Russell et al., 2006). It can result in a relative error on the LW irradiance up to 20% for thin high level clouds ($0.5 < \text{optical thickness at } 0.55 \mu\text{m} < 3$, height $> 6\text{km}$), so a special cirrus cloud analysis in this validation will not be included.

3.4.3 Discussion

The validation with GERB shows remarkably better results than the comparison with CERES. GERB and SEVIRI share the same viewing geometry and present better agreement than CERES and SEVIRI. It can be concluded that the discrepancies between the CERES and SEVIRI irradiances are due to the viewing geometry. The discrepancies are not due to the irradiance computation method of GERB because it uses thoroughly validated angular dependency models (ADMs) to perform the radiance-to-irradiance conversion, similarly to CERES (Harries et al., 2005; Mlynczak et al., 2006). The overestimation found over bright surfaces is present also in this case because GERB ADMs are related to CERES ADMs. In the CERES validation, it was proved that the higher relative differences were found when studying clouds (as it could be seen in Fig. 3.32 and assessed in Fig. 3.35) and that an increase in cloud cover led to an increase in the relative differences. When eliminating the viewing angle dependency by performing the validation with instruments sharing the same viewing angle, the discrepancies disappear. It is evident that a geostationary satellite will see a cloud placed at 50°N differently than a polar orbiting satellite will see the same cloud,

giving rise to the previously mentioned discrepancies. The overestimation of irradiances by SEVIRI found in both validations, mainly over bright structures such as clouds or the desert, could be also related to 3D effects but further work is needed to confirm this statement.

Thus, it has been shown that the LW as well as the SW irradiance retrieval algorithms for SEVIRI are suitable for cloud studies with the advantage of the high SEVIRI temporal and spatial resolution.

A validation of the outgoing longwave and reflected solar irradiance algorithms was previously performed by Krebs (2006), who carried out a comparison between MSG/SEVIRI and Terra/CERES irradiances. To reduce the computing time, a $1^\circ \times 1^\circ$ grid was chosen to perform the validation. This inevitably averaged the irradiances over very large areas missing the influence of small structures. An exhaustive analysis of the discrepancies found was not included although it is mentioned that the possible cause is the 3D effect of clouds. At the time of that work GERB was still not operating.

3.5 Radiative forcing

The radiative forcing, RF, is defined as in Equation 2.21. The net forcing is the sum of both shortwave and longwave net contributions, as described in Equation 2.20. To compute the irradiances corresponding to the contrail and contrail-cirrus pixels, the algorithms described in Sections 3.2 and 3.3 have been used. These algorithms provide the outgoing longwave and reflected solar irradiance for each pixel of the image. To establish the radiative forcing of the contrail, it is necessary to subtract the irradiance of the contrail from the irradiance of that exact same scene in absence of the contrail. Such a retrieval presents an impossibility inherent to the method. Palikonda et al. (2001) proposed to select all pixels in the surrounding of the contrail and eliminate those belonging to cirrus clouds; the remaining would then be considered the reference state of the atmosphere. This requires the computation of a cirrus mask and increases notably the computation time. Moreover, if a contrail is created among natural cirrus clouds, this procedure would eliminate the actual reference state of the atmosphere (covered by cirrus) and consider that the contrail effect is that of a contrail over a cloud-free area. A large number of the contrails seen in this work have been wind-drifted to cloudy areas, some of them cirrus clouds. Meyer et al. (2002) studied the evolution of the brightness temperature and the brightness temperature difference to establish the contrail boundary and then select the surrounding pixels as the reference state of the atmosphere. This method would lead to errors in the case of contrail clusters, because it would consider equally neighbouring contrail-cirrus pixels and the actual reference state.

To establish the reference state of the atmosphere it is necessary to take into account that contrails can be found isolated, over cloudy areas, among pre-existing cirrus clouds or in contrail clusters or any combination thereof. In this work, the reference state of the atmosphere has been established taking all pixels within a 1-pixel distance from the contrail (see Fig. 3.38, left) and selecting from them the ones that are more representative from the background. This is made as follows: in the first place, a distinction between night and daytime scenes has been made:

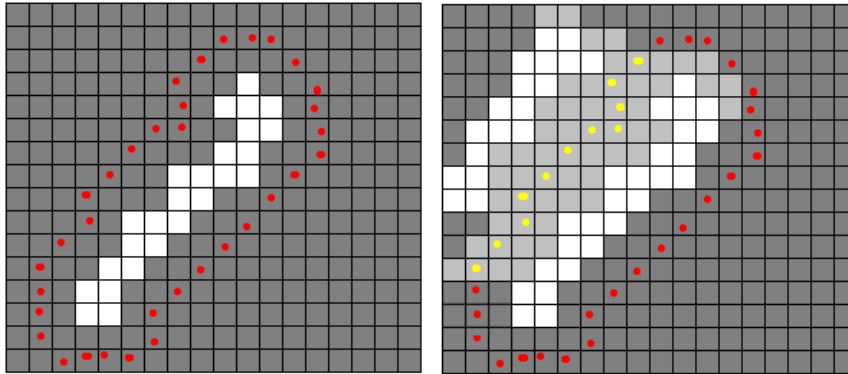


Figure 3.38: Left: schematic representation of an isolated contrail (white), its background (dark grey), and the pixels considered as the reference state (red). Right: schematic representation of a contrail cluster: when another contrail is present causing a thin cloud veil to extend between them (light grey), only pixels marked in red must be considered as the reference state.

a) At daytime, the average of the 40% darkest pixels is considered as the reference state. Should the contrail occur in a cloud-free area, those pixels will be representative of the background. Should it be over a partly cloud covered area, that 40% will favour the surface pixels and, to a lesser extent, also account for the surrounding clouds. This is made to favour the selection of ground pixels instead of the selection of pixels belonging to the thin cloud veil that forms in contrail clusters (see Fig. 3.38, right). If the contrail occurs in or is drifted to an area fully covered by cirrus clouds, this method will not neglect the pre-existing cirrus forcing, and the reference state considered will be that of a cirrus covered sky.

b) At nighttime, the average of the 40% warmest pixels is considered as the background. This method is not used at daytime because the presence of low warm clouds that might produce a similar signal to the satellite than the land/sea below can lead to chose the wrong pixels as reference. As in the previous case, in the case of contrail clusters, this method will favour the selection of the ground pixels (darker and/or warmer) in spite of the aviation-induced cloudy pixels in the neighbourhood. In a case where these pixels include the shadow cast by the contrail-cirrus on the surface, the shadow pixels would be considered as the emission from the ground in the contrail-free case leading to errors. Nevertheless, these do not represent a significant amount of the cases due to the very specific Sun-Earth-satellite geometry conditions that must be fulfilled to produce a shadow at the exact location.

3.6 Optical thickness

The studies determining cloud optical thickness from passive remote sensing instruments are based on visible and near-infrared radiometers. In some cases, a retrieval of both cloud optical thickness and particle size can be made by simultaneously measuring the reflection function at a visible and a near-infrared wavelength and comparing the resulting measurements with theoretical calculations (King and Nakajima, 1990). The underlying principle on which these techniques are based is the fact that the reflection function of clouds at a

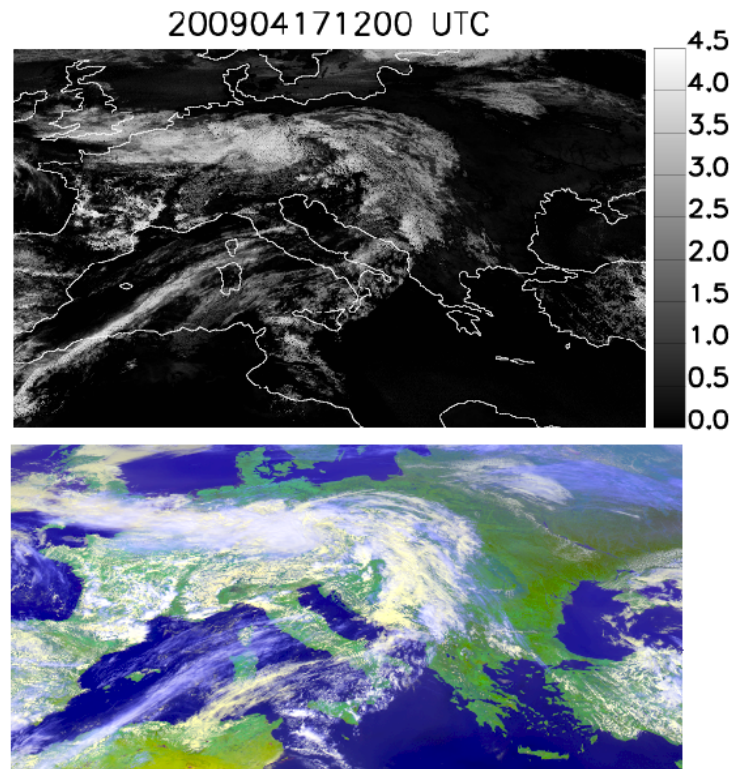


Figure 3.39: Top: optical thickness computed by the neural network for the region depicted, date: 17/Apr/09, 1200 UTC. Bottom: false colour composite of the same scene.

non-absorbing band in the visible wavelength is primarily a function of the cloud optical thickness. Platnick et al. (2001) developed an algorithm combining two shortwave infrared bands (1.62 and 2.13 μm), for cloud optical property retrievals for water clouds. But in this retrieval some errors are expected to be encountered when retrieving cloud effective particle radius and optical thickness in the case when ice clouds are present (Platnick et al., 2001).

In this work, the optical thickness will be retrieved by means of infrared channels, so optical thickness of clouds can also be retrieved at nighttime. The simulations described in Section 3.2 and in Krebs et al. (2007) based on the *libRadtran* (Mayer and Kylling, 2005) package have also been used to train a neural network developed by H. Mannstein at DLR to retrieve optical thickness. This method, based on SEVIRI brightness temperatures, has the advantage that it provides the optical thickness of the clouds in the same spatial and temporal resolution used to track the contrails and contrail-cirrus. The derived optical thickness corresponds to 550 nm. An example of the results derived by this neural network is shown in Fig. 3.39. It can be seen that the results of the optical thickness retrieval match the expected values.

Figure 3.40 shows a comparison between the optical depth retrieved by means of the neural network and measurements taken during the LUAMI campaign (Lindenberg Upper Air Methods Intercomparison). The LUAMI data here plotted are aircraft-borne LIDAR measurements during a 3-hour flight over Germany. The agreement is not perfect, but both sources show the same behaviour, even though the neural network retrieval method does not use any channel of SEVIRI in the visible wavelengths. Some of the discrepancies are due to

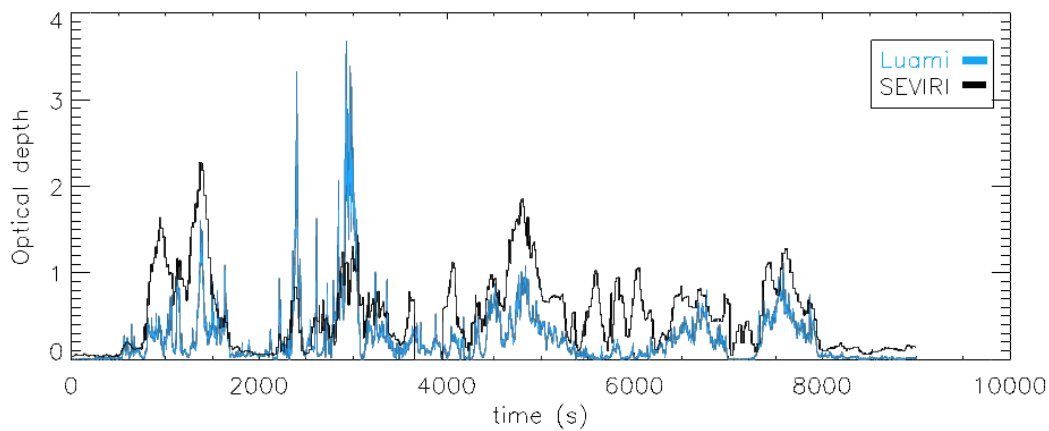


Figure 3.40: Blue: optical thickness measured at the LUAMI campaign on the 18th of October 2008. Black: corresponding optical thickness computed by the neural network from SEVIRI data.

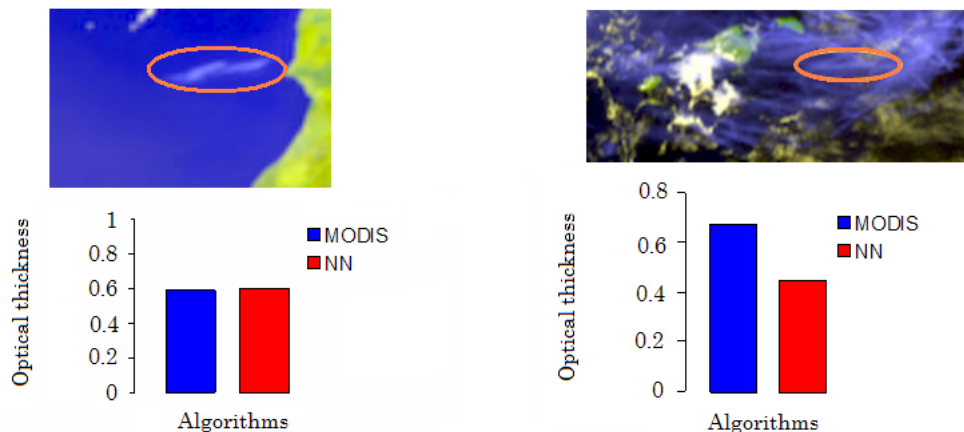


Figure 3.41: Blue: optical thickness retrieved by the MODIS optical thickness product. Red: corresponding optical thickness computed by the neural network (NN) from SEVIRI data.

the presence of underlying clouds below an optically thin cloud, where the SEVIRI based neural network provides an optical depth that is a result of the whole column. Furthermore, the SEVIRI retrieved optical thickness is representative of a large area determined by the pixel size at that latitude, and the LUAMI measured optical thickness is almost a point measurement.

Case study validations using the MODIS cloud optical depth product have shown a good agreement for isolated contrails and a slight difference of 0.2 in a more complicated scene, as seen in the examples in Figure 3.41. Nevertheless, the typical optical thickness of a contrail is very low and further validations are needed. This optical thickness retrieval method based in the SEVIRI sensor will be used in the course of this work in the knowledge that the results must be interpreted with care. Optical thickness products from satellite sensors such as CALIPSO LIDAR data could be used to improve the retrieval of the optical thickness by the neural network.

Chapter 4

Life cycle of contrails: results

In this chapter, the evolution of the aircraft induced clouds from their linear contrail phase to their cirrus phase has been studied. In particular, the coverage, spatial distribution, average duration, optical thickness and radiative forcing of aircraft induced clouds have been computed. First, a research on case studies has been performed (Section 4.1). Then, the results of running ACTA on four months of data are presented (Section 4.2).

The *coverage* of the contrails has been computed taking into account the number of pixels and the average latitude and longitude of the scene, because SEVIRI pixel sizes are latitude and longitude dependent (see Fig. 2.9). The *optical thickness* has been derived using an algorithm based only on SEVIRI infrared channels (see Section 3.6). The *radiative forcing* is defined as in Equation 2.21. A positive forcing implies that the outgoing irradiance in the contrail-free situation is larger than that in the presence of contrail, so the contrail causes a warming of the atmosphere below. A negative forcing means, therefore, that the presence of the contrail causes a cooling.

4.1 Case Studies

Before undergoing the study of a larger number of cases, some case studies have been selected in order to deepen in the knowledge of how contrail and contrail-cirrus properties evolve and to adapt it to systematic studies to prevent any possible mistake. The observation of single events increases the knowledge on the behaviour of contrails and thus will be used as a paradigm to develop and tune the algorithms used to study the evolution of their physical properties.

To select the cases three criteria were taken into consideration: day/night behaviour, land/sea behaviour, presence/absence of surrounding cloudiness. The contrails and the neighbouring pixels needed to account for the reference state of the atmosphere have been selected manually in each step of the evolution. The following information has been retrieved: duration, evolution of the optical thickness, and evolution of the outgoing irradiance in the longwave and in the shortwave ranges. This has been compared with the ACTA results. When choosing the reference state of the atmosphere, the automatic method can select pixels closer to the

original contrail than the method by hand, so the inevitable different choice of background pixels between the human and the automatic detection can vary up to several W/m^2 .

4.1.1 Case 1

The first case study is a contrail over sea in the evening, situated in the North Atlantic region, with other contrail structures nearby (see Fig. 4.1). It grows and spreads until it becomes a wide thin cirrus cloud and merges with natural cirrus in the vicinity. The hand-derived evolution (black) of the radiative forcing and the automatic retrieval (blue) are shown in Fig. 4.2. A false colour composite of the same scene based on reflectance channels from SEVIRI cannot be provided for the observation is at nighttime.

The evolution of the optical thickness can be seen in Fig. 4.3, where the area within the blue box corresponds to the moments tracked by ACTA. The contrail tracking algorithm does not go any further into the past, not only because the contrail is weaker but also because the algorithm does not see a clear contrail signal and stops to prevent an erroneous tracking. The human detector can identify the weak signal the contrail produces when it is still young and optically thinner.

The lower optical thickness in the first stages of the development of the contrail is responsible for the low LW and SW radiative forcing that can be seen in the left and middle plots of Fig. 4.2. The absolute value of the SW forcing is very low because the contrail reflects very little sunlight due to a low optical thickness. ACTA needs a clear contrast with the background, causing the tracking backwards from the MODIS input to stop before the actual first satellite detection of the contrail. This is responsible for the absence of blue (automatic) line in the shortwave RF graph. In this particular case, ACTA has derived information only during nighttime. The low radiative forcing in the longwave range in the initial stages of the contrail evolution is due to the fact that the signal reaching the satellite is a combination of the cold contrail and the warm underlying background. The contrail quickly obtains from the ambient air the necessary humidity to grow larger and thicker, increasing therefore the forcing in the longwave range. As soon as the contrail has aged enough, the LW contribution stops increasing and the graph approaches $20 \text{ W}/\text{m}^2$, a value that is comparable to that of natural cirrus clouds (Chen et al., 2000). In the SW, only a few timesteps contribute to the forcing before the sun sets. The net forcing is, in this case, positive, meaning that this contrail has a warming effect. It can be seen that both retrieval methods are highly coincident, despite some differences due to the selection of the background pixels.

The total lifetime of the contrail until it merges with the surrounding cirrus clouds and is undistinguishable from them is 235 minutes; the time it remains automatically tracked is 155 minutes. The initial point of the tracking occurs 70 minutes after the contrail is visible from the SEVIRI instrument.

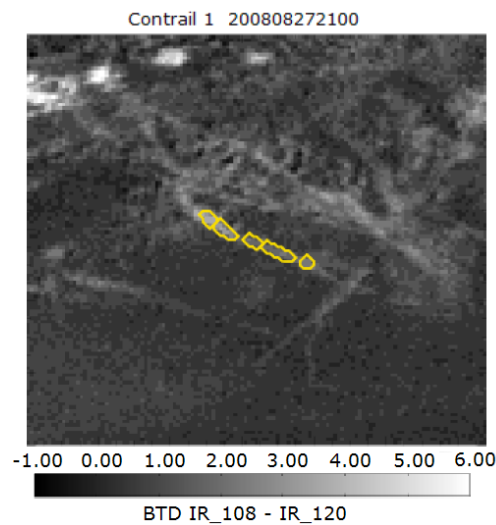


Figure 4.1: Date: 27 August 2008. 2100 UTC. The yellow line encloses the contrail studied in Case 1. Background: Brightness temperature difference image $10.8 \mu\text{m} - 12.0 \mu\text{m}$ (K).

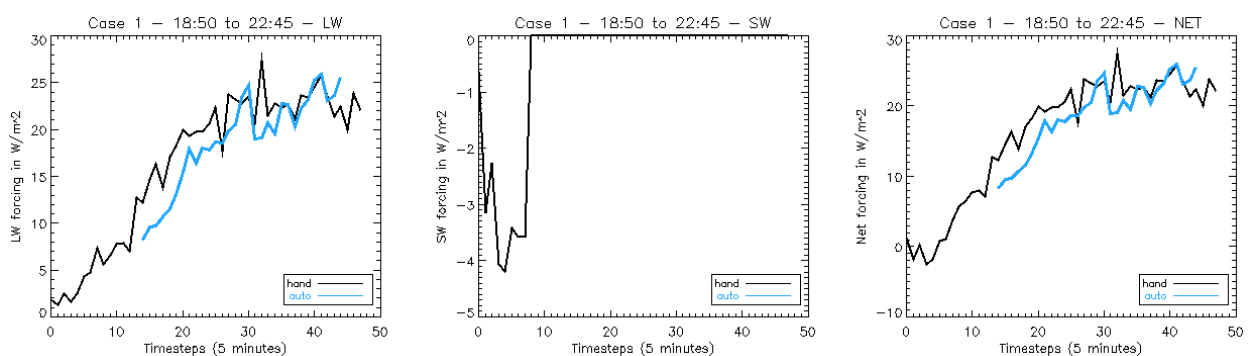


Figure 4.2: Date: 27 August 2008. 2100 UTC. Outgoing LW(left), SW(centre) and NET (right) forcing at TOA derived manually (black) and automatically (blue) due to the presence of a contrail

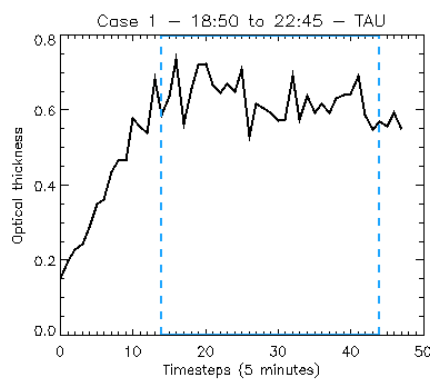


Figure 4.3: Date: 27 August 2008. 2100 UTC. Optical thickness of the hand-derived contrail. In blue: the time range coincident with ACTA results

4.1.2 Case 2

Case 2 (see Figure 4.4) is that of a very weak contrail isolated above sea that evolves until it eventually vanishes. It is located West of Corsica. ACTA sees a part of the development of the contrail in the middle of its lifetime despite the very low optical thickness (see Fig. 4.6). The difference between the hand-derived forcing and the automatic forcing due to the selection of the background pixels is similar to that encountered in Case 1: around 1 or 2 W/m^2 (see Fig. 4.5). The LW forcing is lower than expected because the contrail is transparent due to the low optical thickness. The net forcing is positive despite the fact that this is a daytime scene over sea, in this case the optical thickness is so low that the SW forcing does not outweigh the LW forcing. At daytime, the forcing due to the presence of the contrail has a thermal contribution and a contribution due to the reflexion of the solar irradiance and the SW contribution may outweigh that of the LW, leading to a cooling. In this case it can be seen that very thin contrails at daytime may as well have a net warming effect.

The optical thickness of this contrail is extremely low ($\tau \sim 0.05$), as depicted on Fig. 4.6. The area in blue shows the time range where the algorithm detects and tracks its existence. It can be seen that it corresponds to a moment where the optical thickness is slightly higher causing a stronger contrast with the background and thus a stronger signal reaches the satellite enabling its detection and tracking.

The total lifetime of the contrail assessed by the human observation from a geostationary satellite is 80 minutes, and the lifetime derived from the automatic detection is 35 minutes. The first detection is possible 15 minutes after the occurrence of the contrail.

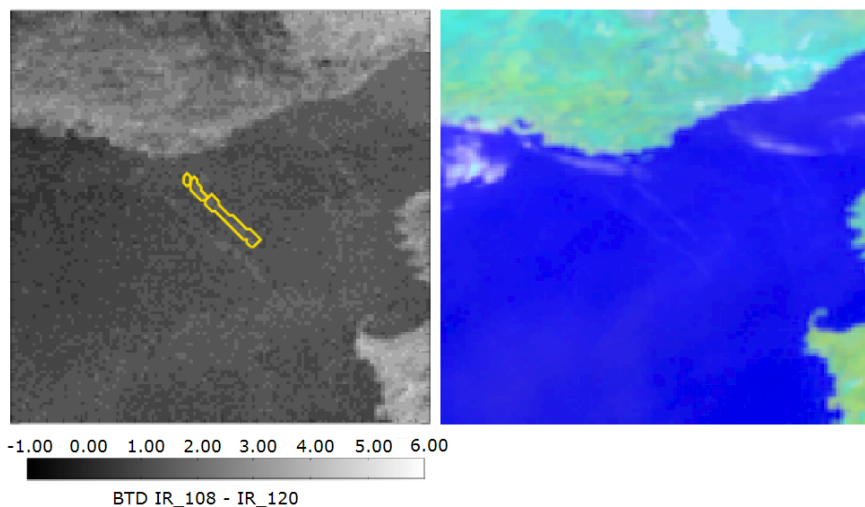


Figure 4.4: Date: 30 August 2008. 1110 UTC. Case 2. Right: The yellow line encloses the contrail tracked. Background: Brightness temperature difference image $10.8 \mu m - 12.0 \mu m$ (K). Left: False colour image of the scene.

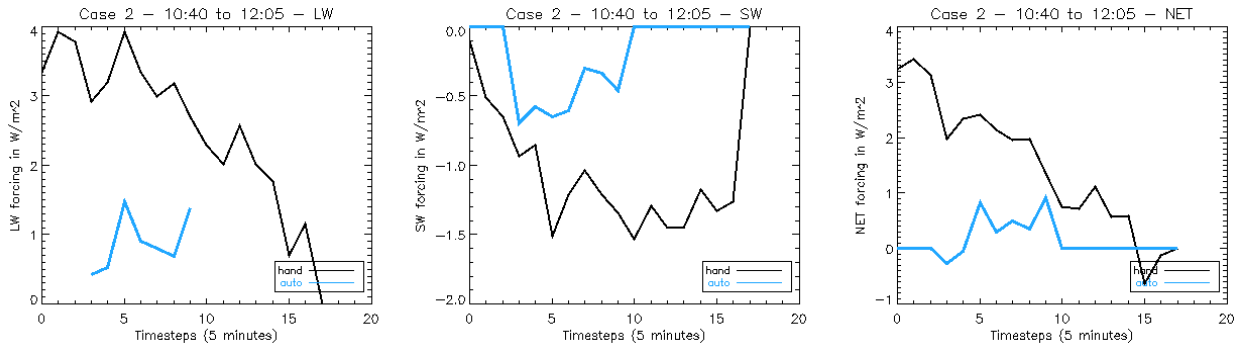


Figure 4.5: Date: 30 August 2008. Outgoing LW(left), SW(centre) and NET (right) forcing at TOA derived manually (black) and automatically (blue) due to the presence of a contrail

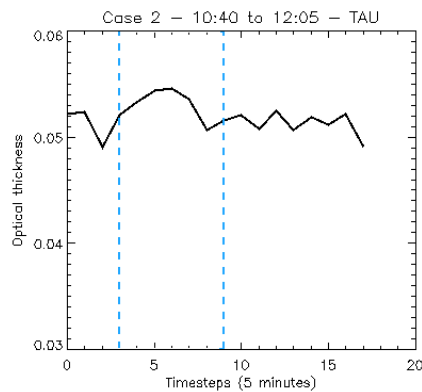


Figure 4.6: Date: 30 August 2008. Optical thickness of the hand-derived contrail. In blue: the time range coincident with ACTA results

4.1.3 Case 3

Case 3 is an isolated contrail over land. It is located on the Iberian peninsula. Fig. 4.7, right shows a RGB colour composite from SEVIRI channels; the left image shows the brightness temperature difference $10.8 \mu\text{m} - 12.0 \mu\text{m}$ corresponding to the same area and time. The contrail tracked appears outlined in yellow on the BTD image. In that moment of the tracking, the contrail is barely seen on the false colour composite due to the high reflectance of the background, so the SW forcing at that time is expected to be low. This is the opposite to what happened in Case 2, where the contrail's very low optical thickness was compensated by the low reflectance of the water surface allowing its identification.

The same RF pattern is shown in both the manual and the automatic retrieval. There is only a 5-minute delay for the automatic tracking, which lasts until the contrail signal begins to decrease. This is a contrail occurring during daytime, where the SW forcing outweighs the LW forcing, causing the net forcing to be negative. In its final stages the optical thickness of the contrail decreases and it becomes as bright as the background, -a land surface-, as expected. The signal reaching the satellite is stronger in the LW than in the SW range, explaining the net positive forcing in the final phase. A contrail of these characteristics over

a sea background would have caused a stronger SW forcing due to the low brightness of the sea surface in comparison to the land surface, causing the net forcing to be negative throughout the whole lifetime. This corroborates that solar and net forcing are strongly influenced by the brightness of the underlying surface and atmosphere and underlines the need to carry out separate studies of contrails depending on the land/water background

The total lifetime of the contrail is 80 minutes in the manual retrieval and 60 minutes in the automatic retrieval.

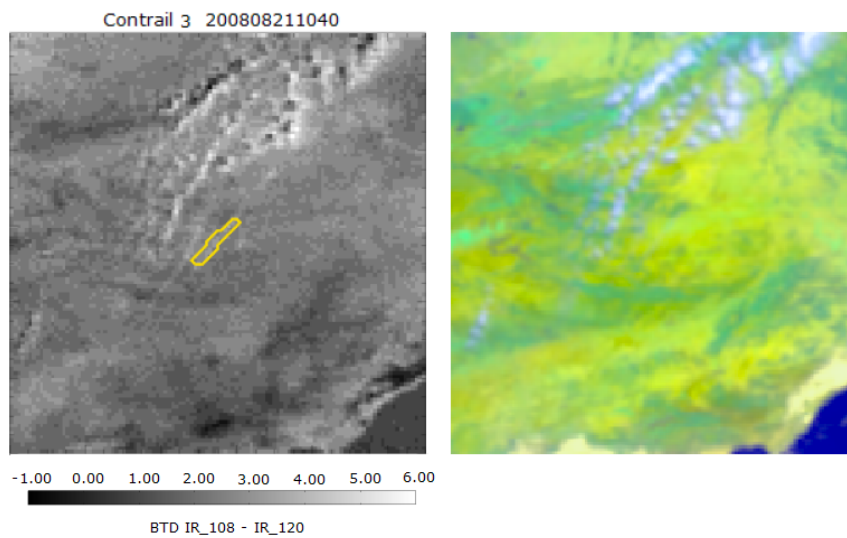


Figure 4.7: Date: 21 August 2008. 1040 UTC. Case 3. Right: The yellow line encloses the contrail tracked. Background: Brightness temperature difference image $10.8 \mu\text{m} - 12.0 \mu\text{m}$ (K). Left: False colour image of the scene.

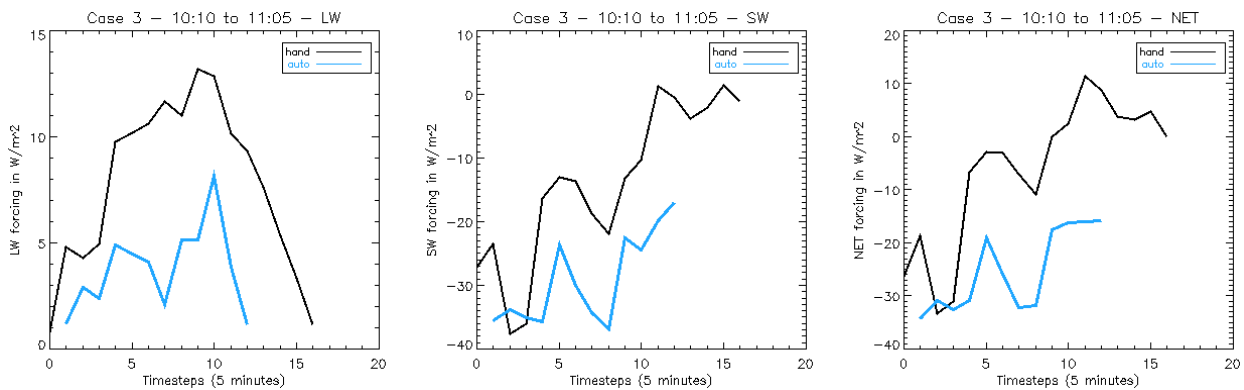


Figure 4.8: Date: 21 August 2008. Outgoing LW(left), SW(centre) and NET (right) forcing at TOA derived manually (black) and automatically (blue) due to the presence of a contrail

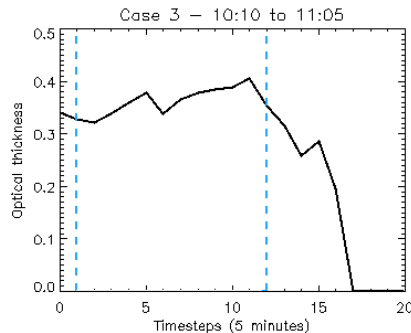


Figure 4.9: Date: 21 August 2008. Optical thickness of the hand-derived contrail. In blue: the time range coincident with ACTA results

4.1.4 Conclusions

The first stage of the study of the life cycle of contrails using the algorithm developed has consisted of the analysis of scenes with different scenarios (day/night, land/sea background, presence/absence of neighbouring clouds). The regions identified as contrails by the algorithms have been seen to belong to the tracked contrail with an extremely high accuracy.

The following conclusions can also be drawn from the case studies analysed:

- The lifetime of contrails is very variable. The automatic retrieval is dependent of the scene: it can cover either the first, the middle or the last stages of the life of the contrail-cirrus. The manual retrieval detects longer lifetimes than the automatic, and it has been proven impossible to assess a minimum delay valid for all scenes. The tracking algorithm developed is conservative and it is designed to stop if there is a possible error in the tracking, rendering the automatic lifetime retrieval in the case of cloudy and complicated scenes notably shorter than in other more simple cases. Errors could be triggered by the presence of other contrails or clouds nearby. Nevertheless, this design leads to very accurate results, as every region labeled as *contrail* actually belongs to the tracked contrail with an extremely high probability.
- The optical thickness can decrease smoothly and monotonously as the contrail-cirrus ages and spreads until it eventually vanishes, or remain constant if the contrail cirrus persists and merges with pre-existing cirrus clouds. ACTA has been able to follow extremely optically thin contrails if the contrast with the background is strong enough (i.e. isolated contrail over sea). No minimum optical thickness is required for the automatic tracking, yet a strong contrast with the background is desired. The behaviour does not show any typical pattern and depends strongly on the scene.
- An increase in thermal radiation is related to an increase in the optical thickness. The contribution of the warmer surface in the case of a less transparent contrail leads to a thermal irradiance value that is lower than in the case of a thick contrail where no information from the underlying, warm surface reaches the satellite. It has been seen than in the case of persistent contrails that become totally undistinguishable from the background, the longwave irradiance increases until 20 W/m^2 . This is typical of natural thin cirrus clouds, and remains constant with small time (age) independent variations.

- The reflected solar radiation approaches 0 as the contrail-cirrus becomes optically thinner, as expected. In cases where the background has a brightness comparable to that of the cloud, such as land or desert, the forcing in the SW range decreases strongly even when the contrail is very thick. Contrails cause a stronger forcing in the shortwave range over dark surfaces than over bright surfaces.

The results of the case studies will be applied to the statistical analysis (see Section 4.2) considering:

a) No distinction will be made between clear-sky and cloudy contrail scenes. It has been observed that the presence of a contrail can have different effects depending on its background. Contrails are often found in both situations, sometimes the same contrail can be isolated in some stages and subsequently mixed with surrounding cloudiness. Many contrails are also found in contrail clusters, where a number of contrails evolve simultaneously and affect one another. The presence of clouds that influence the development of the contrail cannot be detached from the study of the contrails themselves. Contrails in this study have been seldom found in a completely cloud free situation. The effect of the contrail in the atmosphere is highly dependent on the surrounding cloudiness. The aim of this work is to quantify the effect of contrails in the atmosphere, which is a combination of isolated contrails and contrails over cloudy areas. The consideration of the reference state of the atmosphere in this work accounts for the actual state of the atmosphere, favouring the consideration of the Earth's surface as reference but also accounting for the presence of other clouds, low or high, and not systematically neglecting all cirrus clouds. This leads to a better retrieval of the effect of contrails in the atmosphere.

b) Contrails over land and over ocean will be studied separately due to the different RF the same contrail causes over different backgrounds. Some of the contrails in this study drift by the wind from water to land or vice versa will also be considered separately. At a given moment, the radiative forcing caused by the contrail cover is a mixture of that caused by isolated contrails, contrails within other cirrus clouds, contrails over cloudy areas and over land or water simultaneously.

c) A separate day and nighttime study will be carried out due to the fact that only LW forcing contributes to the net forcing at nighttime whereas both LW and SW components contribute to the net forcing at daytime.

4.2 Systematic Studies

In this section it is desired to cover all seasons and make full use of the time period where rapid scans are available. These data have been disseminated on a regular basis only since June 2008. Four months of data have been chosen: August 2008, mid-October to mid-November 2008, January 2009 and April 2009. For each 5 minute timeslot and for the whole rapid scan area, LW and SW irradiances, the cirrus mask needed for the computation of LW, and the optical thickness have been pre-processed and stored. This translates into high computing time and high storage requirements.

Contrails being tracked by ACTA do not represent all the contrails that occur in the atmosphere but the wider ones with a higher contrast with the underlying surface.

The combination of the ACTA output -the contrail-cirrus mask- and the irradiance and optical thickness data mentioned above, will provide a general view of the typical life cycle of AIC and the evolution of their physical properties, especially the radiative forcing they induce. The physical properties that have been studied are: contrail geographical distribution, average lifetime, optical thickness and radiative forcing.

4.2.1 Geographical distribution

The contrails and contrail-cirrus detected by the CDA on MODIS and tracked by ACTA on SEVIRI/MSG are located in similar regions each month (see Fig. 4.10) although each month shows a different frequency (see Table 4.1). It has been assessed that some areas are more frequently covered by contrails, as seen in Fig. 4.11. These areas do not necessarily correspond to the areas with the heaviest air traffic because the formation of persistent contrails also depends on the conditions of the atmosphere, in particular on the location of the areas that are super-saturated with respect to ice. Although some regions with very low air traffic density have also a very low contrail occurrence (northern Africa, for example), the detected contrail cover of other heavily flown areas such as central Europe is not as high as expected. A very large amount of the contrails identified and tracked are located southwards from the north Atlantic flight corridor, drifted by the winds. It must be pointed out that the contrails and contrail-cirrus considered in this study constitute only a small fraction of the total of the contrail occurrence. Nevertheless, geographical distribution of contrails is similar to the persistent contrail coverage derived by Sausen et al. (1998), as shown in Figure 4.12. This persistent contrail coverage was obtained by combining the potential contrail coverage derived from ECMWF re-analysis data and a contrail parameterisation for the ECHAM¹ model with fuel consumption data.

¹Climate model developed by the Max Planck Institut for Meteorology from the ECMWF forecast model cycle 36 (EC) and a comprehensive parameterisation package developed at Hamburg (HAM)

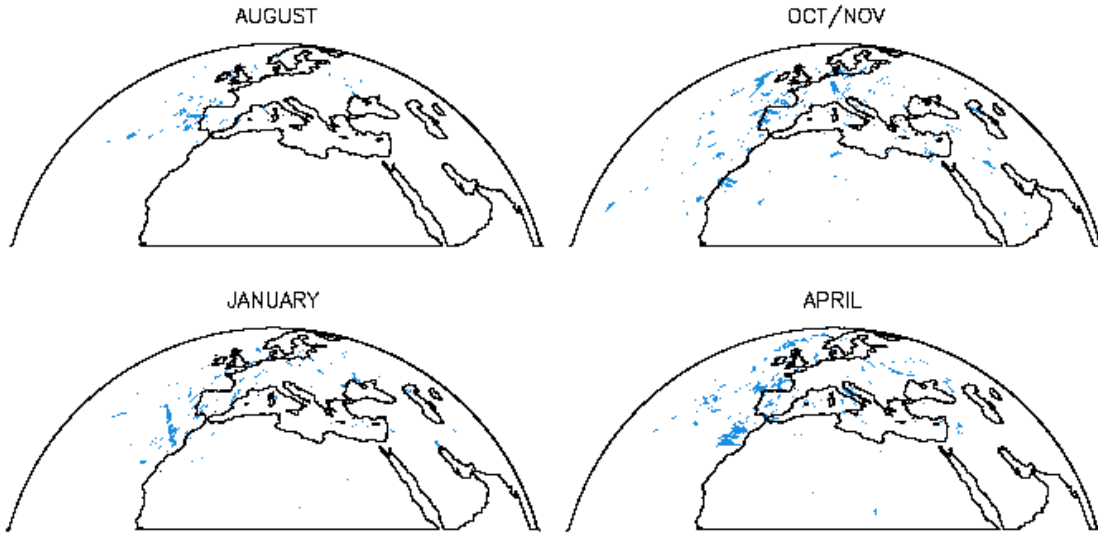


Figure 4.10: Four months of tracking. Geographical distribution of the studied contrails

Month	Frequency
August	14.8 %
Oct/Nov	32.8 %
January	17.4 %
April	35 %

Table 4.1: Frequency of the contrails tracked in % in each month

	Day	Night	Total
Water	40 %	19 %	59 %
Land	22 %	9 %	31 %
Mixed	6 %	4 %	10%
Total	68 %	32 %	

Table 4.2: Geographical distribution in % of the contrails tracked

Most of the contrails are found and tracked at daytime over water (40%) whereas only 9% are found and tracked over land at night. The daytime contrail tracking represents 68% of the total, which is in agreement with the air traffic pattern. As both the ACTA and the CDA algorithm work indistinctly on day and nighttime scenes because they are based only on infrared channels and brightness temperature differences, the distribution of the contrails and contrail - cirrus found is representative of the actual distribution. The day to night ratio is 2:1. Table 4.2 summarises the results.

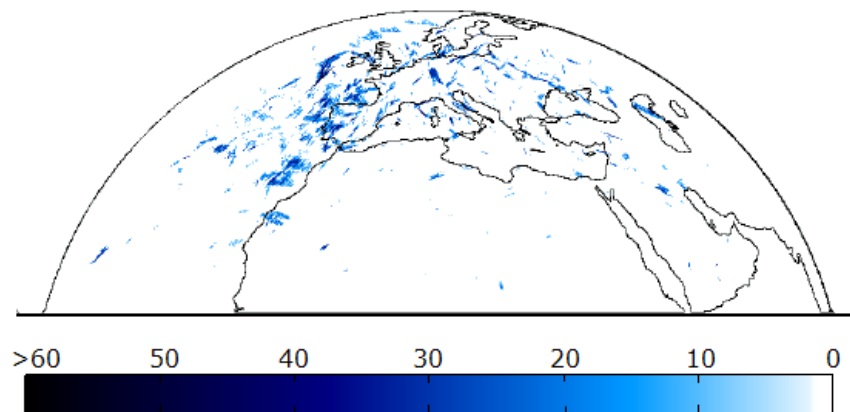


Figure 4.11: Frequency of occurrence of the studied contrails and geographical distribution

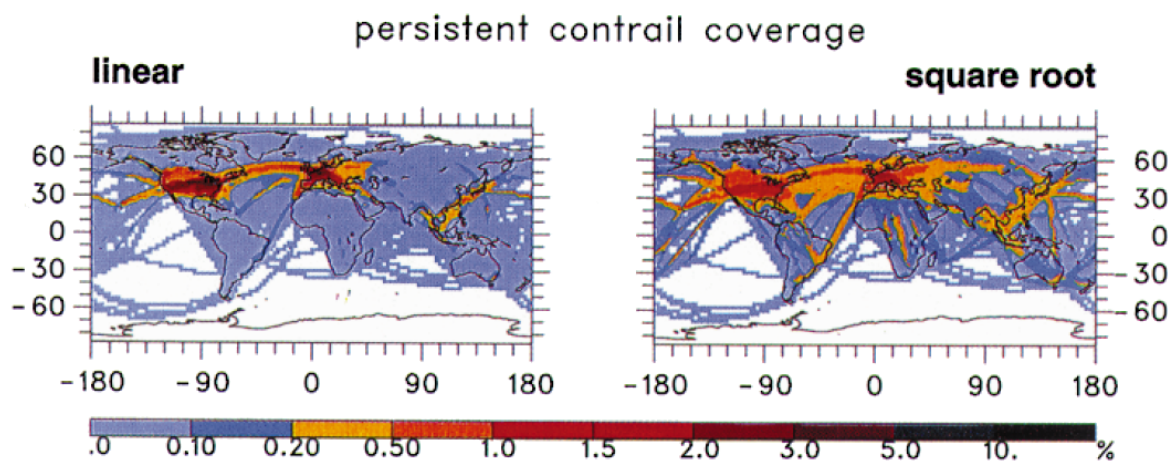


Figure 4.12: Annual mean contrail coverage % (mean of the years 1983 - 1993) as obtained for linear (left panel) and square root weighting (right panel) of the fuel consumption. The calibration produces a mean value of 0.5% for the region extending from 30°W to 30°E and from 35°N to 75°N for the 1992 worldwide aviation fleet. Source: Sausen et al. (1998).

4.2.2 Lifespan

The lifespans determined for the four seasons is shown in Fig. 4.13. Note that the results have been grouped in 30 minute steps, so each point in the histogram corresponds to the number of contrails whose lifetime is within each 30 minute bin (0-30 min, 30min-1h, etc.). As expected, contrail-cirrus with shorter lifetimes are more frequent than longer lived contrail-cirrus. The y-axis is logarithmical, it can be seen that the behaviour follows a decreasing exponential curve. The solid line depicted corresponds to an average lifetime of 51 minutes. The dotted and dashed lines correspond to e-folding times of 2 and 3 hours respectively. The distribution of life times suggests an e-folding time of 2-3 hours for those contrails surviving the first hour. In order to reach robust statistics on the life time, a larger data set of tracked contrails is necessary. The results are summarised in Table 4.3, where it can be seen that isolated cases can have lifetimes longer than 14 hours.

Month	mean Lifetime (minutes)	median (minutes)	range (min-max)
August	53 ± 7	25	5 - 285
Oct/Nov	42 ± 4	15	5 - 480
January	39 ± 4	15	5 - 410
April	71 ± 6	35	5 - 845
Total	51 ± 3	20	

Table 4.3: Lifespan results

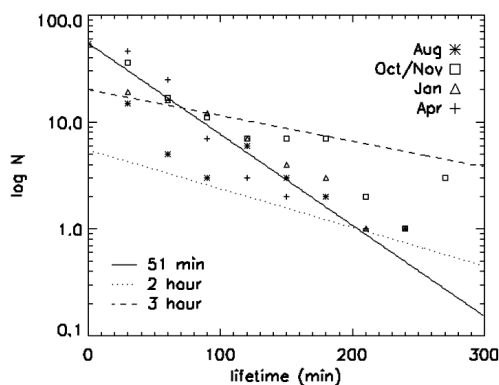


Figure 4.13: Life time of the contrails in all four months studied. Plotted lines correspond to $N = \exp(t/\lambda + c)$. Solid line: $\lambda = 51$ minutes, dashed line: $\lambda = 2$ hours, dotted line: $\lambda = 3$ hours

The actual lifetime of a contrail is longer than that shown here. There is a delay between the moment when the contrail is wide enough to be detected from the geostationary platform and the moment when ACTA sees it for the first time as it has been shown in the previous Section. This depends on the background, on the optical thickness of the contrail and on the its surroundings. In addition to this, there is a finite amount of time from the origin of the contrail until it is wide enough to be detected by the satellite sensor. These time lapses can add up to more than one hour (Duda et al., 2004).

4.2.3 Optical thickness

An average value of the optical depth for the whole lifetime is retrieved for each contrail-cirrus. A comparison between all months is shown in Fig. 4.14 and the combination in Fig. 4.15. All months present very similar distributions, although January presents larger optical depth values. The average optical thicknesses of the contrails here studied are displayed in Table 4.4 for each month. The mean value is nearly 0.9 and the optical thickness of individual contrails can be up to 3. Results are slightly larger than previous optical thickness studies (for instance, Atlas et al. (2006)), but lie within the expected range. These higher values can be attributed to two factors. On one hand, the CDA has been tuned to a very low false alarm rate to ensure that the input dataset for the ACTA algorithm only contains contrails, and the associated decrease of the detection efficiency constrains the CDA detection to optically thicker contrails. On the other hand, as this work considers all contrail and contrail-cirrus with their surroundings, the mixing of the contrail tracked with pre-existing cirrus clouds can lead to higher optical thickness values.

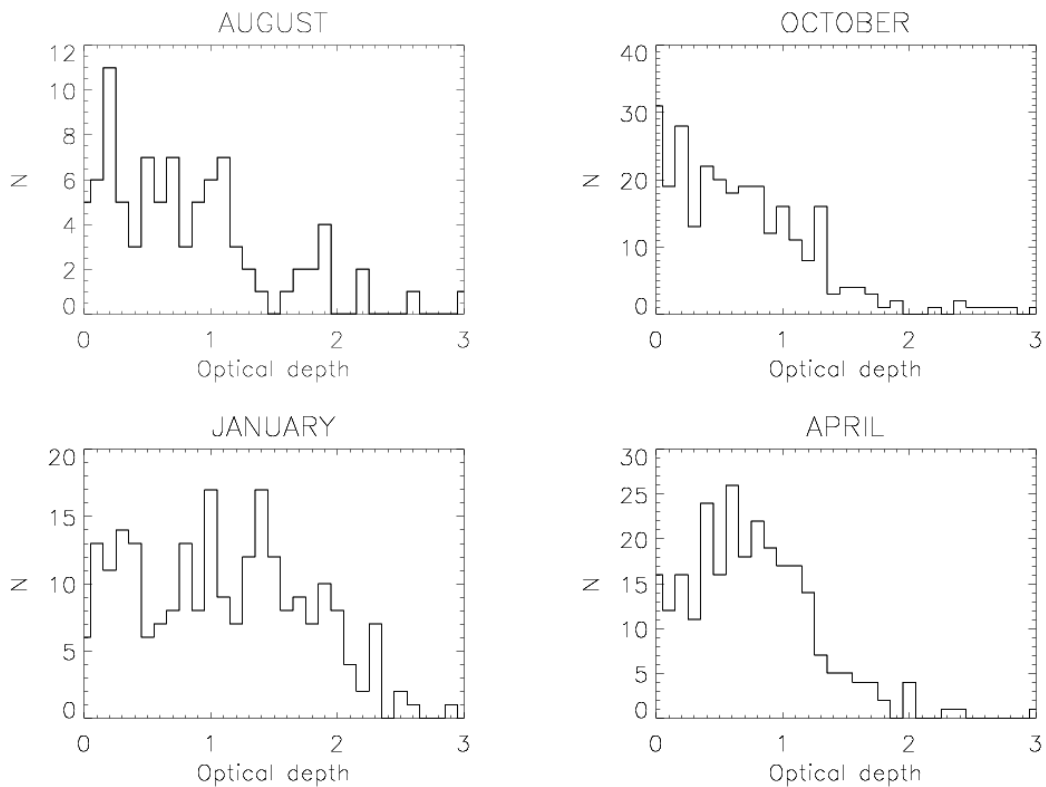


Figure 4.14: Optical thickness of each of the four months studied

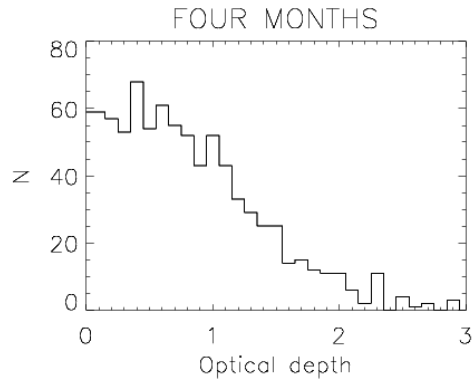


Figure 4.15: Optical thickness of each of all four months studied

Month	Optical thickness	median	range (min - max)
August	0.57 ± 0.04	0.51	0.04 - 1.92
Oct/Nov	0.73 ± 0.03	0.63	0.01 - 3.02
January	1.17 ± 0.05	1.14	0.01 - 3.10
April	0.82 ± 0.03	0.73	0.01 - 3.07
Total	0.859 ± 0.020	0.757	

Table 4.4: Optical thickness average results

4.2.4 Radiative Forcing

Table 4.5 presents the LW, SW and net RF results for each of the months studied, taking into account the time of the day and the background. The distribution of the results can be seen in Figure 4.16. To provide a better insight into the results, not only the arithmetical mean but also the median is presented. It can be seen in all cases that the median is normally notably closer to 0 than the mean value. The standard error is computed from the standard deviation. The radiative forcing values in the table include both the forcing produced by isolated contrails and the forcing produced by contrails within cloudy areas. The ratio isolated/cloudy of all contrails studied is 1:3, but this ratio is not constant throughout a day. At nighttime, most of the tracked contrails are isolated (74%), whereas only 45% of the contrails tracked in this study appear isolated at daytime. Therefore, it is expected that the forcing at nighttime be stronger than at daytime due to the effect of pre-existing surrounding cloudiness on the forcing. The reason for the different ratio at day and nighttime remains unknown and may be related to the different air traffic pattern throughout the day.

			Daytime RF (W/m ²)		Nighttime RF (W/m ²)	
			Water	Land	Water	Land
August	LW	mean	17.7	7.2	30.2	20.2
		median	14.2	4.4	23.5	16.3
		stderr	± 0.5	± 0.5	± 1.0	± 0.8
	SW	mean	-41.4	-28.27	0	0
		median	-31.1	-24.8	0	0
		stderr	± 1.2	± 1.0	0	0
	NET	mean	-23.7	-21.1	30.2	20.2
		median	-12.7	-19.7	23.5	16.3
		stderr	± 1.1	± 1.1	± 1.1	± 0.8
Oct/Nov	LW	mean	18.6	18.4	24.4	25.8
		median	17.2	18.6	24.5	22.1
		stderr	± 0.3	± 0.3	± 0.3	± 0.8
	SW	mean	-35.9	-28.5	0	0
		median	-33.2	-23.0	0	0
		stderr	± 0.7	± 0.7	0	0
	NET	mean	-17.2	-10.1	24.4	25.8
		median	-12.5	-6.4	24.5	22.1
		stderr	± 0.6	± 0.6	± 0.3	± 0.8
January	LW	mean	15.5	14.2	18.6	18.5
		median	13.3	10.6	18.2	18.2
		stderr	± 0.4	± 0.7	± 0.5	± 0.5
	SW	mean	-32.5	-34.5	0	0
		median	-26.4	-29.8	0	0
		stderr	± 0.9	± 1.6	0	0
	NET	mean	-17.0	-20.3	18.6	18.5
		median	-11.4	-14.7	18.2	18.2
		stderr	± 0.9	± 1.3	± 0.5	± 0.5
April	LW	mean	14.11	17.5	20.8	24.4
		median	12.73	14.7	19.2	22.4
		stderr	± 0.21	± 0.5	± 0.4	± 0.9
	SW	mean	-36.4	-28.8	0	0
		median	-28.2	-24.5	0	0
		stderr	± 0.7	± 0.7	0	0
	NET	mean	-22.3	-11.3	20.8	24.4
		median	-13.7	-9.0	19.2	22.4
		stderr	± 0.7	± 0.6	± 0.4	± 0.9

Table 4.5: Results: radiative forcing at top of atmosphere of the contrails tracked by ACTA. Mean, median and standard error.

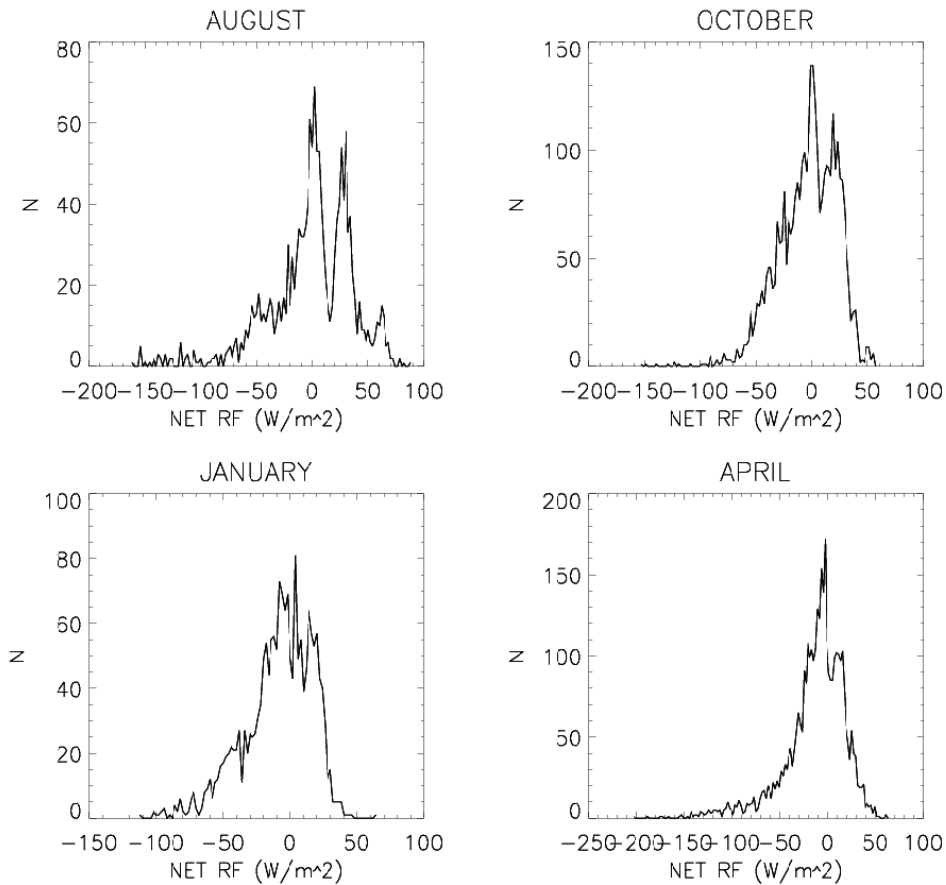


Figure 4.16: Histograms of the net radiative forcing (W/m^2) of the four months studied.

Contrails that drift from land to water or vice versa throughout their lifetime are not taken into account in this study because it is not possible to assess if the process used in this work provides a reliable result when accounting for the reference state of the atmosphere. These mixed scenes represent only 10% of the total (see Table 4.2), the 90 % of remaining cases being representative enough for the study. The reference state retrieval will favour pixels over sea at daytime because of their lower reflectance and land pixels at nighttime because of their higher temperature, regardless of where the larger part of the contrail / contrail-cirrus is located.

Table 4.6 presents a summary of the results considering the effects on day/night or land/water. These radiative forcings correspond to a 100% contrail and contrail-cirrus coverage. As expected, the difference between RF over land or over water at nighttime is not relevant because the forcing only contains the LW contribution, which is less dependent on the underlying surface than the SW forcing. At daytime, however, the SW forcing plays a strong role and a difference can be seen between both surfaces. The reason why the RF over water is stronger than over land is that the sea surface reflects less radiation back to space than the land surface. It must be kept in mind that the scenes do not only correspond to isolated contrail-cirrus but also to contrail-cirrus in cloudy scenes. On average, the contrails / contrail-cirrus studied have a cooling effect at daytime and a warming effect at nighttime and the balance throughout a day is mostly positive in mid-latitude regions.

	Day	Night
Water	-20.5 ± 0.4	23.2 ± 0.2
Land	-13.2 ± 0.4	22.3 ± 0.4

Table 4.6: Net radiative forcing results in W/m^2 corresponding to a sky 100% contrail / contrail-cirrus covered

Month	Net radiative forcing (W/m^2)
August	-0.8 ± 0.5
Oct/Nov	3.08 ± 0.21
January	6.70 ± 0.23
April	2.8 ± 0.3
Total	5.9 ± 0.6

Table 4.7: Net radiative forcing for the four months considered, in W/m^2 . The forcing corresponds to a sky 100% covered by contrail-cirrus. Uncertainties are issued from the standard errors

Table 4.7 presents the average forcings for each month. In order to account for the different hours of sunlight in each month at each latitude, the daytime fraction for three latitude bands [15°N - 35°N , 35°N - 55°N , 55°N - 70°N] has been considered and combined with the forcing produced by the contrails in each band. It can be seen that the net radiative forcing each month is different. This is due to the fact that some months have a larger daytime fraction than the rest. The stronger positive radiative forcing effects are found in January as this is the month with fewer hours of sun. The total effect presented is the average of all contrails tracked in this work, which does not correspond to the sum of all monthly contributions because the different months have a different frequency of contrail/contrail-cirrus coverage.

The behaviour between optical thickness and forcing is shown in Figure 4.17 top and bottom. The high scattering in the plots shows the high variability existing in the effect of the radiative forcing of contrails. Not only the radiative forcing is dependent on the optical thickness, but also other factors may play a role such as the surrounding cloudiness and the background albedo. However, it can be seen that higher optical thicknesses lead to stronger forcings in both the LW and SW ranges, and that the net forcing also is stronger in the case of optically thicker contrails.

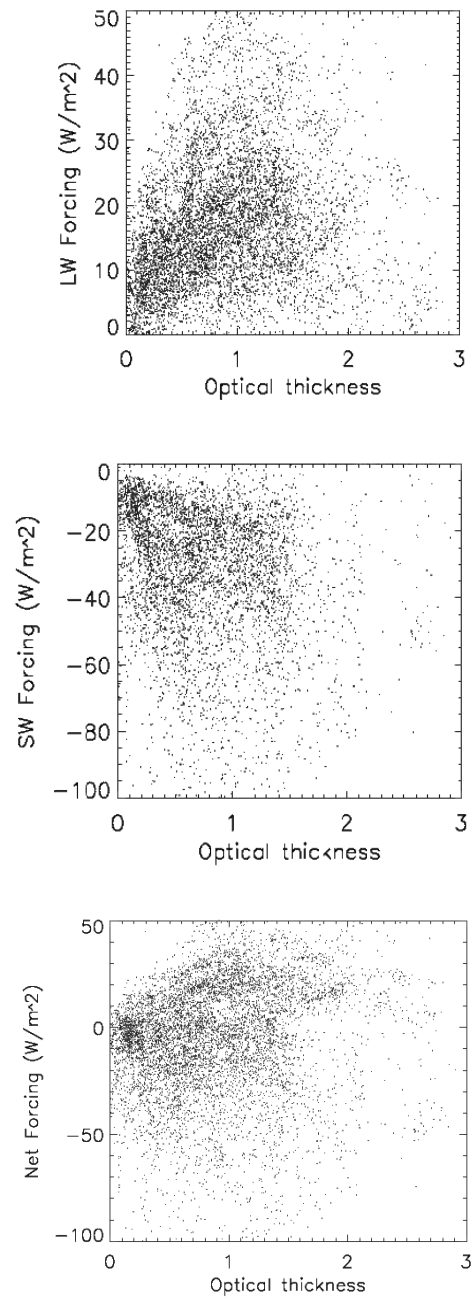


Figure 4.17: Net radiative forcing in W/m^2 vs. optical thickness for all the contrails studied. Top: LW, centre: SW, bottom: Net Forcing

Chapter 5

Conclusions and outlook

An automatic contrail tracking algorithm (ACTA) that takes advantage of the high temporal resolution of SEVIRI infrared channels has been developed. It is based on the brightness temperature difference 10.8-12.0 μm and works on the 5-minute rapid-scan service of MSG. As it is based on information derived from an infrared channel, it functions equally on day and nighttime scenes. The input data used in this work has been provided by a contrail detection algorithm (CDA) that detects contrails in a spatial resolution of 1 km MODIS radiances. However, it should be pointed out that the algorithm developed (ACTA) is designed to receive inputs from either automatic retrievals such as CDA or from a human researcher. A very important characteristic of ACTA is that it can track the whole lifetime of the contrail regardless of the input time. The CDA-provided input can be at any stage of the development of the contrail and ACTA will use this input and track the contrail in negative (to the past) and positive (to the future) time increments until it cannot distinguish it anymore from the background or from the surrounding cloudiness. Thanks to the information provided by ACTA, contrail-cirrus can be labeled as man-made even when they are undistinguishable from their natural counterparts. Thus, these structures can be included automatically for the first time in the computation of the effects of aviation induced cloudiness on the Earth-atmosphere system. Moreover, ACTA's rapid functioning allows the automatic tracking of very large amounts of input contrails, providing results with high statistical significance.

ACTA's tracked contrails in this work are inevitably associated with the contrails provided as input, which represent only part of the contrails that occur in the atmosphere. For the sake of a very accurate input dataset (a low false alarm rate of the contrail detection algorithm), the CDA has constrained its results to the easily identifiable contrails. Despite this, the remaining number of contrails, nearly a thousand, is high enough to provide for the first time a thorough study of a very large dataset on the characteristics of contrails and their evolution to contrail-cirrus from a satellite-borne point of view. This analysis has two limitations: on one hand, due to the nature of the retrieval, contrails whose width is substantially lower than the spatial resolution of the sensor cannot be considered. On the other hand, the accuracy of the results has a high priority for ACTA and dubious cases are purposely neglected. The ACTA results constitute a unique collection of contrails and their development with very high temporal accuracy.

Four months' worth of contrails and contrail-cirrus have been studied. The location of the

contrails has similarities with the persistent contrail cover (Sausen et al., 1998) that can be determined using air traffic data and model information of the state of the atmosphere. The coverage at daytime is twice as large as at nighttime. ACTA does not rely on visible radiances and works independent of the time of the day, so these findings are representative of the actual distribution of contrail cover.

The contrail occurrence in spring and autumn is found to be larger than in summer or winter. Meyer et al. (2002) found a similar behaviour when studying the cover of linear-shaped contrails over central Europe (0.7% cover in spring vs. 0.3% cover in summer). The day to night ratio of contrail occurrence is 2:1, as expected, due to the fact that most air traffic takes place during daytime and only part of the transatlantic flights over the north Atlantic flight corridor occur at nighttime. This coverage does not only represent the coverage of the input contrails during their linear phase but also in the final stages, where no automatic detection method can identify them because they lack the linear shape.

This is the first time that the lifetime of a very large number of contrails and contrail-cirrus has been studied, so that an average lifetime of contrails can be derived. Until now, only case studies had been carried out, usually coincident with measurement campaigns (see Duda et al. (1998)). In addition to the retrieved mean lifetime it is necessary to add the time between the formation of the contrail and the first detection from a satellite instrument. To date, there is no accurate estimate of this time lapse available, although some authors consider it to be up to 1 hour through case study analyses for a sensor of similar spatial resolution as SEVIRI (Duda et al., 2004) or 33 minutes for MODIS 250m imagery (Atlas et al., 2006). It has been seen that most contrails have very short lifetimes, but in this study some cases have been seen to last up to 14 hours. The mean observable lifetime retrieved is 51 ± 3 minutes, affected by the very short lived contrails, but the distribution of the contrails having lifetimes longer than one hour presents e-folding times of two to three hours.

The retrieval of the optical thickness has been based on a neural network trained on a dataset containing 10,000 simulated realisations of the state of the atmosphere. The advantage of this algorithm is that it is based on IR channels, providing optical depth also at nighttime. The mean optical thickness retrieved for the contrails in this study is 0.9 with a standard deviation of 0.6. Four months of data have shown mean optical thicknesses between 0.57 and 1.18. Meyer et al. (2002) estimated from satellite measurements a mean effective optical thickness of linear contrails over west Europe of 0.11, and Minnis et al. (2004) derived an optical thickness of 0.2 over the USA, but these results cannot be applied to contrail-cirrus because optical thickness increases with aging of the contrail (Atlas et al., 2006). The results obtained are higher than in previous works because the input dataset contains typically optically thicker (and therefore better detectable) contrails and it also accounts for the contrails that merge into pre-existing cirrus, with a higher optical thickness.

The radiative forcing, RF, has been assessed by means of two algorithms based on combinations of the SEVIRI sensor channels. The outgoing irradiances and the radiances of the SEVIRI channels at the top of the atmosphere have been modeled using the `libRadtran` package. The retrieval of the longwave irradiance is based on multilinear parameterisation and the retrieval of the shortwave irradiance is based on a fit by a neural network. Both algorithms have been thoroughly validated in this work with widely accepted instruments such as CERES (on board of Terra) and GERB (on board of MSG) with very good results.

To compute the RF, knowledge of the background state of the atmosphere is needed. To do this, Palikonda et al. (2001) use neighbouring pixels located at a fixed distance from the contrail pixels and eliminate all the cirrus-covered pixels among them (even natural cirrus), and Meyer et al. (2002) measure the brightness temperatures of the pixels nearby to establish the contrail boundary and then consider the remaining pixels, which can lead to the consideration of other contrails as reference state of the atmosphere. In this work, the background state of the atmosphere has been assessed considering the pixels in the surroundings that are darker (at daytime) or warmer (at nighttime). This method has the advantage of being closer to the actual reference state. It neither eliminates all cirrus clouds in the scene nor does it consider all the surrounding pixels without discrimination. If the scene is covered by a significant amount of other clouds (even cirrus clouds) -a very common situation-, these clouds will also be taken into account, although cloud-free pixels will be favoured to diminish the influence of contrail pixels.

The mean radiative forcing has been shown to be dependent on the month considered. In all cases, the SW has outweighed the LW forcing at daytime causing a cooling and the net forcing has been positive at nighttime causing a warming due to the SW forcing not being present at night. Through case studies and through a separate study of the effect of contrails over land/water and at day/nighttime, the effects have been proven to be highly affected by surrounding clouds and by the albedo and temperature of the background. The net effect has been assessed considering the different daylight hours in each month leading thus to a smaller forcing in summer than in winter. The mean net radiative forcing of all the contrails tracked in this work is 6 W/m^2 (for a 100% contrail-cirrus covered sky) and due to the very high variability of the data, the standard deviation is as high as 18 W/m^2 . Even though the CDA-provided input dataset for ACTA slightly biases the tracked contrails towards the easily detectable, it is the first time that the effect of such a large number of contrails have been studied. This work has considered not only the linear contrails but also those that would not have been otherwise considered as anthropogenic. The value of the radiative forcing includes the effect of the contrail-cirrus-covered regions considering the natural surrounding, which includes the effect of other clouds, leading to a smaller radiative forcing than in the case of isolated contrails. Sub-visible contrails or thinner contrails not seen from a satellite platform are not represented in this value. Wider and optically thicker contrails are well represented due to the large amount of data handled, which also accounts for the RF of contrails surrounded by other cloud structures.

Previous works based on remote sensing techniques establish net radiative forcings for 100% contrail cover of 4.4 to 8.9 W/m^2 for contrails over Central Europe (Meyer et al., 2002) or 8 W/m^2 for a 30 minute old contrail (Duda et al., 1998). Model-derived studies show larger results such as the 23.9 W/m^2 derived for clear sky over a continental mid-latitude summer atmosphere by Stuber and Forster (2007) or 29.5 W/m^2 by Meerkötter et al. (1999). The results in this work are in good agreement with previous satellite-derived findings, but they are lower than model radiative forcing results. The findings in this work show in average a LW forcing of 19.3 W/m^2 . These results are in agreement with the results of Palikonda et al. (2002). They derived LW forcing from MODIS and AVHRR data and retrieved values between 12 and 27 W/m^2 . Model results (Meerkötter et al., 1999; Stuber and Forster, 2007) consider that the mean LW forcing easily reaches 40 or 50 W/m^2 over a cloud-free continental mid-latitude summer atmosphere. The mean SW forcing in daily average in this

work is -15.89 W/m^2 , not as strong as in model findings (-22 W/m^2 according to Meerköetter et al. (1999) and -20.3 W/m^2 according to Stuber and Forster (2007)). The causes of the disagreement between remote sensing methods and models when deriving radiative forcing are twofold. On one hand, sensitivity studies on model results show that the LW computation strongly varies with small variations of optical thickness and effective radii (Meerköetter et al., 1999). On the other hand, the presence of surrounding cloudiness (not considered in models) alters the RF results. The LW forcing caused by a contrail surrounded by natural clouds is lower than the one produced by a contrail of the same characteristics isolated over the warm Earth surface. This effect is smaller in the SW range due to the fact that the SW irradiance of land surfaces is some times closer to that of thin clouds. This large decrease of the LW forcing and small decrease of the SW forcing due to surrounding cloudiness lead to satellite-derived net RF values smaller than expected by models.

Outlook

Meteosat-8 Rapid scan data have only been disseminated on a regular basis since June 2008. Running ACTA on several years of data will produce more robust results. The radiative forcing has been shown to be extremely dependent on the temperature and albedo of the background (altered by the presence of cloudiness), so three years of data would account for all possible situations and will provide an estimate of the climatic effect of aviation induced cloudiness. A larger array of input contrails can be obtained running the CDA not only on MODIS but also on other polar orbiting platforms. ACTA is also designed to receive a *human* input that can be made coincident with campaigns or case studies.

The accuracy of the results would increase if ACTA were modified so that the detection covered more stages of the tracking. ACTA's performance has been limited in some cases by the presence of other clouds in such a way that the tracking has stopped to avoid the tracking of a wrong structure. Therefore, the inclusion of a test retaining information of the shape of the contrail that is accurate enough to identify the contrail despite its constant changes in the shape could increase the accuracy of the results.

The combination of ACTA results with air traffic data can fill the time lapse gap between the moment where an aircraft produces a contrail and the moment it is first seen from the satellite instrument. Furthermore, a more accurate lifetime retrieval will lead to more accurate mean RF and mean optical thickness values.

ACTA's results also contain information about the direction and speed of the wind at the height of the contrail in time intervals of 5 minutes, increasing the information about the windfield.

ACTA's results could be combined with products such as particle size from other satellite instruments, but in order to provide a better insight on the development of contrails, it would be interesting to take advantage of SEVIRI's high temporal and spatial resolution over the Rapid-Scan area and develop SEVIRI-based algorithms to derive measurements of other physical properties of the contrail such as particle size and ice water content. A large collection of ACTA's tracked contrails could also be helpful to develop more accurate cirrus masks.

As ACTA can track a very large number of contrails, maps depicting the occurrence of that large number of contrails and contrail-cirrus constitute a useful tool for regional studies on the areas where air traffic has a larger impact, which are not necessarily coincident with the areas where the air traffic density is larger.

Appendix A

Contrail tracking. Example

A step-by-step sample of the functioning of ACTA is shown here. This contrail corresponds to the 5th April 2009, was located over the bay of Biscay and lasted 6 hours and 30 minutes. The yellow line encloses the pixels identified as contrail. Note that the vicinity of other contrails parallel to the tracked one does not affect the tracking and that crossing over a pre-existing contrail or the presence of underlying cloudiness does not lead to a misidentification of the original contrail. Besides, after two hours the contrail is no longer recognisable as such had it not been for its previous history. The input provided by the CDA corresponds to the 1135 timeslot and is marked with a blue frame. The temporal resolution is 5 minutes.

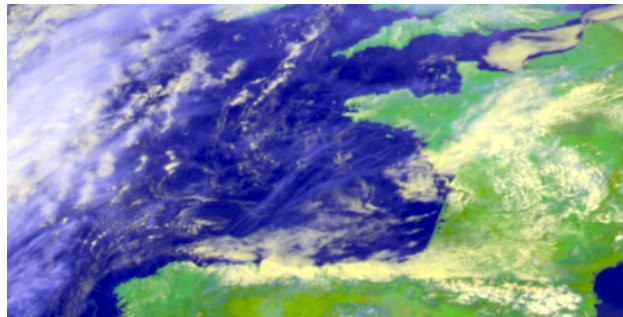


Figure A.1: False color RGB composite of the scene in the moment when CDA provides the input, 1135 UTC

It can be seen that the tracking always identifies the same contrail. The relationship between slope and intercept show a very smooth change (see Figure A.3) and the area covered by the contrail does neither show any blank spaces nor a behaviour against the wind field (see Figure A.2).

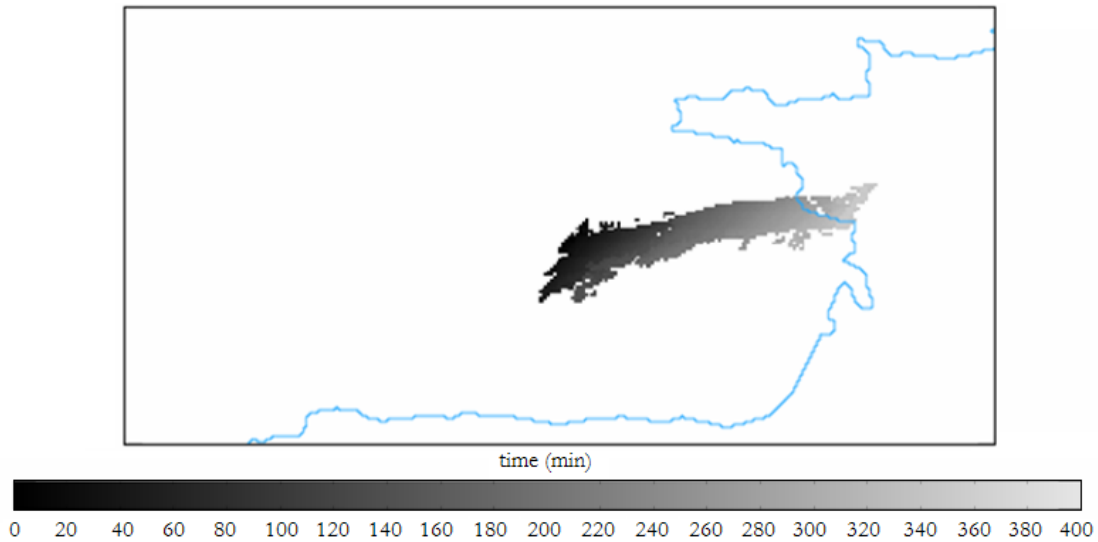


Figure A.2: Area covered by the contrail during the tracking. The colours indicate the age of the contrail

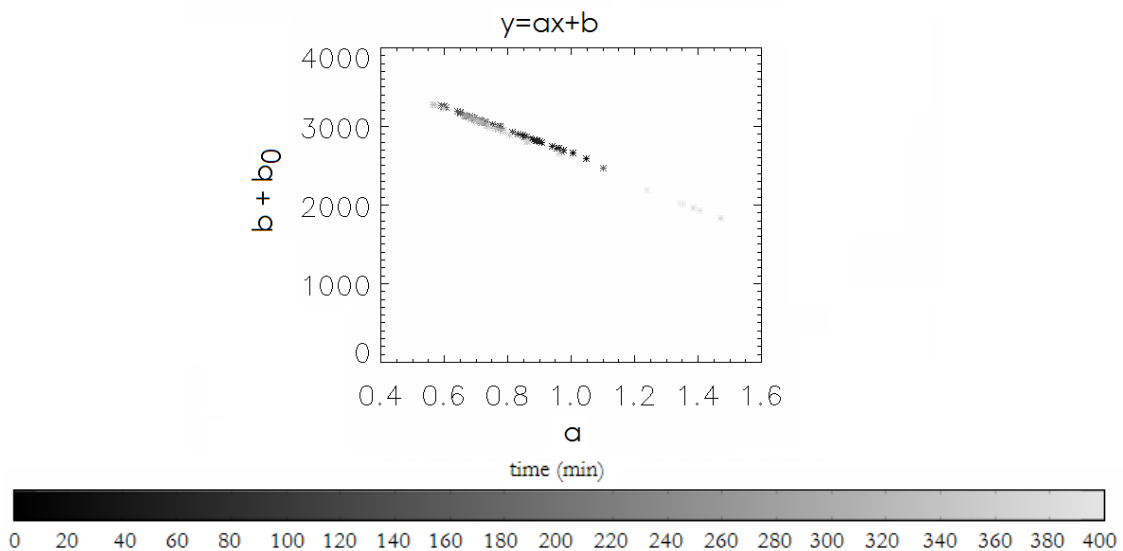
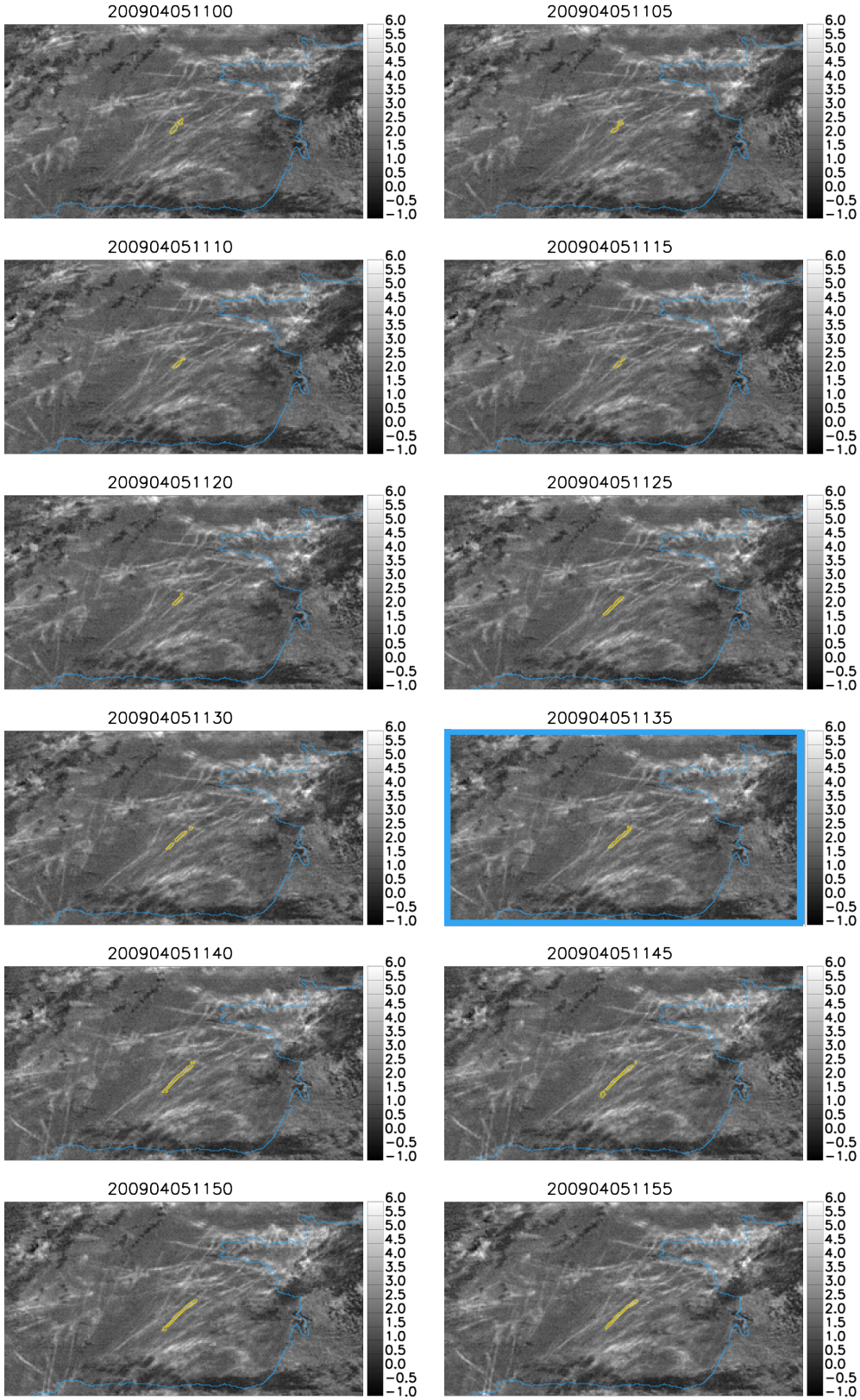
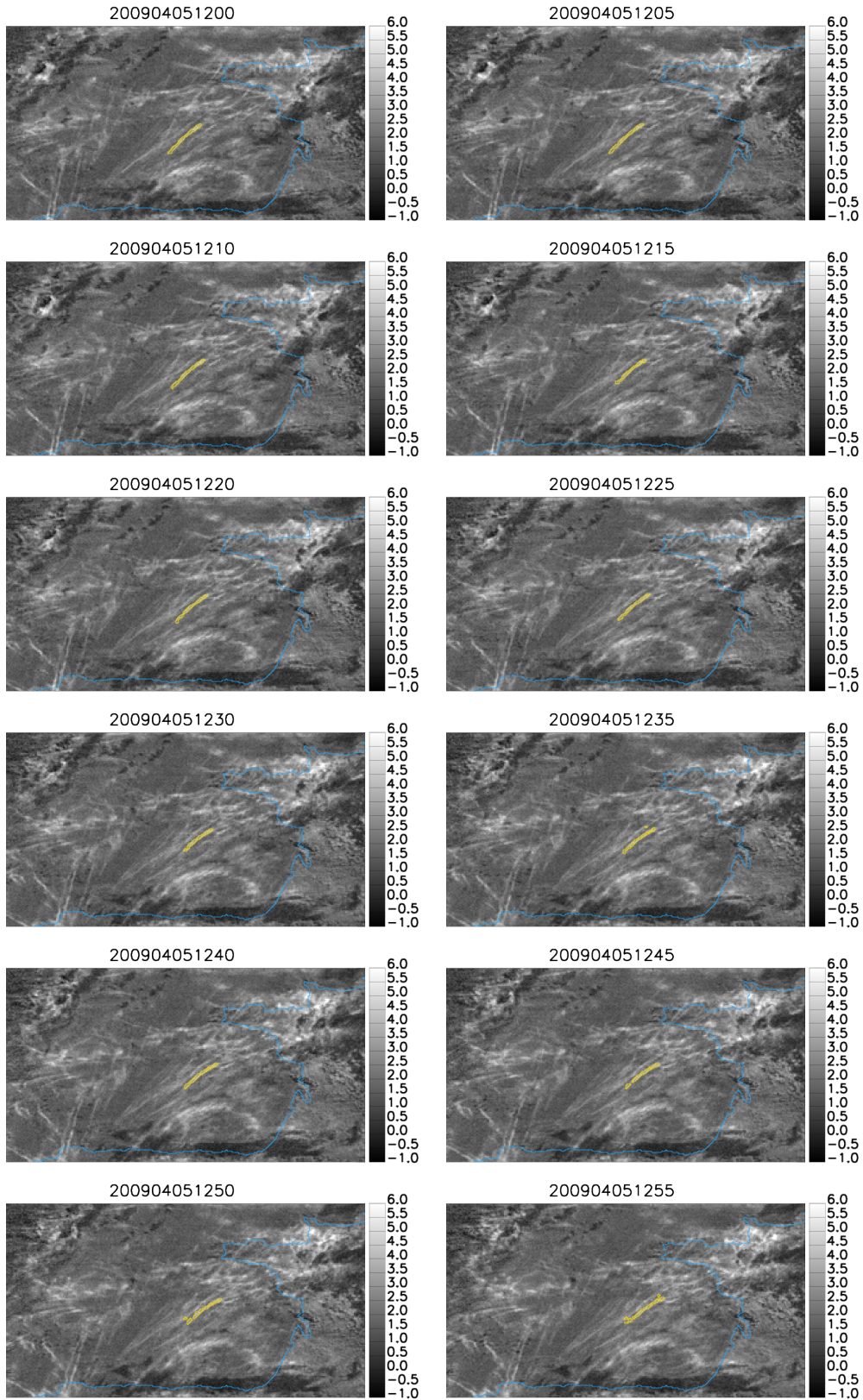
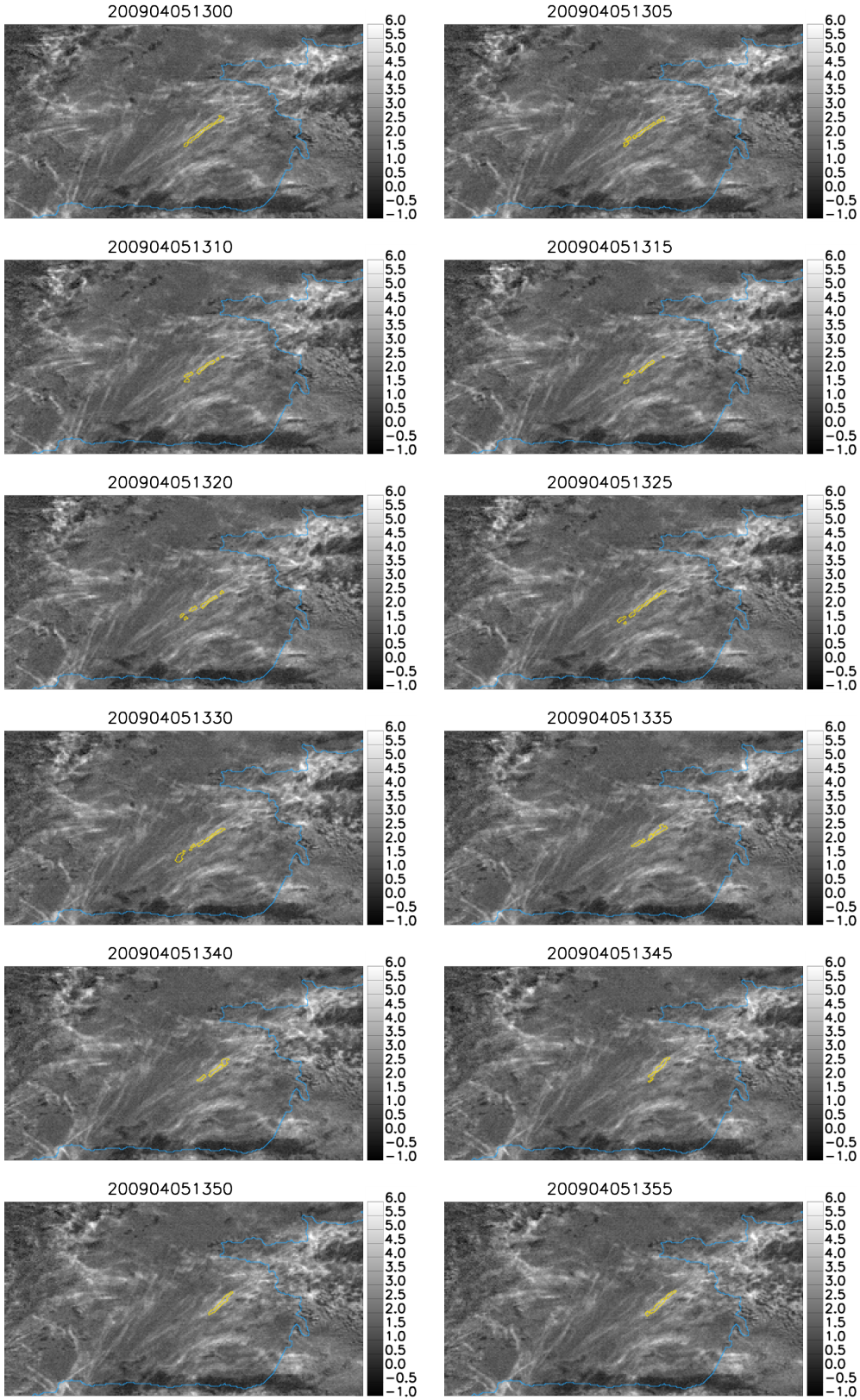
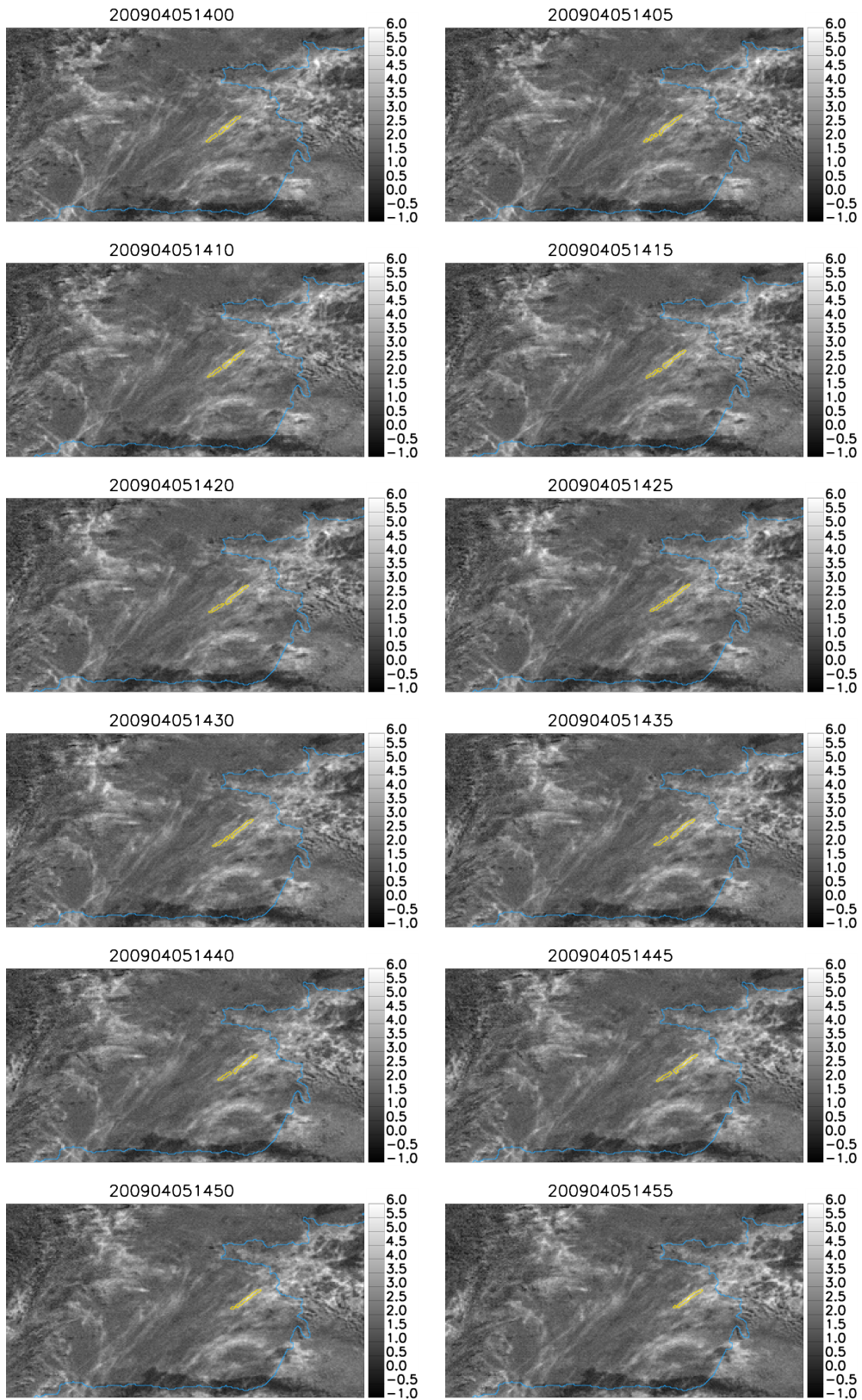


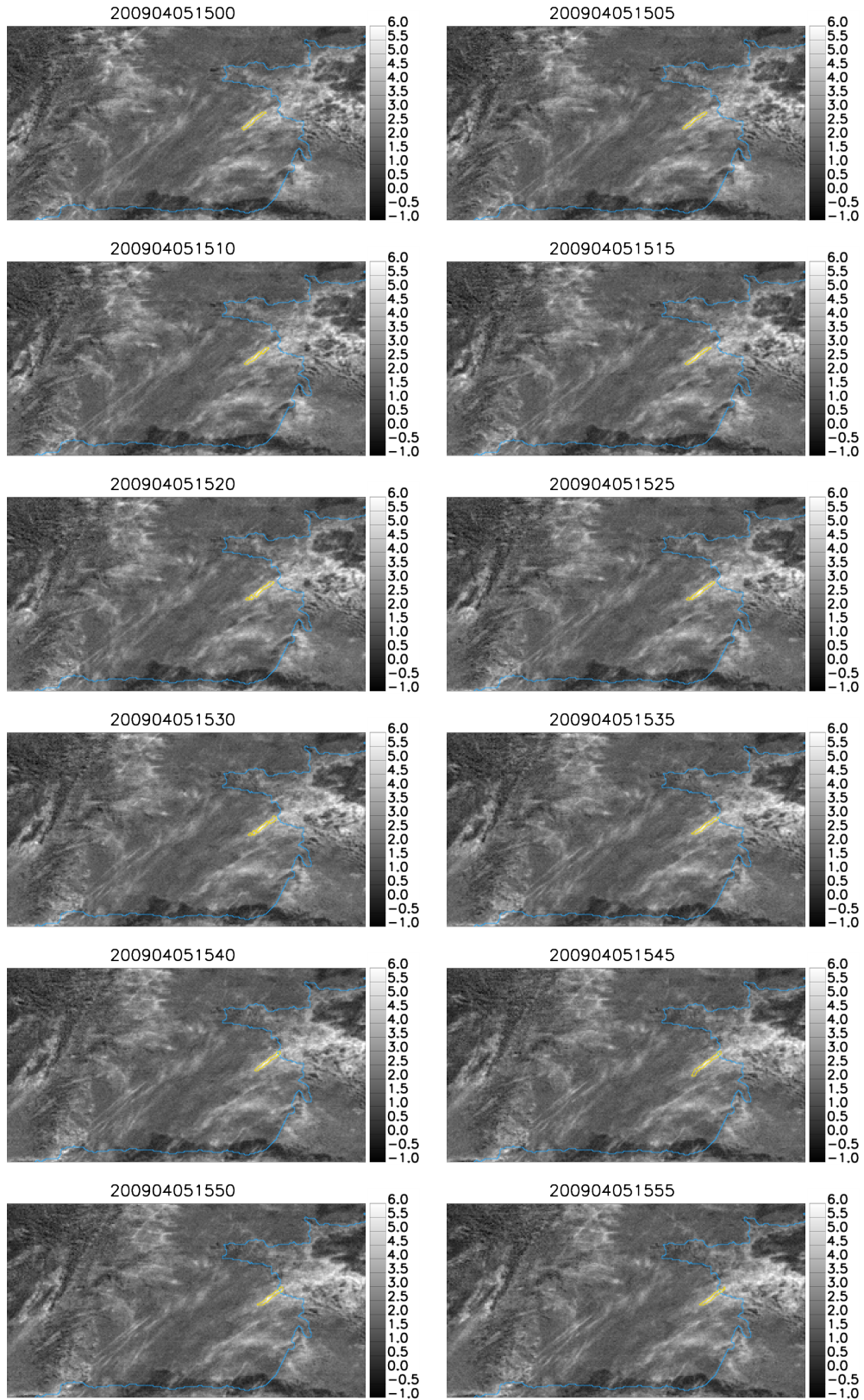
Figure A.3: Slope (a) and intercept (b) of the line defining the contrail ($y=ax+b$) in each moment of its development. The colours indicate the age of the contrail

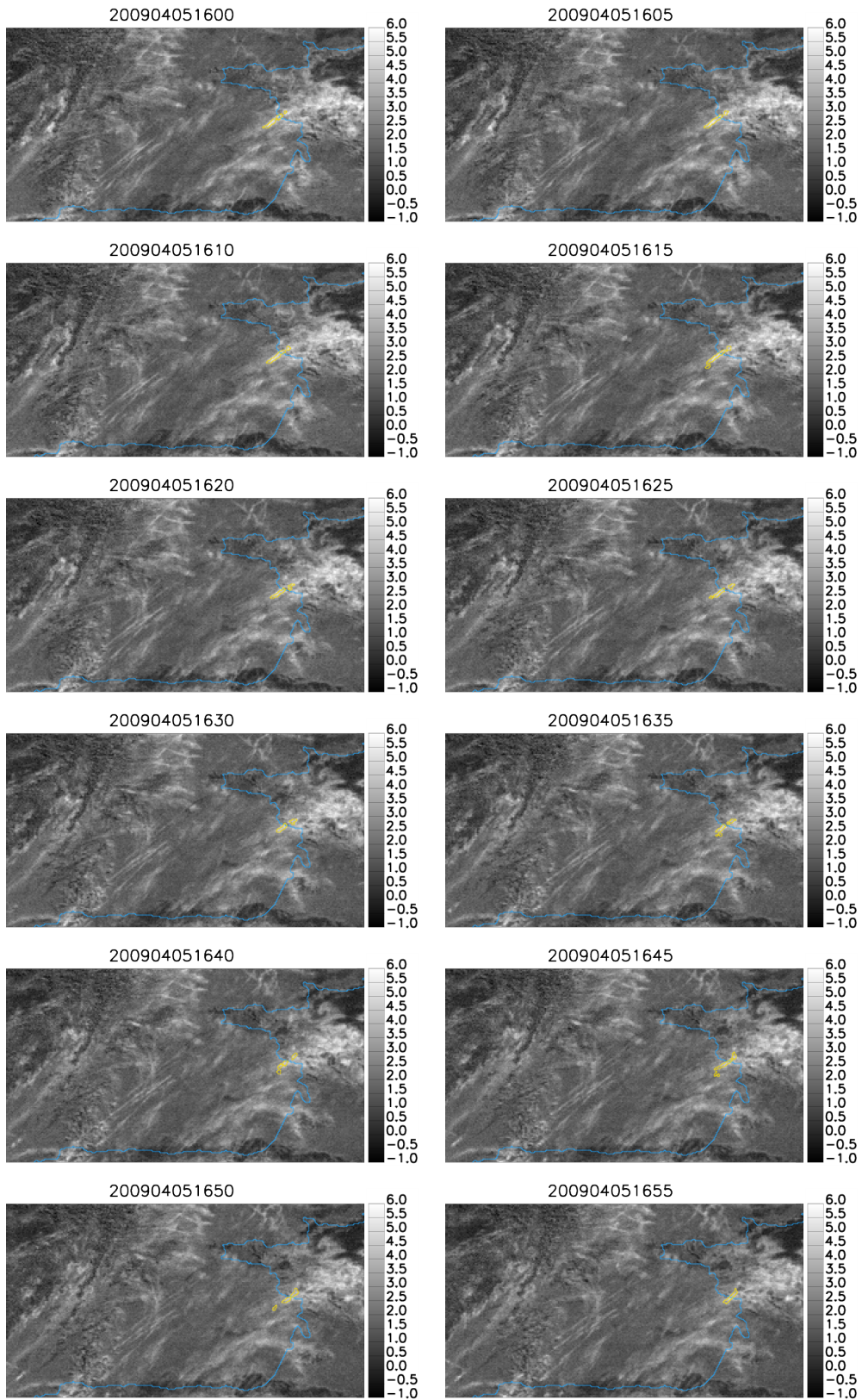












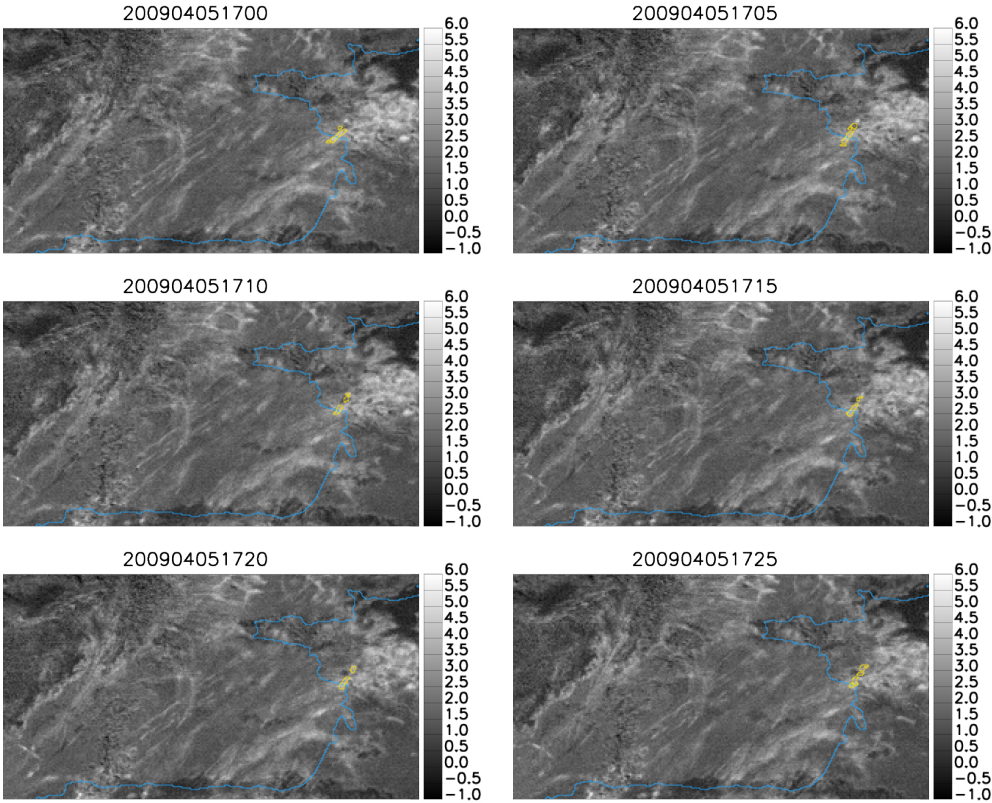


Figure A.4: Example of the functioning of ACTA. 5/April/09 from 1100 UTC to 1735 UTC. Yellow: contrail tracked. Background: brightness temperature image 10.8 μm - 12.0 μm

Appendix B

Validation of irradiances: CERES/Terra vs. SEVIRI/MSG

Linear fits of CERES irradiance data vs. the irradiance computed by the algorithms based on MSG/SEVIRI channels. Unless otherwise specified, each pair of plots correspond to the same scene. LW (W/m^2) on the left, SW (W/m^2) on the right. Fit equation is displayed on each plot and corresponds to the solid line; dashed line $y = x$ only for reference. The missing data in some of the shortwave cases are due to the time of the day (reflected solar irradiance is zero at nighttime). Tables B.1 and B.2 show the slope, correlation coefficient, average irradiance, root mean square and bias of each of the fits.

Instrument		Longwave		Shortwave	
MSG/SEVIRI	Terra/CERES	Slope	R^2	Slope	R^2
01/02/04 08:30	08:23 - 08:38	0.94	95.24	0.97	94.60
02/02/04 02:15	02:07 - 02:23	0.93	97.05	-	-
24/03/04 08:00	08:00 - 08:13	0.96	97.13	0.83	94.52
08/04/04 07:30	07:14 - 07:29	0.98	97.10	0.85	95.52
14/06/04 11:15	11:01 - 11:18	1.00	97.76	0.81	97.16
01/07/04 08:30	08:16 - 08:35	0.99	94.53	0.76	87.87
08/07/04 12:00	12:00 - 12:08	0.99	98.93	0.82	97.83
13/08/04 14:45	14:39 - 14:59	0.81	88.18	0.82	94.10
02/09/04 12:45	12:38 - 12:57	0.94	96.73	0.84	92.49
15/10/04 18:45	18:35 - 18:59	0.90	94.11	-	-
10/11/04 21:00	20:50 - 20:59	0.95	88.48	-	-
22/12/04 02:15	02:07 - 02:23	1.00	96.40	-	-

Table B.1: Results of the comparisons between Terra/CERES and SEVIRI/MSG irradiances. Slope and correlation coefficient

Instrument		Longwave			Shortwave		
MSG/SEVIRI	Terra/CERES	Mean (W/m ²)	RMS (W/m ²)	Bias (W/m ²)	Mean (W/m ²)	RMS (W/m ²)	Bias (W/m ²)
01/02/04 08:30	08:23 - 08:38	230.18	10.09	2.02	239.87	48.83	-21.07
02/02/04 02:15	02:07 - 02:23	238.64	9.75	-1.53	-	-	-
24/03/04 08:00	08:00 - 08:13	236.34	11.85	4.02	274.06	42.02	-17.66
08/04/04 07:30	07:14 - 07:29	268.54	9.41	4.88	263.43	36.56	-7.16
14/06/04 11:15	11:01 - 11:18	270.99	9.69	0.66	324.70	62.35	-37.20
01/07/04 08:30	08:16 - 08:35	291.13	11.22	3.15	234.74	33.10	-21.16
08/07/04 12:00	12:00 - 12:08	282.48	6.67	-4.62	224.87	43.24	-15.67
13/08/04 14:45	14:39 - 14:59	249.84	18.99	-3.60	246.90	69.70	-13.35
02/09/04 12:45	12:38 - 12:57	251.11	10.43	-4.25	241.13	51.23	-22.47
15/10/04 18:45	18:35 - 18:59	230.00	12.31	3.82	-	-	-
10/11/04 21:00	20:50 - 20:59	254.57	9.59	2.17	-	-	-
22/12/04 02:15	02:07 - 02:23	252.97	11.78	0.84	-	-	-

Table B.2: Results of the comparisons between Terra/CERES and SEVIRI/MSG irradiances. Mean irradiance, root mean square (RMS) and bias

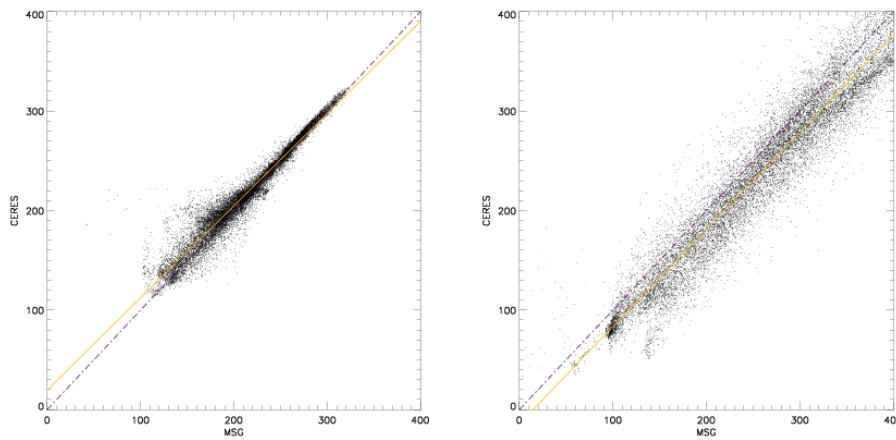


Figure B.1: 1/Feb/2004, 0830 UTC. Left: LW, Right: SW

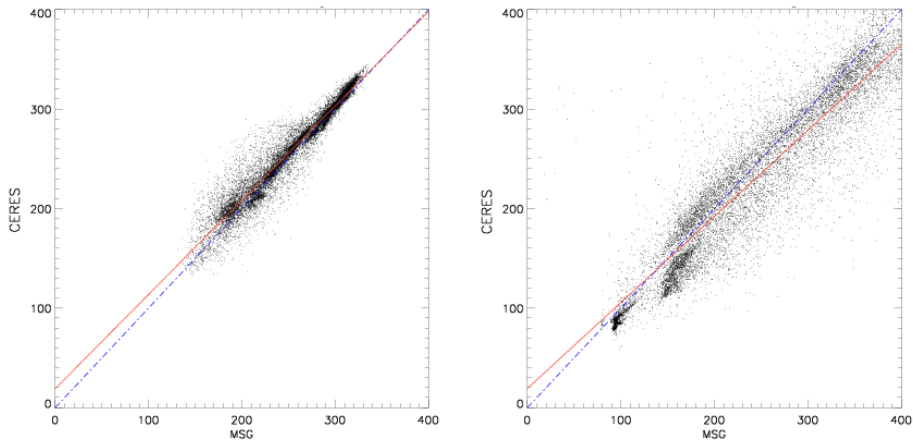


Figure B.2: 24/Mar/2004, 0800 UTC. Left: LW, Right: SW

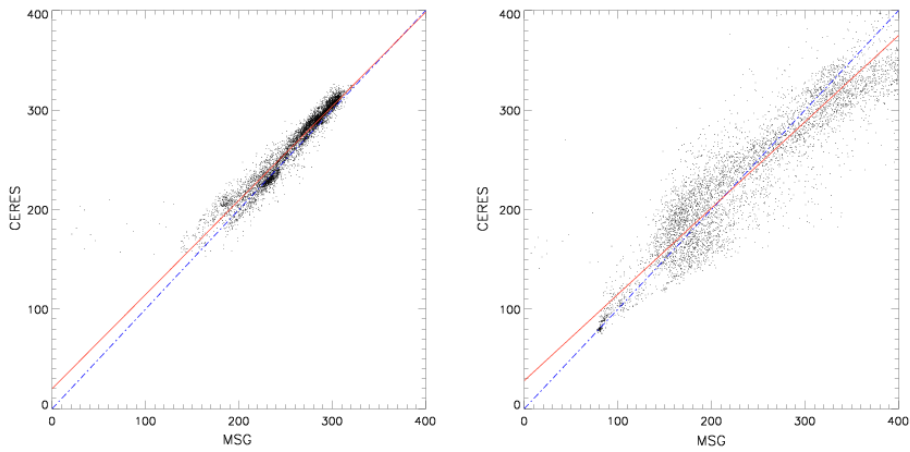


Figure B.3: 8/Abr/2004, 0730 UTC. Left: LW, Right: SW

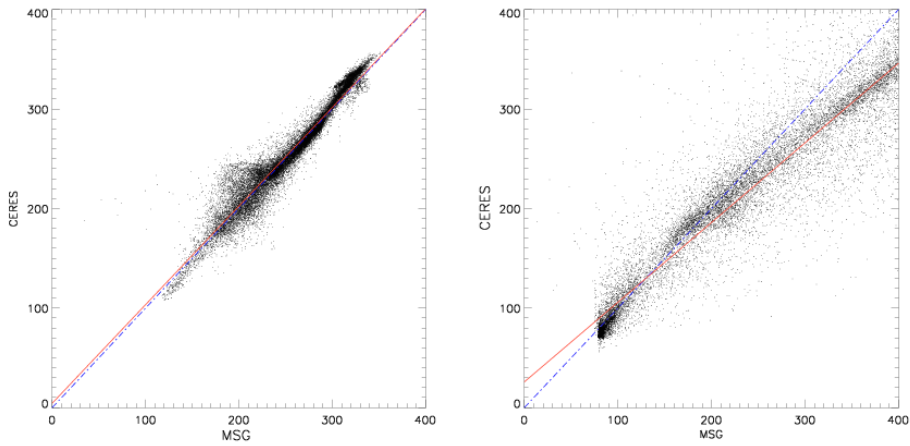


Figure B.4: 14/Jun/2004, 1115 UTC. Left: LW, Right: SW

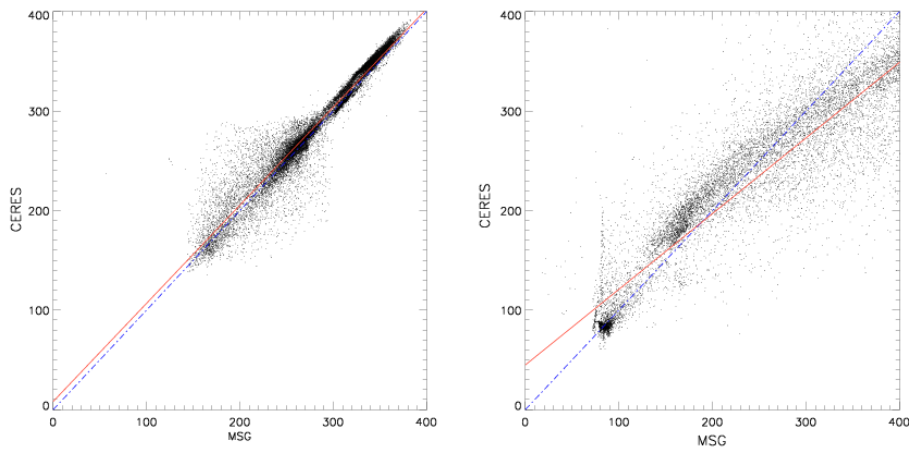


Figure B.5: 1/Jul/2004, 0830 UTC. Left: LW, Right: SW

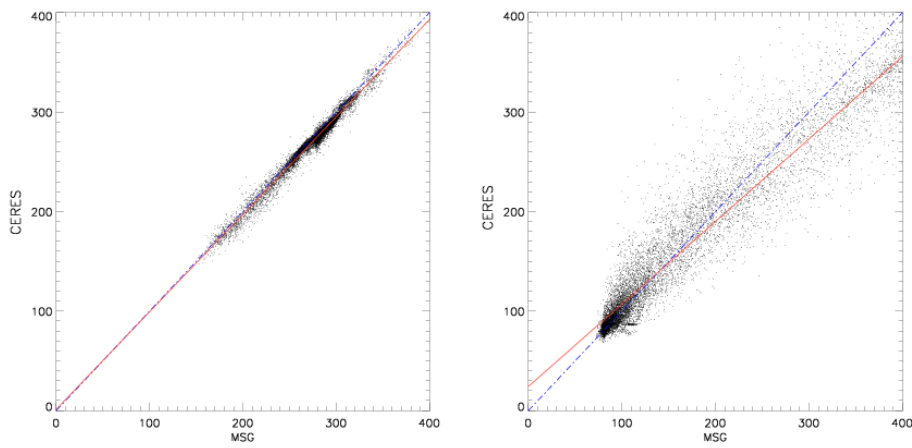


Figure B.6: 8/Jul/2004, 1200 UTC. Left: LW, Right: SW

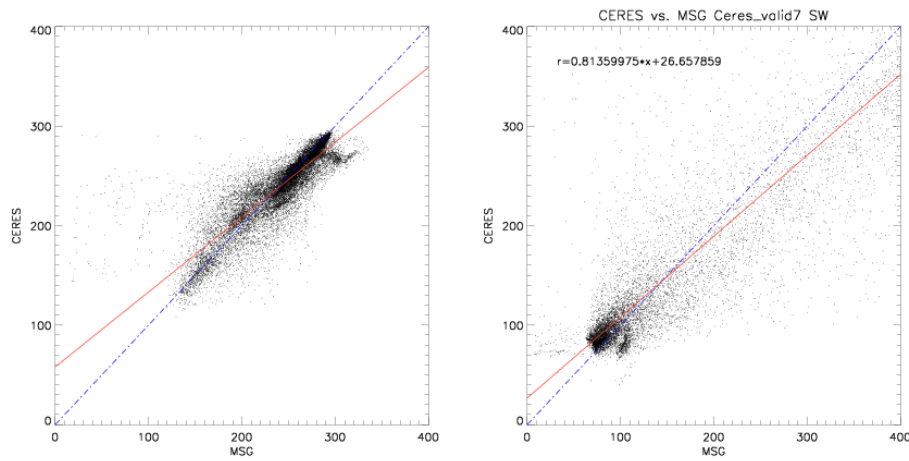


Figure B.7: 13/Ago/2004, 1445 UTC. Left: LW, Right: SW

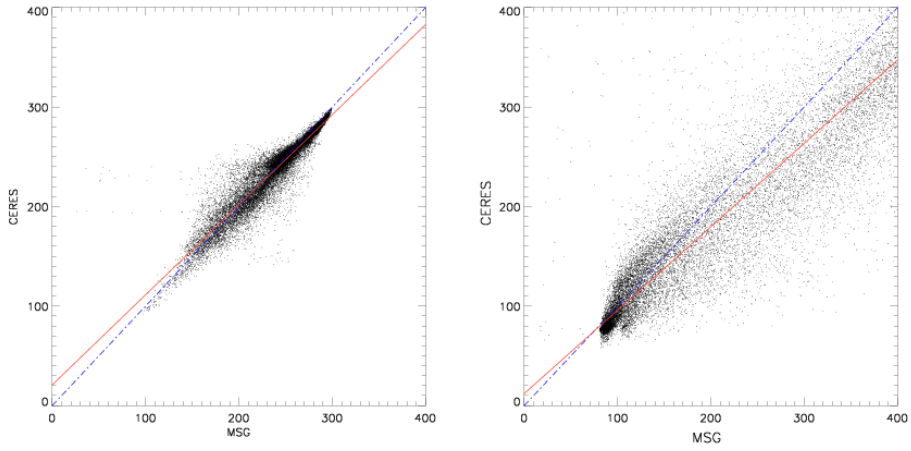


Figure B.8: 2/Sep/2004, 1245 UTC. Left: LW, Right: SW

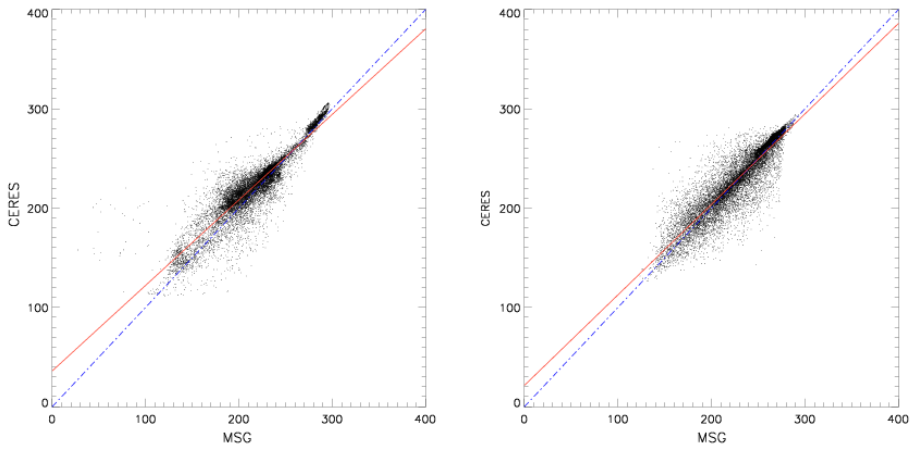


Figure B.9: Left: 15/Oct/2004, 1845 UTC. Right: 10/Nov/2004, 2100 UTC. No SW data due to the time of the day

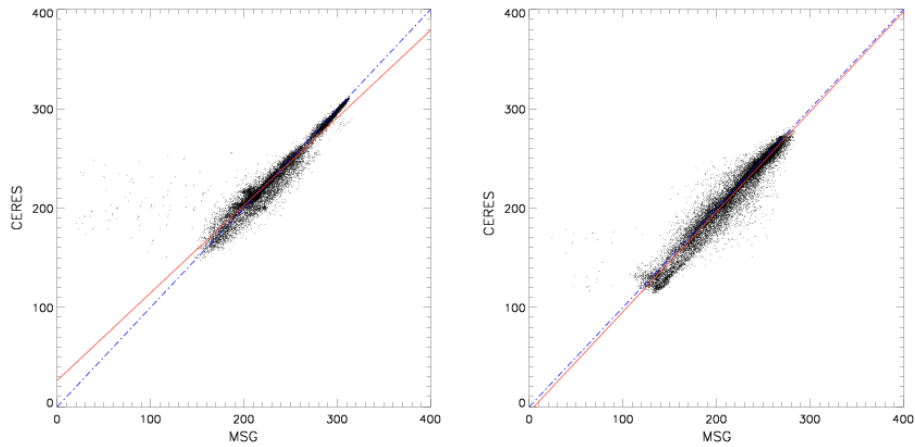


Figure B.10: Left: 2/Feb/2004, 0215 UTC. Right: 22/Dec/2004, 0215 UTC. No SW data due to the time of the day

Appendix C

Analysis of discrepancies

Additional examples of the discrepancies found in the validation of the Terra/CERES irradiances vs. the MSG/SEVIRI irradiances (see B) are shown in this appendix. The relative differences are plotted vs. diverse magnitudes (latitude, solar zenith angle and satellite zenith angle) in both the longwave and the shortwave ranges. It can be seen that none of the parameters here shown has a direct influence in the relative differences.

Latitude

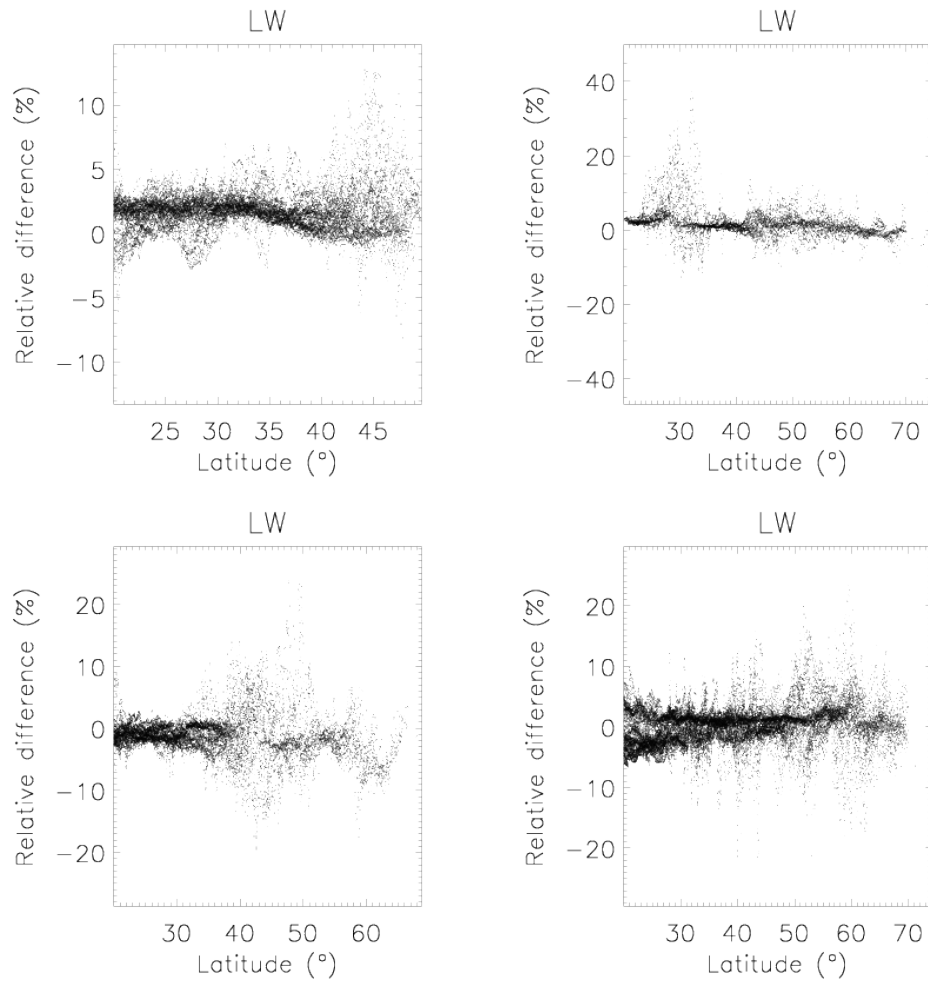


Figure C.1: Relative differences in LW vs. latitude corresponding to: top left, 8/Jul/04 1200 UTC; top right, 13/Aug/04 1445 UTC; bottom left, 24/Mar/04 0800 UTC; bottom right, 14/Jun/04 1115 UTC

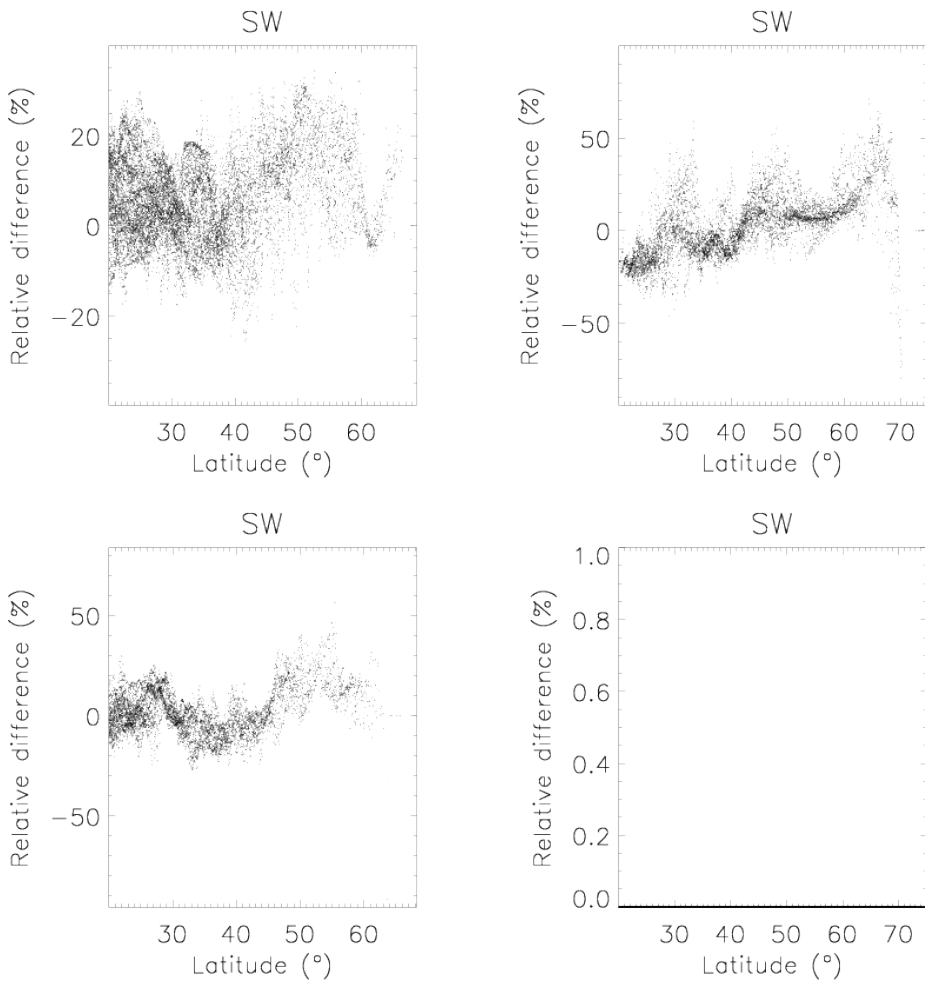


Figure C.2: Relative differences in SW vs. latitude corresponding to: top left, 4/Mar/04 0800 UTC; top right, 13/Aug/04 1445 UTC; bottom left, 8/Apr/04 0730 UTC; bottom right, 15/Oct/04 2100 UTC

Solar zenith angle

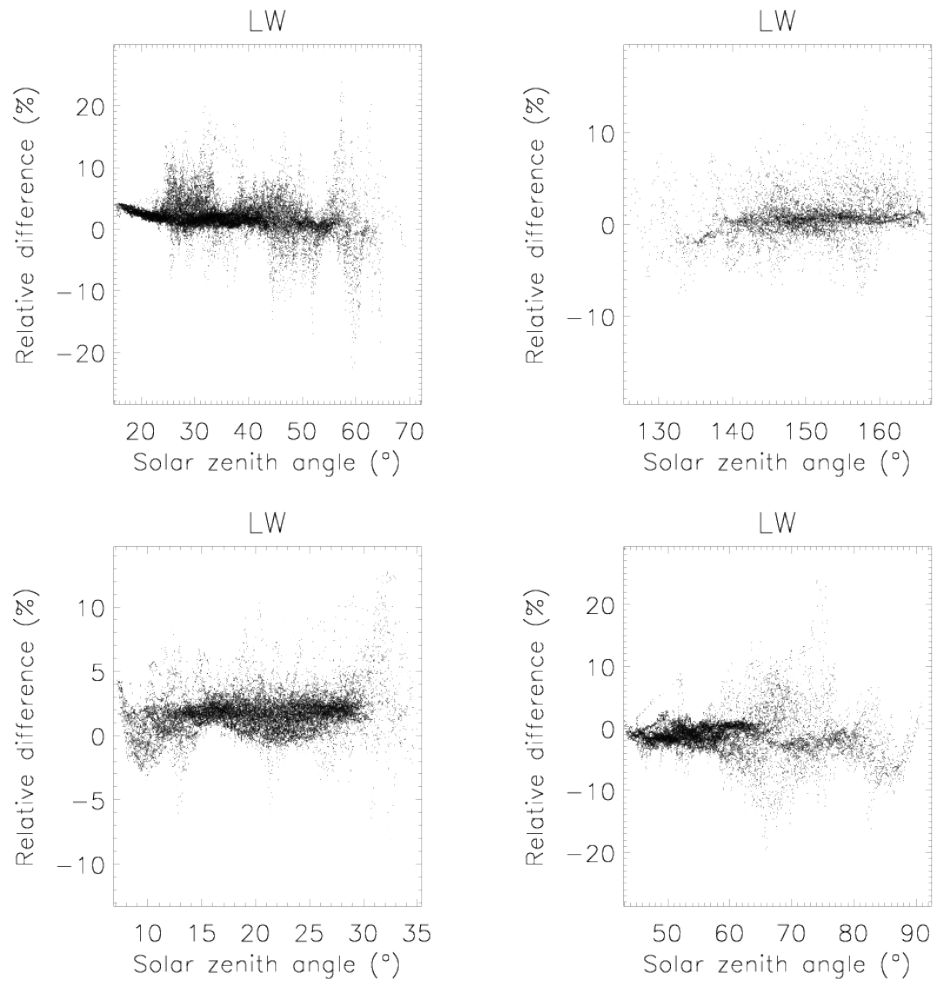


Figure C.3: Relative differences in LW vs. solar zenith angle corresponding to: top left, 2/Sep/04 1245 UTC; top right, 2/Feb/04 0215 UTC; bottom left, 8/Jul/04 1200 UTC; bottom right, 4/Mar/04 0800 UTC

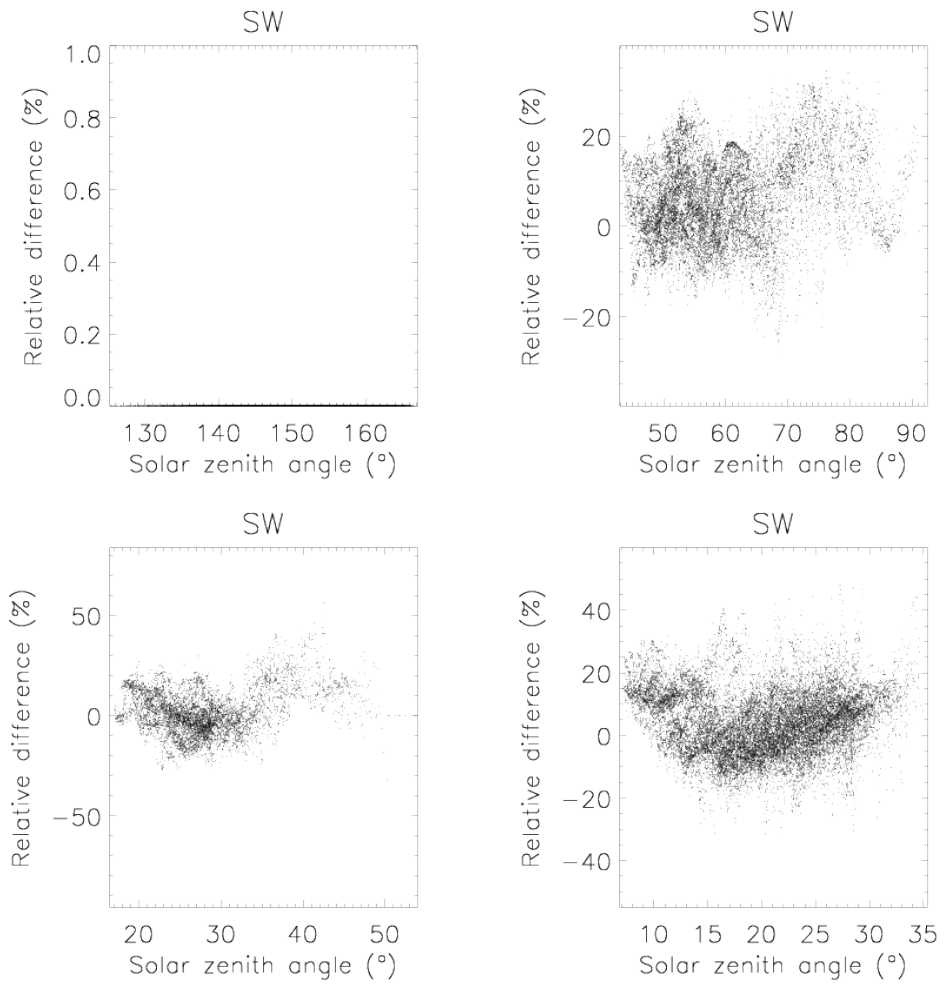


Figure C.4: Relative differences in SW vs. solar zenith angle corresponding to: top left, 2/Feb/04 0215 UTC; top right, 24/Mar/04 0800 UTC; bottom left, 8/Apr/04 0730 UTC; bottom right, 8/Jul/04 1200 UTC

Satellite zenith angle

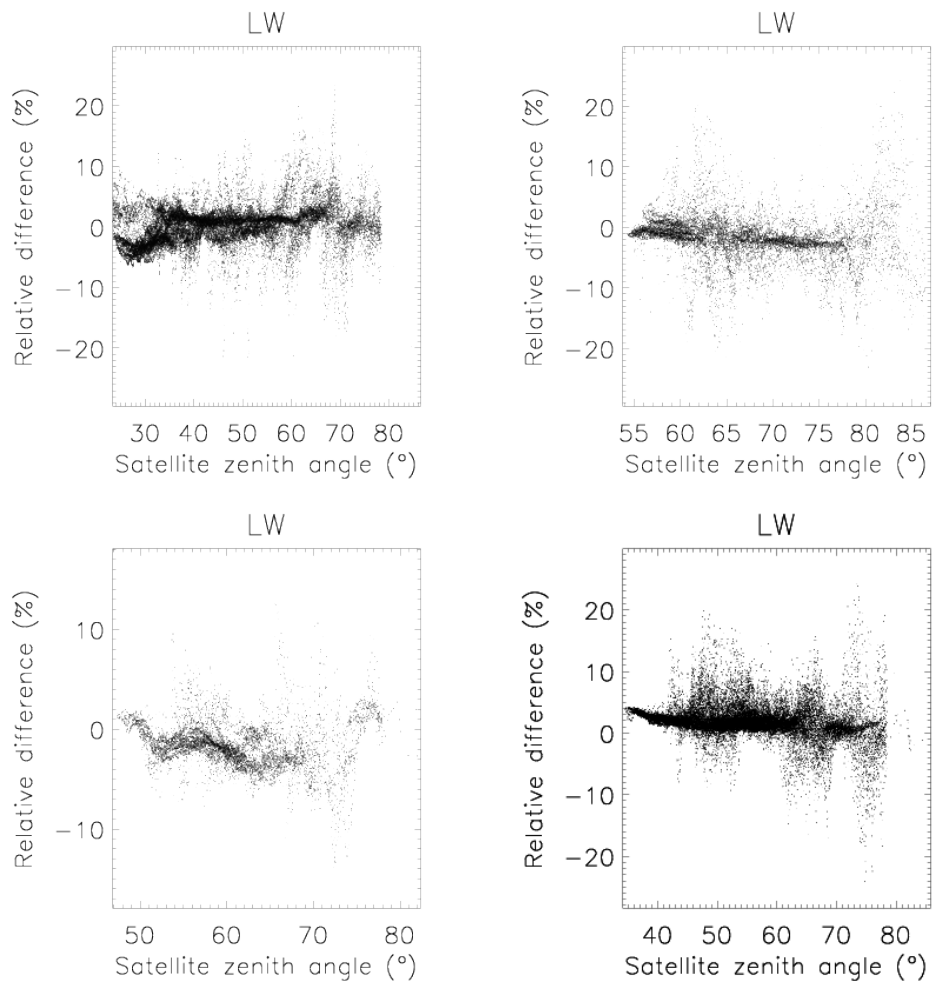


Figure C.5: Relative differences in LW vs. satellite zenith angle corresponding to: top left, 14/Jun/04 0915 UTC; top right, 15/Oct/04 2100 UTC; bottom left, 8/Apr/04 0730 UTC; bottom right, 2/Sep/04 1245 UTC

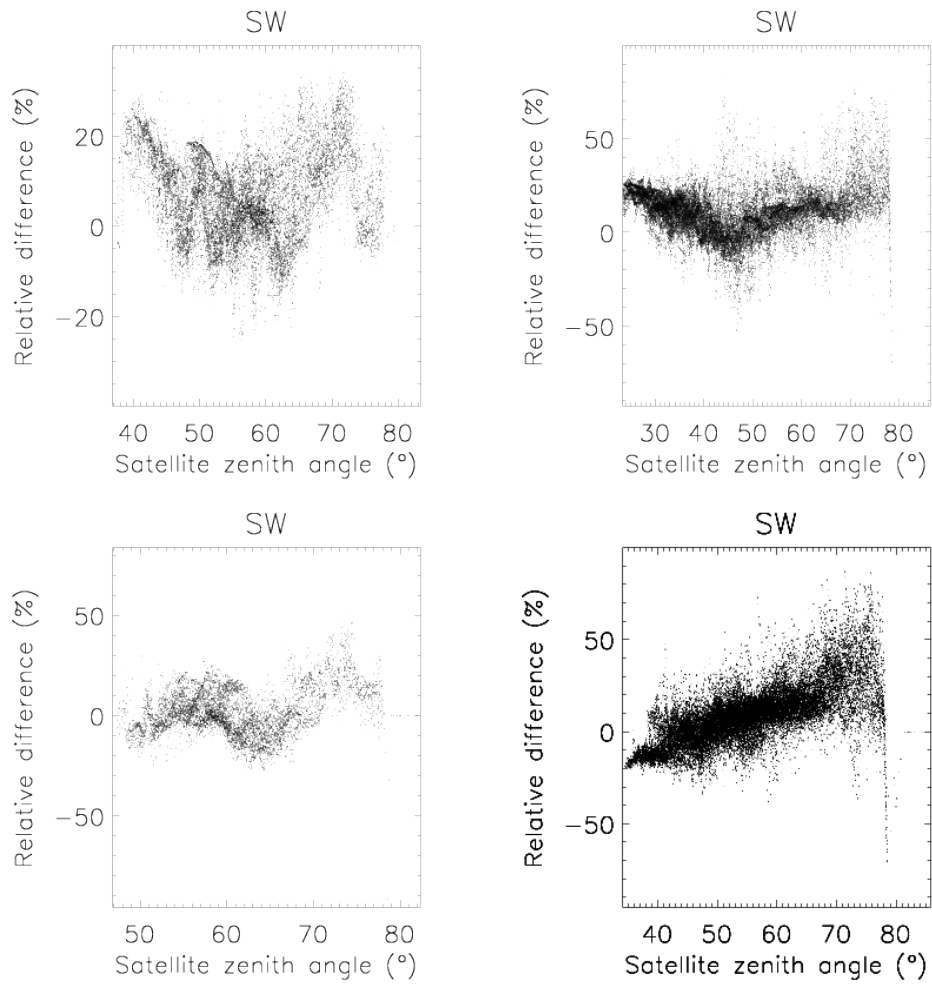


Figure C.6: Relative differences in SW vs. satellite zenith angle corresponding to: top left, 4/Mar/04 0800 UTC; top right, 14/Jun/04 0915 UTC; bottom left, 8/Apr/04 0730 UTC; bottom right, 2/Sep/04 1245 UTC

Appendix D

Validation of irradiances: GERB/MSG vs. SEVIRI/MSG

Linear fits of GERB irradiance data vs. the irradiance computed by the algorithms based on MSG/SEVIRI channels, smoothed using the filter that simulates the point spread function of the GERB detector. Unless otherwise specified, each pair of plots correspond to the same scene. LW (W/m^2) on the left, SW (W/m^2) on the right. Fit corresponds to the solid line; dashed line $y = x$ only for reference. Tables D.1 and D.2 show the slope, correlation coefficient, root mean square and bias of each of the fits. The extremely high correlation of both methods to retrieve the irradiances can be seen. Comparing these results with the validation in appendix B the advantage of comparing data from the same satellite is clear. The first three values of the table, showing a very large slope, correspond to scenes with a very high satellite viewing angle, nearly at the limits of the instrument performance and when only a small fraction of the Earth is illuminated under an extreme solar viewing angle (see time of the overpass).

MSG instrument		Longwave		Shortwave	
SEVIRI	GERB	Slope	R^2	Slope	R^2
12/05/06 20:00	19:59	0.99	99.81	1.40	97.82
12/05/06 19:45	19:42	0.99	99.80	1.39	98.19
15/05/06 18:30	18:39	0.99	99.65	1.14	97.92
18/05/06 11:30	11:27	1.00	99.70	0.97	98.56
20/05/06 03:00	03:00	0.98	99.66	-	-
22/05/06 00:15	00:14	0.98	99.65	-	-
25/05/06 15:00	15:01	0.99	99.70	0.99	97.93
29/05/06 14:15	14:17	1.00	99.66	0.96	97.84
01/06/06 12:45	12:41	1.00	98.50	0.91	95.19
03/06/06 10:00	09:54	1.00	98.66	0.92	96.11
10/06/06 22:22	22:02	0.92	97.77	-	-
12/06/06 07:30	07:24	0.99	98.61	0.91	96.53

Table D.1: Results of the comparisons between MSG/GERB and MSG/SEVIRI irradiances. Slope and correlation coefficient

MSG Instrument		Longwave			Shortwave		
SEVIRI	GERB	Mean (W/m ²)	RMS (W/m ²)	Bias (W/m ²)	Mean (W/m ²)	RMS (W/m ²)	Bias (W/m ²)
12/05/06 20:00	19:59	238.25	12.2	-1.91	101.43	36.13	39.52
12/05/06 19:45	19:42	237.94	11.75	-0.82	110.90	39.48	43.13
15/05/06 18:30	18:39	244.07	11.41	-2.01	134.46	44.26	25.91
18/05/06 11:30	11:27	254.19	17.23	-1.11	294.72	45.35	-3.15
20/05/06 03:00	03:00	238.71	14.86	-2.32	-	-	-
22/05/06 00:15	00:14	243.90	14.51	-2.14	-	-	-
25/05/06 15:00	15:01	242.67	16.30	-2.42	267.35	52.56	0.577
29/05/06 14:15	14:17	256.96	15.59	-1.09	269.77	48.27	-10.16
01/06/06 12:45	12:41	273.99	8.57	-0.89	296.88	48.81	-9.88
03/06/06 10:00	09:54	276.65	7.81	-1.20	281.81	41.42	-7.36
10/06/06 22:22	22:02	261.14	8.06	-3.01	-	-	-
12/06/06 07:30	07:24	266.35	7.32	-3.24	251.95	31.75	-12.18

Table D.2: Results of the comparisons between MSG/GERB and MSG/SEVIRI irradiances. Mean irradiance, root mean square (RMS) and bias

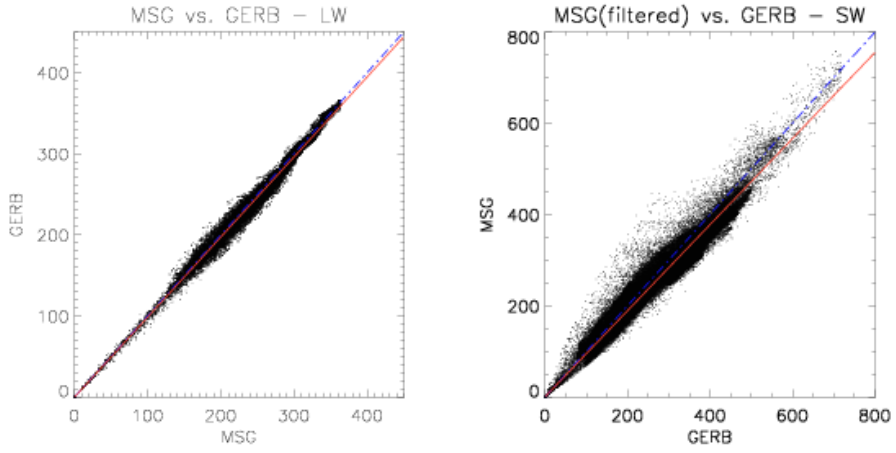


Figure D.1: 12-Jun-06, 0730 UTC

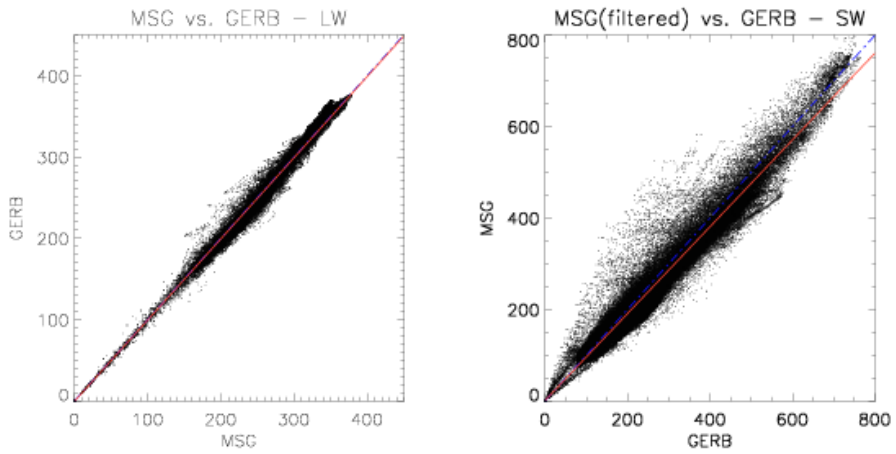


Figure D.2: 1-Jun-06, 1245 UTC

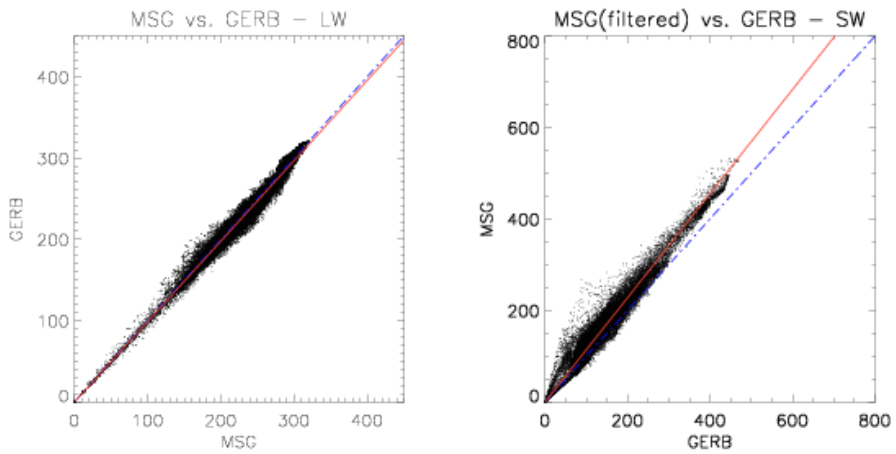


Figure D.3: 15-May-06, 1830 UTC

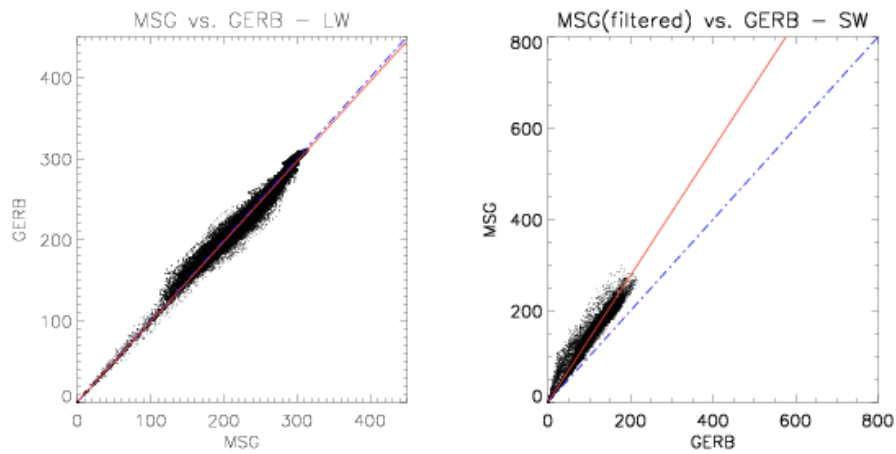


Figure D.4: 12-May-06, 1945 UTC

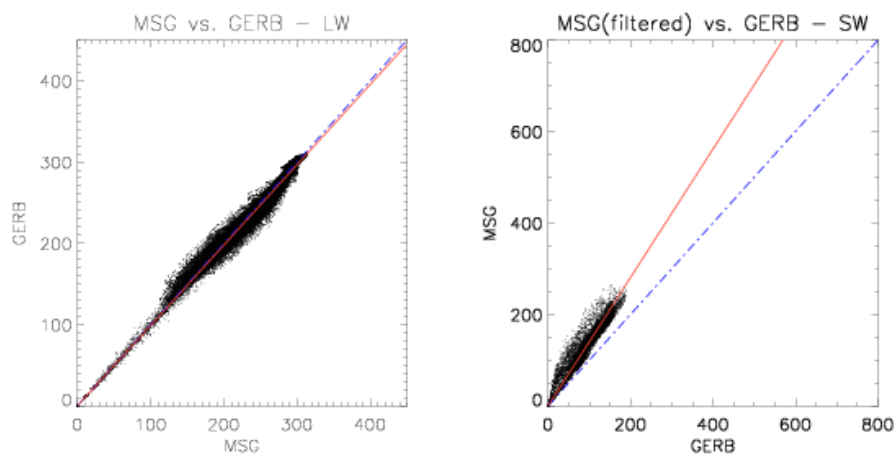


Figure D.5: 12-May-06, 2000 UTC

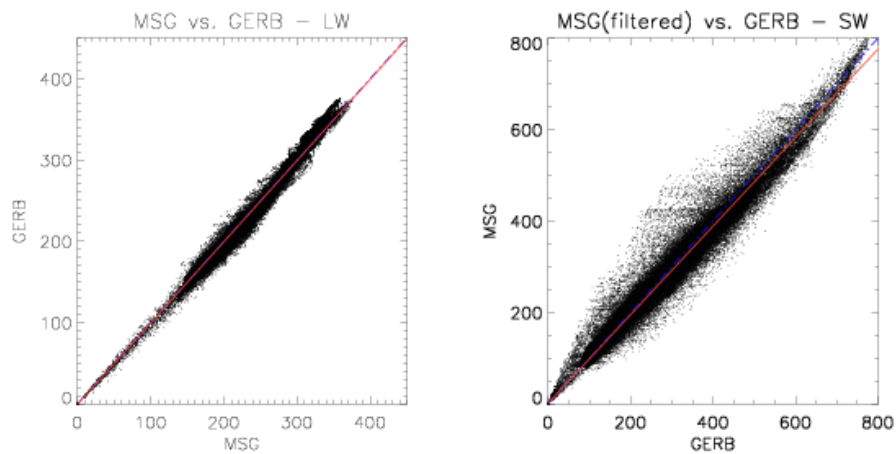


Figure D.6: 18-May-06, 1130 UTC

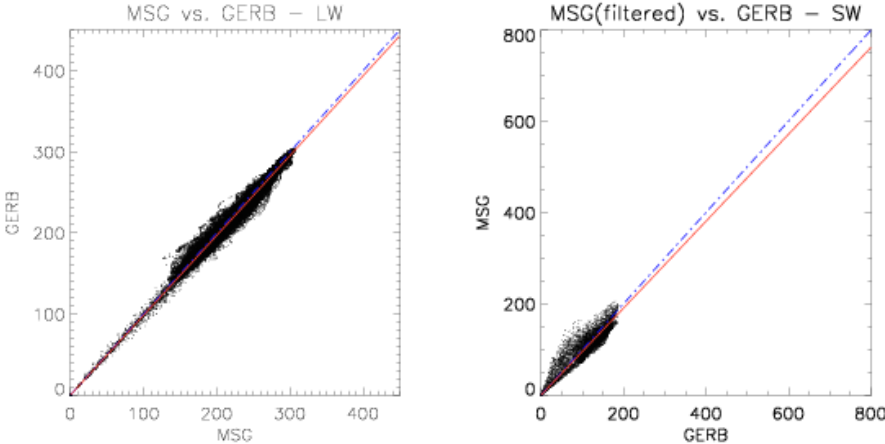


Figure D.7: 20-May-06, 0300 UTC

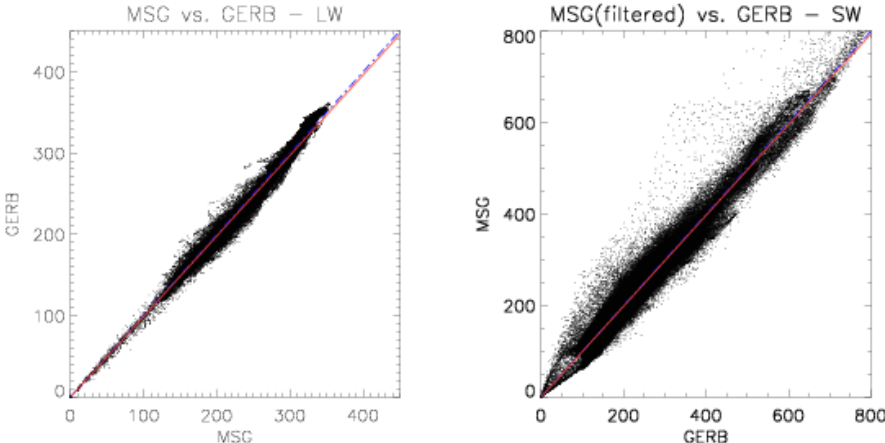


Figure D.8: 25-May-06, 1500 UTC

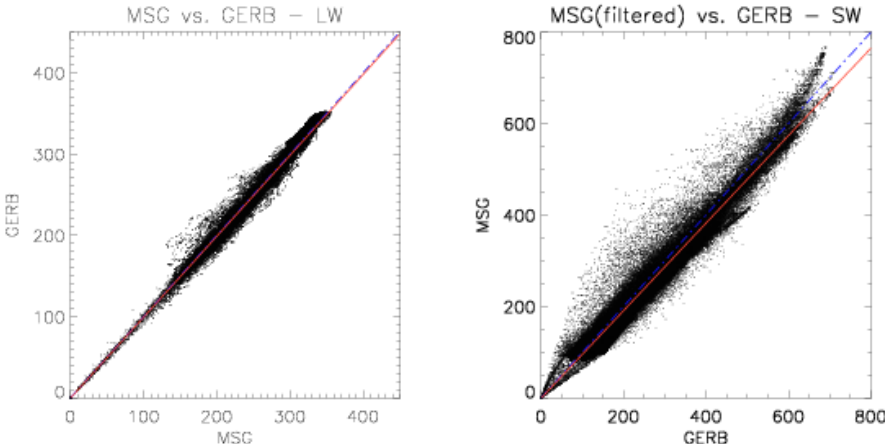


Figure D.9: 29-May-06, 1415 UTC

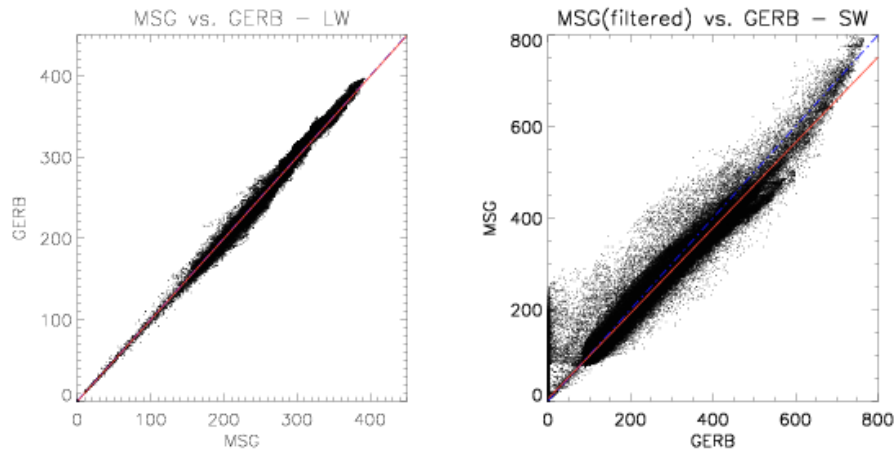


Figure D.10: 3-Jun-06, 1000 UTC

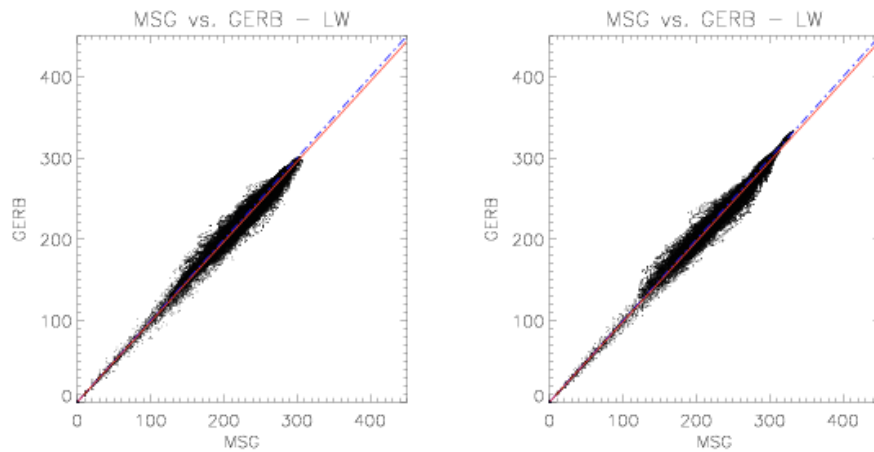


Figure D.11: Left: longwave, 22-May-06, 0000 UTC. Right: longwave, 10-Jun-06, 2200 UTC. Nighttime, no SW data.

Acronyms

ACTA	Automatic Contrail Tracking Algorithm
AIC	Aviation Induced Cloudiness
ANN	Artificial Neural Network
ARG	Averaged Rectified Geolocated (GERB products)
ATBD	Algorithm Theoretical Basis Documents
AVHRR	Advanced Very High Resolution Radiometer (NOAA Satellites)
BTD	Brightness Temperature Difference
CDA	Contrail Detection Algorithm
CERES	Clouds and the Earth's Radiant Energy System (TERRA/AQUA)
DE	Detection Efficiency
EADS	European Aeronautic Defence and Space Company
ECMWF	European Centre for Medium-Range Weather Forecasts
ERB	Earth Radiation Budget
EOS	Earth Observing System (NASA)
EUMETSAT	European Organisation for the Exploitation of Meteorological Satellites
FAR	False Alarm Rate
GDP	Gross Domestic Product
GERB	Geostationary Earth Radiation Budget (MSG)
GOES	Geostationary Operational Environmental Satellites (NOAA Satellites)
HDF	Hierarchical Data Format File
HIRS	High Resolution Infra-Red Sounder (NOAA Satellites)
HRV	High Resolution Visible channel on MSG
IDL	Interactive Data Language
IPCC	International Panel on Climate Change

LaRC	Langley Research Center
LEO	Low Earth Orbit
LIDAR	Light Detection and Ranging
LoG	Laplacian of Gaussian
LW	Longwave
MCP	Mission Communications Payload (MSG)
MeCiDA	MSG Cirrus Detection Algorithm
MODIS	MODERate resolution Imaging Spectroradiometer (TERRA/AQUA)
MSG	Meteosat Second Generation
NASA	National Aeronautics and Space Administration
NN	Neural Network
NOAA	National Oceanic and Atmospheric Administration
OLR	Outgoing Longwave Radiation
PSF	Point Spread Function
RAL	Rutherford Appleton Laboratory
RAP	Rotating Azimuth Plane (CERES)
RF	Radiative Forcing
RMIB	Royal Meteorological Institute of Belgium
RMS	Root Mean Square
ROLSS	RMIB On-Line Short-term Service
RSS	Rapid Scan Service
S&R	Search and Rescue transponder (MSG)
SEVIRI	Spinning Enhanced Visible and Infra-Red Imager
SW	Shortwave
TERRA/AQUA	NASA's Earth Observing System (EOS) satellites
TOA	Top Of Atmosphere
TRMM	Tropical Rainfall Measuring Mission (NASA)
UTC	Coordinated Universal Time

Bibliography

- Ackerman, S., Strabala, K., Menzel, P., Frey, R., Moeller, C., Gumley, L., Baum, B., Seaman, S. W., and Zhang, H. (2006). *Discriminating clear-sky from cloud with MODIS. Algorithm Theoretical Basis Document (MOD35)*.
- Atlas, D., Wang, Z., and Duda, D. P. (2006). Contrails to cirrus: morphology, microphysics, and radiative properties. *J. Appl. Meteorol.*, 45:5–19.
- Bakan, S., Betancor, M., Gayler, V., and Grassl, H. (1994). Contrail frequency over Europe from NOAA-satellite images. *Ann. Geophysicae*, 12:962–968.
- Bates, M. J., Smith, A., Allan, P. M., Coan, B., Lepine, D. R., Ricketts, M. J., and Stewart, B. C. (2004). Geolocation accuracy of GERB data. In *Proc. 2004 EUMETSAT Meteorological Satellite Conference*.
- Boltzmann, L. (1884). Ableitung des Stefanschen Gesetzes, betreffend die Abhaengigkeit der Waermestrahlung von der Temperatur aus der electromagnetischen Lichttheorie. *Annalen der Physik und Chemie*, 22:291–294.
- Canty, M. J. (2007). *Image analysis, classification and change detection in remote sensing*. CRC Taylor & Francis.
- Charlock, T. P. and Alberta, T. L. (1996). The CERES/ARM/GEWEX Experiment (CAGEX) for the retrieval of radiative fluxes with satellite data. *B. Am. Meteorol. Soc.*, 77(11):2673–2683.
- Chen, T., Rossow, W. B., and Zhang, Y. (2000). Radiative effects of cloud-type variations. *J. Climate*, 13:264–286.
- Diekmann, F. J. and Smith, G. L. (1988). Investigation of scene identification algorithms for radiation budget measurements. *J. Geophys. Res.*, 94:3395–3412.
- Duda, D. P., Minnis, P., Nguyen, L., and Palikonda, R. (2004). A case study of the development of contrail clusters over the Great Lakes. *J. Atmos. Sci.*, 61:1132–1146.
- Duda, D. P., Spinhirne, J. D., and Hart, W. D. (1998). Retrieval of contrail microphysical properties during SUCCESS by the split-window method. *Geophys. Res. Lett.*, 25(8):1149–1152.
- EUMETSAT (2005a). *Level 1.5 Data Format Description*, eum/msg/icd/105 edition.

- EUMETSAT (2005b). *LRIT/HRIT Mission Specific Implementation*, EUM/MSG/SPE/057 edition.
- Fu, Q. and Liou, K. N. (1993). Parameterization of the radiative properties of cirrus clouds. *J. Atmos. Sci.*, 50(13):2008–2025.
- Gierens, K. (1996). Numerical simulations of persistent contrails. *J. Atmos. Sci.*, 53(22):3333–3348.
- Gierens, K. (2006). Contrails, contrail cirrus, and ship tracks. In *International Conference on Transport, Atmosphere and Climate*, Oxford, UK.
- Gierens, K., Sausen, R., and Schumann, U. (1999). A diagnostic study of the global distribution of contrails. Part II: Future air traffic scenarios. *Theor. Appl. Climatol.*, 63:1–9.
- Harries, J. E., Russell, J. E., Hanafin, J. A., Brindley, H., Futyan, J., Rufus, J., Kellock, S., Matthews, G., Wrigley, R., Last, A., Mueller, J., Mossavati, R., Ashmall, J., Sawyer, E., Parker, D., Caldwell, M., Allan, P. M., Smith, A., Bates, M. J., Coan, B., Stewart, B. C., Lepine, D. R., Cornwall, L. A., Corney, D. R., Ricketts, M. J., Drummond, D., Smart, D., Cutler, R., Dewitte, S., Clerbaux, N., Gonzalez, L., Ipe, A., Bertrand, C., Joukoff, A., Crommelynck, D., Nelms, N., Llewellyn-Johnes, D. T., Butcher, G., Smith, G. L., Szewczyk, Z. P., Mlynchak, P. E., Slingo, A., Allan, R. P., and Ringer, M. A. (2005). The Geostationary Earth Radiation Budget Project. *B. Am. Meteorol. Soc.*, 86(7):945–960.
- Kaercher, B., Burkhardt, U., Unterstrasser, S., and Minnis, P. (2009). Factors controlling contrail cirrus optical depth. *Geophys. Res. Lett.*, 9:11589–11658.
- Kiehl, J. and Trenberth, K. (1997). Earth’s annual global mean energy budget. *Bull. Am. Meteorol. Soc.*, 78:197206.
- King, M. D. and Nakajima, T. (1990). Determination of the optical thickness and effective particle radius of clouds from reflected solar radiation measurements. part i: Theory. *J. Atmos. Sci.*, 47:1878–1893.
- King, M. D., Tsay, S.-C., Platnick, S. E., Wang, M., and Liou, K.-N. (2007). *Cloud retrieval algorithms for MODIS: optical thickness, effective particle radius, and thermodynamic phase*. MODIS Algorithm Theoretical Basis Document No. ATBD-MOD-05. MOD06-Cloud product.
- Krebs, W. (2006). *Analyse des Einflusses des Flugverkehrs auf die natürliche Zirrusbewoelkung über Europa, Nordafrika und dem Nordatlantik*. PhD thesis, Ludwig-Maximilians-Universitaet Muenchen. DLR Forschungsbericht ISRN DLR-FB–2006-10.
- Krebs, W., Mannstein, H., Bugliaro, L., and Mayer, B. (2007). Technical note: A new day-and night-time Meteosat Second Generation Cirrus Detection Algorithm MeCiDA. *Atmos. Chem. Phys.*, 7:6145–6159.
- Lee, D. S., Fahey, D. W., Forster, P. M., Newton, P. J., Wit, R. C. N., Lim, L. L., Owen, B., and Sausen, R. (2009). Aviation and global climate change in the 21st century. *Atmos. Environ.*, 43:3520–3537.

- Lee, T. F. (1989). Jet contrail identification using the AVHRR infrared split window. *J. Appl. Meteorol.*, 28:993–995.
- Loeb, N. G., Kato, S., Loukachine, K., and Manalo-Smith, N. (2005). Angular Distribution Models for Top-Of-Atmosphere radiative flux estimation from the Clouds and the Earth’s Radiant Energy System Instrument on the Terra satellite. Part I: Methodology. *J. Atmos. Oceanic Technol.*, 22:338–351.
- Loeb, N. G., Loukachine, K., Manalo-Smith, N., Wielicki, B. A., and Young, D. F. (2003). Angular Distribution Models for Top-Of-Atmosphere radiative flux estimation from the Clouds and the Earth’s Radiant Energy System Instrument on the Tropical Rainfall Measuring Mission satellite. Part II: Validation. *J. Appl. Meteorol.*, 42:1748–1769.
- Mannstein, H., Meyer, R., and Wendling, P. (1999). Operational Detection of Contrails from NOAA-AVHRR-Data. *Int. J. Remote Sens.*, 20(8):1641 – 1660.
- Mannstein, H. and Schumann, U. (2005). Aircraft induced contrail cirrus over europe. *Meteorol. Z.*, 14:549 – 554.
- Marquart, S., Ponater, M., Mager, F., and Sausen, R. (2003). Future development of contrail cover, optical depth and radiative forcing: impacts of increasing air traffic and climate change. *J. Climate*, 16:2890–2904.
- Mayer, B. and Kylling, A. (2005). Technical Note: The libRadtran software package for radiative transfer calculations: Description and examples of use. *Atmos. Chem. Phys. Discuss.*, 5:1319–1381.
- Meerkoetter, R., Schumann, U., Doelling, D. R., Minnis, P., Najakima, T., and Tsushima, Y. (1999). Radiative forcing by contrails. *Ann. Geophys.*, 17:1080–1094.
- Meyer, R., Buell, R., Leiter, C., Mannstein, H., Marquart, S., Oki, T., and Wendling, P. (2007). Contrail observations over Southern and Eastern Asia in NOAA/AVHRR data and comparisons to contrail simulations in a GCM. *Int. J. Remote Sens.*, 28(9):2049–2069.
- Meyer, R., Mannstein, H., Meerkoetter, R., Schumann, U., and Wendling, P. (2002). Regional radiative forcing by line-shaped contrails derived from satellite data. *J. Geophys. Res.*, 107(D10).
- Minnis, P., Ayers, J. K., Palikonda, R., and Phan, D. (2004). Contrails, cirrus trends, and climate. *J. Climate*, 17:1671–1685.
- Minnis, P., Palikonda, R., Walter, B. J., Ayers, J. K., and Mannstein, H. (2005). Contrail properties over the eastern North Pacific from AVHRR data. *Meteor. Z.*, 14:515–523.
- Minnis, P., Schumann, U., Doelling, D. R., Gierens, K., and Fahey, D. W. (1999). Global distribution of contrail radiative forcing. *Geophys. Res. Lett.*, 26(13):1853–1856.
- Minnis, P., Young, C. F., Garber, D. P., Nguyen, L., Jr., W. L. S., and Palikonda, R. (1998). Transformation of contrails into cirrus during SUCCESS. *Geophys. Res. Lett.*, 25:3119–3122.

- Minnis, P., Young, D. F., Kratz, D. P., Jr., J. A. C., King, M. D., Garber, D. P., Heck, P. W., Mayor, S., and Arduini, R. F. (1997). *Clouds and the Earth's Radiant Energy System (CERES), Algorithm Theoretical Basis Document, Cloud Optical Property Retrieval (Subsystem 4.3)*.
- Mlynczak, P. E., Szewczyk, Z. P., Smith, G. L., Russell, J. E., Harries, J. E., Dewitte, S., and Clerbaux, N. (2006). Comparisons of GERB and CERES measurements. In *Proc. 13th Sat. Met. and Ocean*.
- Palikonda, R., Minnis, P., Costulis, P. K., and Dudad, D. P. (2002). Contrail climatology over the USA from MODIS and AVHRR data. In *Abstract for the 10th Conference on Aviation, Range and Aerospace Meteorology. Portland, Oregon*.
- Palikonda, R., Minnis, P., Duda, D. P., and Mannstein, H. (2005). Contrail coverage derived from 2001 AVHRR data over the continental United States of America and surrounding areas. *Meteor. Z.*, 14:515–523.
- Palikonda, R., Minnis, P., Heck, P. W., Sun-Mack, S., Trepte, Q. Z., and Mannstein, H. (2001). Contrail cover and radiative properties from high-resolution satellite data. In *Proceedings AMS 11th Conference on Satellite Meteorology and Oceanography. Madison, Wisconsin*, pages 508–511.
- Penner, J. E., Lister, D. H., Griggs, D. J., Dokken, D. J., and McFarlands, M. (1999). *Aviation and the Global Atmosphere*. Intergovernmental Panel on Climate Change, Cambridge University Press. Cambridge UK edition.
- Planck, M. (1901). Über das Gesetz der Energieverteilung im Normalspektrum. *Ann. Physik*, 4(553).
- Platnick, S., Li, J. Y., King, M. D., Gerber, H., and Hobbs, P. V. (2001). A solar reflectance method for retrieving the optical thickness and droplet size of liquid water clouds over snow and ice surfaces. *J. Geophys. Res.*, 106:15185–15199.
- Ponater, M., Marquart, S., and Sausen, R. (2002). Contrails in a comprehensive global climate model: parameterization and radiative forcing results. *J. Geophys. Res.*, 107(D13).
- Rumelhart, D. E., Hinton, G., and Williams, R. (1986). Learning representations by back-propagating errors. *Nature*, 323:533–536.
- Russell, J. E., Dewitte, S., and Harries, J. E. (2006). *Quality Summary: GERB L2 ARG, 3 scan average Edition 1 product*. GERB project team.
- Sassen, K. (1997). Contrail-cirrus and their potential for regional climate change. *B. Am. Meteorol. Soc.*, 78(9):1885–1903.
- Sausen, R., Gierens, K., Ponater, M., and Schumann, U. (1998). A diagnostic study of the global distribution of contrails. part i: Present day climate. *Theor. Appl. Climatol.*, 61:127–141.

- Sausen, R., Isaksen, I., Grewe, V., Hauglustaine, D., Lee, D., Myhre, G., Khler, M., Pitari, G., Schumann, U., Stordal, F., and Zerefos, C. (2005). Aviation radiative forcing in 2000: An update on IPCC (1999). *Meteorol. Z.*, 14:555–561.
- Schmetz, J., Pili, P., Tjemkes, S., Just, D., Kermann, J., Rota, S., and Ratierk, A. (2002). An introduction to Meteosat Second Generation (MSG). *B. Am. Meteorol. Soc.*, pages 977–992.
- Schroeder, F., Kaercher, B., Duroure, C., Stroem, K., Petzold, A., Gayet, J. F., Strauss, B., Wendling, P., and Borrmann, S. (2000). On the transition of contrails into cirrus clouds. *J. Atmos. Sci.*, 57:464–480.
- Schumann, U. (1996). On conditions for contrail formation from aircraft exhausts. *Meteorol. Z.*, 5:4–23.
- Schumann, U. (2005). Formation, properties and climatic effects of contrails. *C. R. Physique*, 6:549–565.
- Smith, G. L. and Manalo-Smith, N. (1995). Scene identification error probabilities for evaluating earth radiation budget measurements. *J. Geophys. Res.*, 100(D5).
- Solomon, S., Qin, D., Manning, M., Marquis, M., Averyt, K., Tignor, M. M. B., Miller, H. L., and Chen, Z. (2007). *Climate change 2007. The physical science basis. Contribution of Working Group I to the Fourth Assessment Report of the Intergovernmental Panel on Climate Change*. Intergovernmental Panel on Climate Change, cambridge university press. cambridge uk edition.
- Stark, J.-L., Murtagh, R., and Bijaoui, A. (1998). *Image Processing and Data Analysis. The multiscale approach*. Cambridge University Press.
- Stefan, J. (1879). Über die Beziehung zwischen der Wärmestrahlung und der Temperatur. *Sitzungsberichte der mathematisch-naturwissenschaftlichen Classe der kaiserlichen Akademie der Wissenschaften*, 79:391–428.
- Stuber, N. and Forster, P. (2007). The impact of diurnal variations of air traffic on contrail radiative forcing. *Atmos. Chem. Phys.*, 7:3153–3162.
- Wallace, J. M. and Hobbs, P. V. (1977). *Atmospheric Science, an introductory survey*. Academic Press.
- Wielicki, B. A., Barkstrom, B. R., Harrison, E. F., III, R. B. L., Smith, G. L., and Cooper, J. E. (1996). Clouds and the Earth’s Radiant Energy System (CERES): An Earth Observing System experiment. *B. Am. Meteorol. Soc.*, 77(5):853–632.
- Wien, W. (1896). Über die Energieverteilung im Emissionsspectrum eines schwarzen Körpers. *Annalen der Physik*, 662.
- Zerefos, C., Eleftheratos, K., Balis, D., Zanis, P., Tselioudis, G., and Meleti, C. (2003). Evidence of impact of aviation on cirrus cloud formation. *Atmos. Chem. Phys.*, 3:1633–1644.

Danksagung

Diese Arbeit wäre ohne die Hilfe zahlreicher Personen nicht möglich gewesen, bei denen ich mich an dieser Stelle bedanken möchte.

Zuerst möchte ich mich bei meinem Doktorvater Prof. Dr. Schumann dafür bedanken, dass er mir die Gelegenheit gegeben hat, diese Arbeit am Institut für Physik der Atmosphäre (DLR) durchzuführen, für die Förderung und Begutachtung und für seine interessanten Anmerkungen und Ideen.

Ich bedanke mich bei Prof. Dr. Mayer für seine konstruktiven Verbesserungsvorschläge, seine Hinweise wie auch für seine motivierte Mithilfe und für die Übernahme des Zweitgutachtens.

Ein ganz besonders großer Dank gilt Dr. Mannstein für die Betreuung dieser Arbeit. Seine Hilfsbereitschaft, sein umfassendes Wissen und seine wertvollen Ratschläge auf diesem Gebiet waren für mich eine unschätzbare Hilfe. Der von ihm entwickelte CDA war entscheidend für die Entstehung dieser Arbeit.

Ich möchte mich auch bei Dr. Bugliaro für seine immer interessanten Anregungen und für die große und freundliche Hilfe im Umgang mit MSG und IDL bedanken.

Gleiches gilt für Dr. Krebs für seinen wesentlichen Beitrag zu den ersten Schritten dieser Arbeit.

Allen Kollegen der Abteilung gilt ein großer Dank für die freundliche Hilfe und Bereitschaft zur Beantwortung der vielen Fragen in allen möglichen Fachgebieten. Insbesondere bedanke ich mich bei meinen Zimmerkollegen Kaspar Graf, Stephan Kox und Tanja Reize für die produktive Arbeitsatmosphäre und Hilfestellungen bezüglich \LaTeX , Linux, Deutsch und Fachfragen (nicht immer unbedingt in dieser Reihenfolge).

Ich bedanke mich recht herzlich bei meinen Eltern, die mich zu dieser Arbeit immer ermutigt haben; bei meiner Schwester, deren Dissertation mit "you're next, Marga!" endete, für ihre Unterstützung; bei meinen Freunden für die Hilfe in vielfältiger Art und Weise und bei Quique für seine Geduld und ständige Unterstützung sowohl in guten als auch in schwierigen Zeiten während der letzten drei Jahre.

Lebenslauf

Persönliche Daten:

Name Margarita R. Vázquez Navarro
geboren am 10.12.1980
in Madrid, Spanien
Familienstand ledig

Schulbildung:

Sept. 1985 - Juli 1988 Colegio San Juan Bosco (Grundschule)
Sept. 1988 - Juli 1998 Colegio Santa María del Pilar (Grundschule und Gymnasium)
Juni 1008 Selectividad (Abitur)

Studium:

Okt. 1998 - März 2004 Studium Physik
an der Universidad Complutense de Madrid (UCM)
Okt. 2000 - Juli 2001 Studium Physik an der
Université Denis Diderot, Paris VII (Austausch)
Juli 2004 Diplom in Physik (UCM), Diplomarbeit zum Thema
*Analysis of Meteosat-7 WV imagery and its application to
the study of convective systems and atmospheric stability*
Sep. 2004 - Dez. 2004 Wissenschaftlicher Aufenthalt
am Institut für Physik der Atmosphäre, DLR Oberpfaffenhofen
Development of a cloud mask for MSG - SEVIRI
Jan. 05 - Feb. 05 Digital Signal Processing course
an der Fakultät für Luft- und Raumfahrttechnik
der Universidad Politécnica de Madrid
Jan. 05 - Dez. 05 Doktorarbeit in Physik, Vorlesungen
an der Universidad Complutense de Madrid
März 2006 - Juli 2009 Doktorandin
am Institut für Physik der Atmosphäre, DLR Oberpfaffenhofen
seit Juli 2009 Wissenschaftliche Mitarbeiterin
am Institut für Physik der Atmosphäre, DLR Oberpfaffenhofen

